HIGH ENERGY DENSITY DIRECT METHANOL FUEL CELLS

A Dissertation
Presented to
The Academic Faculty

by

Hyea Kim

In Partial Fulfillment
of the Requirements for the Degree
Doctor of Philosophy in the
School of Chemical & Biomolecular Engineering

Georgia Institute of Technology
December 2010

HIGH ENERGY DENSITY DIRECT METHANOL FUEL CELLS

Approved by:

Dr. Paul A. Kohl, Advisor
School of Chemical & Biomolecular Engineering
Georgia Institute of Technology

Dr. David Sholl
School of Chemical & Biomolecular Engineering
Georgia Institute of Technology

Dr. Carson Meredith
School of Chemical & Biomolecular Engineering
Georgia Institute of Technology

Dr. Meilin Liu
School of Material Science & Engineering
Georgia Institute of Technology

Dr. Tom Fuller
School of Chemical & Biomolecular Engineering
Georgia Institute of Technology

Date Approved: November 1, 2010

In dedication to my loving parents

ACKNOWLEDGEMENTS

I would like to express my greatest appreciation to my advisor Prof. Paul Kohl. His guidance and encouragement has molded me into the researcher that I am. He has always been there for me when I needed him. I would also like to thank my committee members; Prof. Tom Fuller, Prof. David Sholl, Prof. Meilin Liu and Prof. Carson Meredith. They have provided me fruitful input over a broad base of knowledge. I was blessed to have Daphne Perry help me throughout my thesis. She made my stay in our group more than enjoyable as a loving friend.

The Kohl group members will always be remembered with great affection. Especially, Dr. William Mustain and Dr. Shruti Prakash who treated me as a family member, and helped me adapt to school and my new life in America, my officemate Dr. Venmathy Rajarathinam whom I shared even all the small moments in life, Dr. Murat Unlu, Dr. Junfeng Zhou, Irene Anestis-Richard for all their discussions and feedback on fuel cell research, Nathan Fritz and Johanna Stark for all the laughs in the group.

A special thanks to my Korean friends in Atlanta. My roommate of three years, Juhyun Kim, for always standing by my side, Sonia Choy who always took care of me like a real sister, Sangeun Jee my mentor, Jeongwoo Han, Hyewon Lee, Sarah Kim for being great friends, all thriving towards the same goal.

I am grateful for having my Mom and Dad as my parents. They always believed me, supported me, and prayed for me. Without their unconditional love and sacrifices, I would not be where I am today. My younger sister, Siwon, for being there for me and letting me know she always cares. Finally, I would like to thank my fiancé, Jonathan Taejoo Park, for sharing my ups and downs through this time, for loving and understanding me just as I am, and for being a joy in my life.

TABLE OF CONTENTS

LIST OF TABLES

LIST OF FIGURES

LIST OF SYMBOLS

A_1	Membrane area
A_2	Exposed membrane area for fuel transport
A_x	Anode #
α_j	Effective transfer coefficient of the species j
C_x	Cathode #
C_j	Bulk concentration of the species j
δ_1	Membrane thickness
δ_2	MEA thickness
E^o	Standard potential of an electrode
E_a	Activation energy
Eu	Useful power
E_R	IR loss in power
E_X	Cross-over loss in power
F	Faraday's constant

i	Current
k	Pre-exponential term
k_j	Electrochemical rate constant
λ	EOD coefficient
μ	Micro
N_j	Number of moles of species j
n	Number of equivalent per mole
n′	Number of alkoxy groups
Ω	Ohms
P	Permeability coefficient
Δp	Pressure drop across the membrane
R	H_2O/Si mole ratio
R	Ideal gas constant
ρ	Ionic resistivity
S	Selectivity as the ratio of ionic conductivity to methanol permeability
σ	Ionic conductivity
T	Absolute temperature

V_{ocv}	Open circuit voltage
V_{op}	Operating voltage
X	Percentage of ruthenium in the deposit

LIST OF ABBREVIATIONS

ADMFC	Alkaline direct methanol fuel cell
AEM	Anion exchange membrane
CV	Cyclic voltammetry
DMFC	Direct methanol fuel cell
DMF	Dimethyl formamide
EDX	Energy-dispersive X-ray spectroscopy
EOD	Electro-osmotic drag
FTIR	Fourier transform infrared spectroscopy
GPTMS	3-glycidoxypropyltrimethoxy silane
HMC	Hydroxy-methoxy cellulose
IEC	Ion exchange capacity
LSV	Linear sweep voltammetry
MEA	Membrane electrode assembly
MOR	Methanol oxidation reaction
ORR	Oxygen reduction reaction

OCV	Open circuit voltage
SCE	Saturated calomel reference electrode
SHE	Saturated hydrogen electrode
TPB	Three phase boundary
PEM	Proton exchange membrane
PECVD	Plasma enhanced chemical vapor deposition
PTFE	Polytetrafluoroethylene
PSG	Phosphorous-doped silicate glass
SEM	Scanning electron microscope
STA	Silicotungstic acid
TEOS	Tetraethoxy orthosilicate
3MPS	3-mercaptoropyl trimethoxysilane
3TPS	3-(trihydroxysilyl)-1-propanesulfonic acid

SUMMARY

Direct methanol fuel cells (DMFCs) have received attention as a power source for portable devices. Especially for low power electronics, energy density, system efficiency, and life time are the important factors to consider. Improving the methanol conversion efficiency is the most significant challenge for achieving higher efficiency and long life time. The traditional polymer membranes need to be replaced with inorganic ones to reduce the methanol cross-over. Compliant and chemically stable electrodes are necessary for inorganic membranes. Moreover, new DMFC stack design is required for compact systems. The challenges to create a highly efficient DMFC for low power system are addressed in this work.

Inorganic glass membranes have been synthesized via a sol-gel reaction using 3-mercaptopropyl trimethoxysilane (3MPS), 3-glycidoxypropyl trimethoxysilane (GPTMS) and tetraethoxy orthosilcate (TEOS). The effect of oxidation time of the thiol group on the 3MPS, the mole fraction within the sol, and the water ratio in the reactant mixture were investigated. The particular behavior of conductivity and permeability for the glass membranes with respect to polymeric ones was observed. While the conductivity increased, the permeability decreased resulted in high selectivity membrane. The total energy loss of a DMFC was decreased by replacing a Nafion with a glass membrane.

Glass composite electrodes were prepared by incorporating the commercial catalyst nanoparticles (Pt/C or PtRu/C) into a silica-based matrix prepared by sol-gel reaction. A Leaman bath was used to electrolessly deposit Pt in order to both merge the catalyst islands and optimize the electrochemically active area of the electrode layer. For

efficient methanol oxidation on the anode, Pt_xRu_{1-x} bimetallic electrocatalysts have been prepared by modifying the Leaman bath. Formic acid was found to be a more efficient reducing agent than hydrazine to achieve 1:1 ratio of Pt and Ru deposition at lower temperature.

The blocking effect of the glass electrodes on methanol cross-over is of interest. The effect of the gelation time, curing temperature, the mole ratio of the sol components, and the ratio of catalyst to glass on reducing methanol cross-over were investigated using $PtRu/SiO_2$ inorganic electrodes synthesized using 3TPS and GPTMS. The electroless deposition of Pt_xRu_{1-x} improved both methanol permeability and the catalytic activity for methanol oxidation, since the additional metal not only decreased the cross-over but also increased the active catalytic surface area. As a result, the selectivity was increased leading to higher energy efficiency.

Anionic-cationic bi-cell stack design was proposed to achieve higher voltage from the limited volume. A bi-cell design consists of an alkaline exchange membrane (AEM) and proton exchange membrane (PEM) fuel cell in series using a common liquid fuel tank. The actual AEM cathode potential was essentially the same as the PEM anode potential making the bi-cell configuration viable, addressing the short circuit problem between adjacent anodes through the common fuel tank. The bi-cell system was demonstrated with the optimized AEM and PEM fuel cell in series operated from a single fuel tank with higher voltage (theoretically, 2.4 V) and reduced volume.

The current anionic-cationic bi-cell stack performance was limited by the immature alkaline electrode structure. The effect of hydrophobicity in alkaline electrodes was investigated using hydrophobic ionomer and polytetrafluoroethylene (PTFE). The

cathode overpotential was improved by using hydrophobic ionomer even though the ionic conductivity was lower. The addition of PTFE in the catalyst layer does not only decrease the water content but also serves as binder, improving mechanical stability, and introduce porosity, improved mass transport. The ADMFC with optimized electrodes showed improved performance by three times compared to the electrode without PTFE.

CHAPTER 1

INTRODUCTION

1.1 Motivation

Recent advancements in portable electronics have created a need for a higher energy density, lower cost, and longer life energy source. Energy demands for these devices are ever-increasing, since these devices have become multi-functional. The state-of-the-art batteries such as lithium ion batteries have been used for powering these devices. However, the growth of power demands have surpassed the current technology level of batteries which have relatively low energy density, thus limiting the lifetime of portable devices. The complexity of recharging has become another limitation for portability[1].

Direct methanol fuel cells (DMFCs) have several key advantages compared to batteries. High energy density, the most remarkable feature of methanol, can be utilized so that it may lead to small volume, long-life sources. The theoretic energy density of pure methanol is 6100 Whr/kg (realistic energy density is 1200 Whr/kg using 12 M methanol). This compares favorably to lithium ion batteries which are generally in the range of 110-160 Whr/kg [2]. Another significant advantage of DMFCs is the ease of replenishing the fuel. This can be done by replacing the cartridge of methanol, which is easy to store and handle as a liquid. DMFCs are also considered environmentally friendly by only producing small amounts of water and carbon dioxide as by-products. Thus, DMFCs are being considered as an alternative power source for portable electronics.

Portable devices can be divided into different segments, depending on the required power level, which include (with example power levels) laptops (10-120W), cell phones (0.1-10W) and small wireless sensors (1μW-100mW). In the development of traditional high power range DMFCs, including laptops and cell phones applications, increasing power and energy density has been the focal points of improvement to compete with batteries. To achieve high fuel cell performance, it is crucial to develop membranes with high ionic conductivity and low methanol permeability. Electrode surface area has also been a critical parameter in need of optimization, in terms of materials and structures, because it affects the power level and resistive losses. The slow kinetics of methanol oxidation on the anode needs improvement.

However, for low power level applications, such as small wireless sensors, the previously discussed challenges of DMFC development may no longer be the most critical issues. For example, the ionic conductivity can be significantly lower than the one for high power system, since the operating current will be much lower. The design parameters for the fuel cell should shift from the traditional high power mode to low power. Thus, there are different requirements to be satisfied in the development of DMFCs for low power applications.

For smaller devices that only allow a limited space for its power source, volumetric density is a key design parameter. In this sense, DMFCs can be more competitive because they can be built in a simple fashion compared to a large one. Since a low power application can utilize a passive DMFC system, it can be operated without a traditional active fuel delivery system and other balance of plant components, such as the

fuel pump, humidifier and thermal management system. Therefore, DMFCs can be the solution for satisfying various kinds of micro-devices.

1.2 Dissertation Overview

The goal of this dissertation is to create a new class of DMFC targeted at high energy density and low loss for small electronic devices. In order for the DMFC to efficiently use all its fuel, with a minimum of balance of plant, a low-loss proton exchange membrane is required. Moderate conductivity and ultra low methanol permeability are needed. Fuel loss is the dominant loss mechanism for low power systems. By replacing the polymer membrane with an inorganic glass membrane, the methanol permeability can be reduced, leading to low fuel loss. In order to achieve steady state performance, a compliant, chemically stable electrode structure must be investigated. An anode electrode structure to minimize the fuel loss is being studied, so as to further increase the fuel cell efficiency.

Inorganic proton conducting membranes and electrodes have been made through a sol-gel process. The sol-gel process is a cost-effective and rapid wet chemical method. The sol-gel process allows for easy control of both the composition and structure of glasses, in order to achieve the desired conductivity. This process has the potential to increase the ionic conductivity and mechanical properties of the silicate glasses by the correct selection of functionalized silane precursors. A fundamental understanding of the sol-gel process is being studied in order to improve the conductivity and decrease the permeability of the membranes.

To achieve higher voltage and power, multiple fuel cells can be connected in series in a stack. For the limited volume allowed for the small electronic devices, a noble, compact DMFC stack can be designed. Using an ADMFC with a traditional DMFC including PEM, twice higher voltage can be achieved by sharing one methanol fuel tank. Since the current ADMFC technology is not as mature as the traditional DMFCs with PEM, the improvement needs to be accomplished to achieve higher performance from ADMFC. The ultimate goal of this study is to develop a DMFC system with high energy density, high energy efficiency, longer-life and lower-cost for low power systems.

.

CHAPTER 2

BACKGROUND

2.1 Inorganic Proton Exchange Membrane Development

2.1.1 Low Methanol Permeability Inorganic Membrane

In the case of low power fuel cells, the membrane conductivity can be significantly lower than high power cells since the current will be lower. Methanol permeability through the PEM is a critical issue because it results in fuel loss and lowers the effectiveness of oxygen reduction reaction at the cathode. Cross-over through a Nafion membrane is a considerable problem for low-power, long-life fuel cells. Low-power cells can tolerate a modest loss in conductivity, resulting in lower iR drop compared to high-current fuel cells, in order to achieve lower methanol permeability for extended life and higher overall fuel conversion efficiency.

In previous studies, the polymer membrane surface was modified to block methanol transport[3]. Inorganic materials have been introduced into the membrane [4-5], and new inorganic membranes have been developed in order to reduce the methanol permeability through the PEM. In particular, Nogami, Uma, et al. have synthesized new inorganic electrolytes and characterized their behavior. Methanol permeability has been reduced in these previous studies, however, the magnitude of the improvement is not adequate to achieve long-life DMFCs. The membranes have considerable water uptake and free volume resulting methanol permeability. Consequently, there is interest in developing inorganic membranes specifically for low-power DMFC.

Silicate glasses are promising inorganic proton conducting materials due to their intrinsically low methanol permeability, but they have limited ionic conductivity (10^{-6} S cm^{-1}) [6]. As a result, the glass structure needs to be adjusted to enhance their proton conductivity. Prakash et al. [6] fabricated phosphorous-doped silicate glasses (PSG) by plasma enhanced chemical vapor deposition (PECVD) and showed that PSG has potential as a PEM for low power applications. The amount of phosphorous or other oxide in the glass can be tailored to enhance the structure, mechanical strength, and ionic conductivity. PECVD glass made from phosphine and silane yielded PSG with ionic conductivity of 2.52×10^{-4} S cm^{-1}. Though the conductivity was of interest for low power DMFCs, PSG fabricated via PECVD suffers from low mechanical strength, and high equipment cost. It is also challenging to selectively tune the glass structure for proton conduction with PECVD.

An alternative fabrication method for glass membranes has been explored, involving a sol-gel process, which allows control of both the composition and structure of the glass. It is also less expensive and more rapid than vacuum processes. The sol gel process involves two reactions: hydrolysis and condensation using alkoxides as a precursor. In this process, hydrolysis and condensation takes place via 3 steps: i) nucleophilic substitution of the end group, ii) proton transfer from the attacking molecule to an alkoxide (within the transition state), and iii) removal of the end group as alcohol or water [7-8]. The characteristics and properties of the inorganic silica network are related to a number of sol-gel parameters. The parameters that affect the rate of hydrolysis and condensation reactions include: pH, mixing temperature, reaction time, precursor concentration, H_2O/Si mole ratio (R), curing temperature, and reaction time.

Previous attempts to synthesize inorganic glass membranes via the sol-gel process used tetraethoxy orthosilcate (TEOS) [9-11]. Phosphorous was introduced into the silicon dioxide matrix to generate defects during the sol-gel reaction. However the ionic conductivity was limited, because high levels of the secondary oxide, necessary for improved ionic conductivity, caused cracks in the membrane. The glasses needed to be cured slowly for 3 days to 6 months [11-13] to prevent crack formation. Higher temperature also facilitated the full condensation of TEOS glass (e.g. > 400^{o}C) [10-11, 14].

Functionalized alkoxy silanes have been investigated as an additive to the sol-gel glass to improve the properties of the membranes. Tezuka [15] and Siwen [16] have added 3-glycidoxypropyltrimethoxysilane (GPTMS) to the phosphorous doped TEOS mixture to enhance the mechanical strength. The glass membranes containing GPTMS were cured at lower temperature, below 200^{o}C, for a shorter time period (less than 3 days). Park et al., fabricated GPTMS-based membranes by incorporating silicotungstic acid (STA) which served as a proton source [17-18]. The conductivity of the STA-GPTMS membrane was higher than previous membranes, however, the membrane was not chemically stable because the STA did not bond directly to the GPTMS. 3-mercaptopropyl trimethoxysilane (3MPS) was introduced as a second precursor for GPTMS-based membranes [19]. 3MPS was chemically bonded with GPTMS via the sol-gel reaction enhancing the chemical stability of the glass membrane. However, the effect of the sol-gel curing parameters on final properties of the functionalized glass membranes has not been investigated. Also, the methanol permeability coefficient of the functionalized glass membranes has not been reported.

2.1.2 Proton Transport Mechanism

The conductivity and permeability differences between glass and polymer membranes are related to the proton transport mechanism in each material. Bulk transport and surface transport mechanisms have been discussed in the literature [11]. The mechanisms are shown in Figure 2.1. In both cases, the proton is transported through the electrolyte by binding to functionalized stationary anions such as sulfonic acid groups. The transport mechanism is dictated by the chemical properties of the membrane and the chemical environment surrounding the anionic sites within the membrane.

In case of bulk transport, protons are solvated ($H^+(H_2O)_\lambda$) and move with a relatively large solvent shell with λ ranging from 2 to 4. On the other hand, surface transport has less water transport with λ between 0 to 1. The electro-osmotic drag (EOD) coefficient, λ, is one factor in water transport through the membrane, in addition to water diffusion as a result of the concentration gradient [20]. Since polymer membranes, such as Nafion, have a relatively large free volume compared to glass membranes, greater amounts of water can be transported with the proton. Bulk transport is generally the dominant transport mechanism for the polymeric anion exchange membranes.

One ramification of high EOD in Nafion is the sensitivity of its conductivity to relative humidity and residual. Water is needed for conductivity in a polymer membrane, however, excess water can be detrimental to cell performance. Liquid films can form on the electrodes disrupting the delivery of gaseous reactants, especially oxygen to the air-

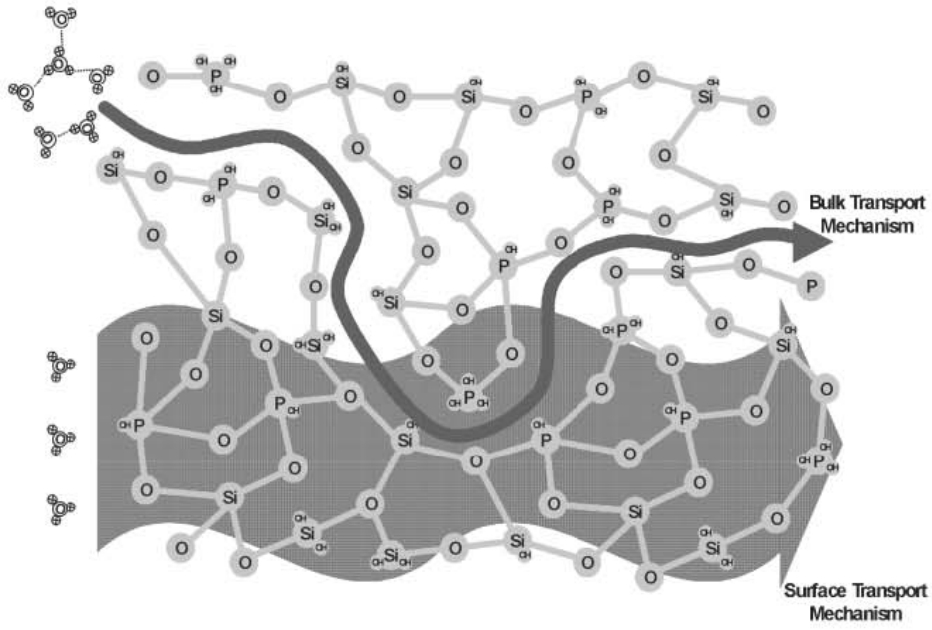

(a)

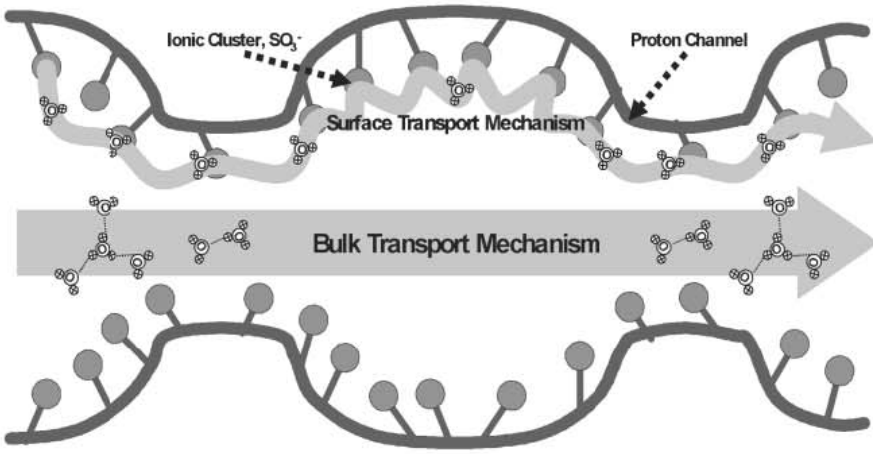

(b)

Figure 2.1: Proton transport mechanisms (a) surface transport in phosphor-silicate glass membrane and (b) bulk transport in the Nafion membrane
(The figure is reproduced with the permission from Journal of Materials Chemistry[11].)

breathing cathode. Methanol permeability is also an issue because materials which facilitate water permeation, generally, have high methanol permeability, such as by

mixed clusters $H^+ (H_2O)_\lambda (CH_3OH)_y$ [11]. Diffusion of methanol through the high free volume within the polymer is also an issue.

The linear relationship between conductivity and permeability for several polymer membranes has been reported in the literature as shown in Figure 2.2 [21]. Therefore, it is desirable to have a material with a lower proton solvation in order to decrease the methanol permeation for a low-power fuel cell. It is critical to make the surface transport dominant over bulk transport in the synthesized electrolytes, since surface transport requires less water. The free volume should be minimized to allow a minimum of adsorbed water leading to surface transport. The density of the functional groups and distance between neighboring sites are important parameters.

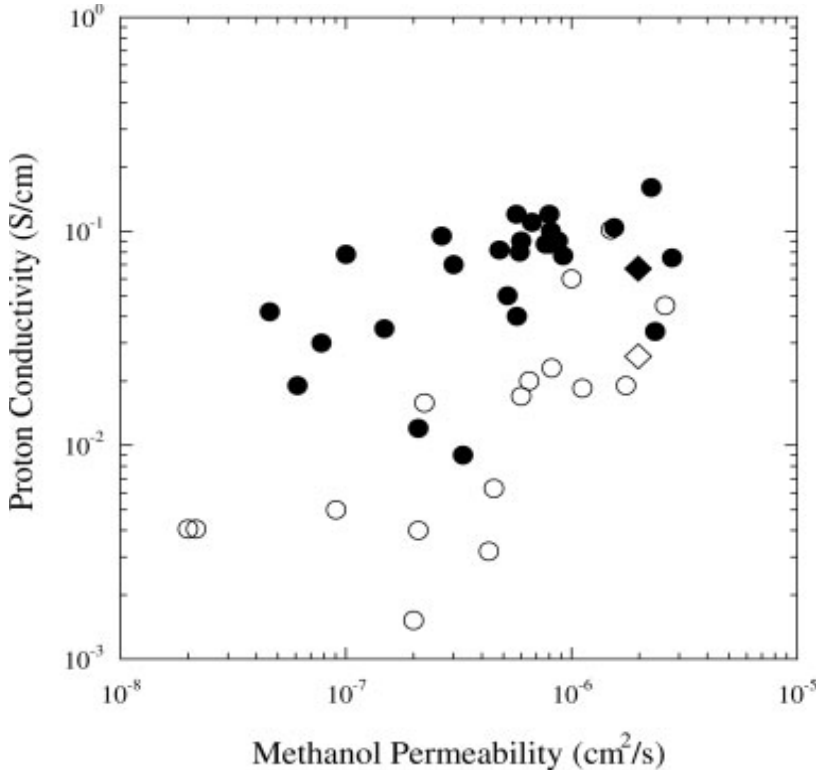

Figure 2.2: Proton conductivity and methanol permeability for existing polymer membranes. ♦ denote the reference values for Nafion.
(The figure is reproduced with the permission from Materials Letters[21].)

2.1.3 High Selectivity Inorganic Membrane

The trade-off between conductivity and permeability can be captured by defining selectivity (S) as the log of the ratio of proton conductivity to methanol permeability, Equation 2.1.

$$S = \log (\text{Conductivity}/\text{Permeability}) \quad (2.1)$$

The advantage of using a glass membrane even with its limited conductivity can be verified by comparing the selectivity value of glasses to Nafion.

For most polymer membranes, the selectivity is low because the high conductivity comes with the burden of high methanol cross-over. For example, the selectivity for Nafion is 4.48 with the conductivity of 10^{-1} S cm^{-1} and the permeability coefficient of 2.62×10^{-6} mol cm $cm^{-2}day^{-1}Pa^{-1}$ [22] by Equation 2.1. Even for the most highly selective membrane in Figure 2.2, the selectivity is 5.48, which is a modest improvement over Nafion. By reducing the free volume of the synthesized glass, the surface transport mechanism could be dominant over the bulk mechanism, and the permeation could be less dependent on conductivity, leading to a high selectivity.

2.1.4 High Energy Efficiency in Low Power DMFC

The energy conversion efficiency of a DMFC with a inorganic glass membrane can be compared to a Nafion membrane, using the energy loss analysis presented previously [23]. There are two main energy losses within the DMFC which must be considered and mitigated in order to achieve high energy efficiency and long operating life with DMFCs. First, ohmic losses in the membrane are caused by resistant to ionic transport through the proton exchange membrane. Second, fuel can be lost by diffusion

through the membrane, often called cross-over. Cross-over not only wastes fuel but also causes a potential drop at the cathode, resulting in low cell performance.

An expression for the energy loss of a fuel cell can be derived by considering the useful energy relative to the each energy loss. The useful power delivered from a fuel cell, E_U, is given in Equation 2.3.

$$E_U = iV_{op} \tag{2.3}$$

where i is the fuel cell current and V_{op} is the operating voltage. IR voltage drop from ionic transport through the proton exchange membrane causes a loss in power, E_R, Equation 2.4.

$$E_R = \frac{i^2 \rho \delta_1}{A_1} \tag{2.4}$$

where ρ is the ionic resistivity of the membrane, δ_1 is the membrane thickness, and A_1 is the area. Then, the energy loss (%) due to IR drop can be calculated by Equation 2.5.

$$\text{IR loss} = \frac{E_R}{E_R + E_U} \times 100 \tag{2.5}$$

For Nafion 117, it has a conductivity of 0.08 S cm^{-1} and 178 μm thickness. The IR loss is 0.01% for a surface area of 1 cm^2, operating at 0.5 V and 200 μA, while the IR loss for a more typical current, 100 mA, is 4.3 %. For low power cells, the current will be at the low end of this range and thus, the conductivity may be substantially reduced as well.

The maximum loss in power, E_x, due to cross-over is given by Equation 2.6.

$$E_X = \left(\frac{P \, \Delta p A_2}{\delta_2} \right) nFV_{op} \tag{2.6}$$

where P is the permeation coefficient of the membrane, Δp is the pressure drop across the membrane, A_2 is the exposed membrane area available for fuel transport through the

membrane, δ_2 is the electrolyte thickness, n is the number of equivalents per mole, F is Faraday's constant. Then, the fuel loss from cross-over (neglecting iR loss) can be calculated by Equation 2.7.

$$\text{Fuel loss} = \frac{E_X}{E_X + E_U} \times 100 \tag{2.7}$$

The fuel loss of Nafion 117 using Nafion permeability of 2.62 x 10^{-6} mol cm $cm^{-2}day^{-1}Pa^{-1}$ [22] is 99.9 %. Despite Nafion's high conductivity, Nafion is not a good electrolyte for low-power sources unless extremely low surface area electrodes were used. Extremely low surface area is a problem because that would require exceptionally high current density and fuel transport problems.

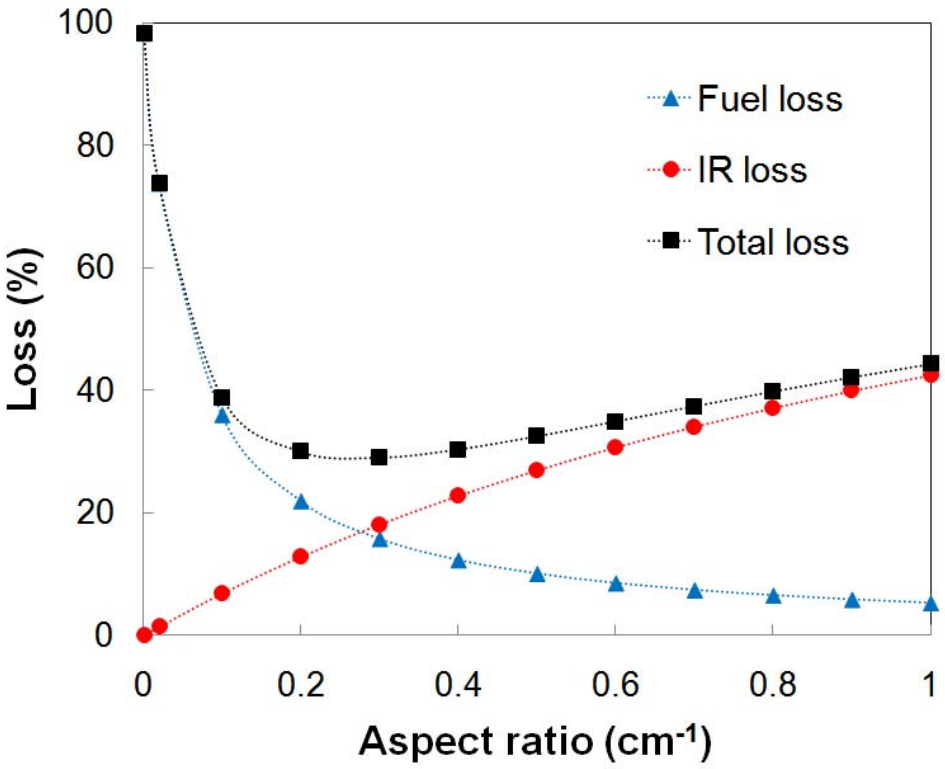

Figure 2.3: The permeation loss and Energy loss as a function of alpha (α=thickness/area)
(*k*= 5x10^{-4} S cm^{-1}, P=10^{-10} molcm $cm^{-2}day^{-1}Pa^{-1}$, i=200uA and V_{op} =0.5V)

The total loss (%) was calculated by Equation 2.8.

$$\text{Total loss} = \frac{E_X + E_R}{E_X + E_R + E_U} \times 100 \quad (2.8)$$

A specific quantity of the membrane, the aspect ratio of the membrane (α=membrane thickness/membrane area), can be defined from Equation 2.4 and 2.6. This design variable α, affects both fuel and IR loss. As shown in Figure 2.3, there is a linear relationship between the aspect ratio and IR loss, and an inverse relationship with fuel loss through cross-over. Therefore, there is a trade-off in the IR and cross-over losses with α. Figure 2.3 expresses the two relationships in the case of a glass membrane with a conductivity of $5x10^{-4}$ S cm^{-1} and the permeability coefficient of 10^{-10} mol cm $cm^{-2}day^{-1}Pa^{-1}$, when the fuel cell operates at 200uA and 0.5V. The total loss which is the sum of the two losses can be lowered to 29.1% from 99.9% by replacing the Nafion membrane with glass even with its lower conductivity.

2.2 Sol-Gel Chemistry

The sol-gel process involves two reactions: hydrolysis and condensation. The general reaction scheme is shown in Figure 2.4. In this process, hydrolysis and condensation takes place via 3 steps: i) nucleophilic substitution of the end group, ii) proton transfer from the attacking molecule to an alkoxide (within the transition state), and iii) removal of the end group as alcohol or water [8, 24].

The characteristics and properties of the inorganic silica network are related to a number of factors that affect the rate of hydrolysis and condensation reactions, such as, sol pH, temperature and reaction time, precursor concentration, H_2O/Si molar ratio (R),

curing temperature and time. Of the factors listed above, pH, H_2O/Si molar ratio (R), and temperature have been identified as the most important parameters as they can significantly affect the rate of reactions.

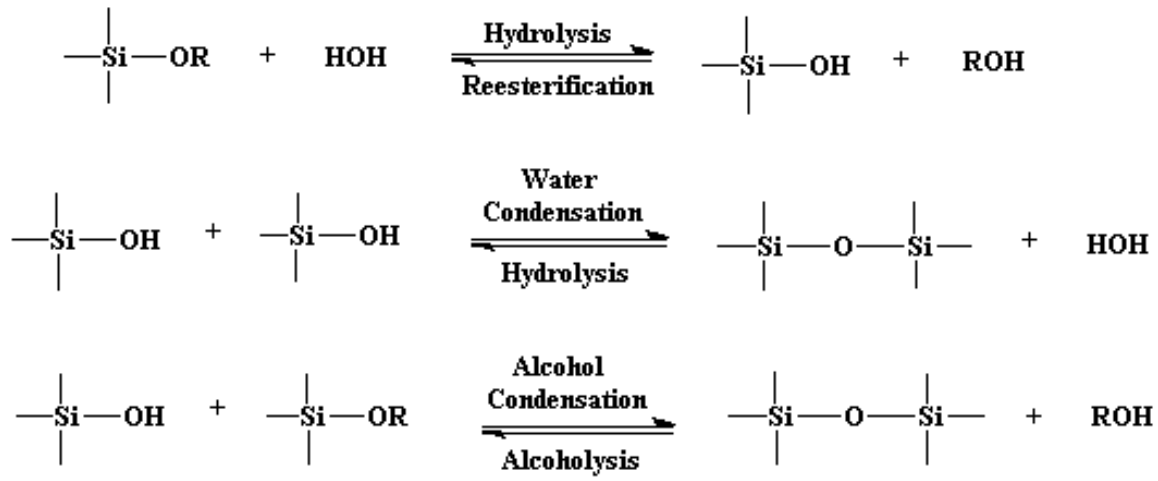

Figure 2.4: The general scheme of hydrolysis and condensation reaction in sol-gel chemistry

It is important that the rate of hydrolysis must be appropriate to allow enough reactants for the condensation to make mechanically rigid and dense functionalized glass with low methanol cross-over. It is possible to control the relative reaction rates for hydrolysis and condensation by adjusting the amount of acid, water and solvent. The theoretical ratio of water for complete hydrolysis and condensation is n′/2, where n′ is the number of alkoxy groups in the reaction precursors. Therefore, the molar ratio of water to silicon, R, is expressed by Equation 2.9 [25].

$$R = \frac{H_2O}{Si(OR)_{n'}} \tag{2.9}$$

It should be noted that R also varies during the sol-gel reaction, since the water is consumed and produced dynamically. Hence, it is important to have the exact amount of

adsorbed water since any excess would eventually lead to an empty space in the glass film and may cause cracks in the matrix after evaporation. It is well known that acids act as a catalyst in sol-gel process. They cause a protonation of the negatively charged alkoxide groups, thus enhancing the reaction kinetics as shown in Figure 2.5. It is believed that acid catalyzed gels contain a higher concentration of adsorbed water, silanol groups and unreacted alkoxy groups. On the other hand, alcohol is used to mix the immiscible silanes and water. The more solvent that is used, the greater the reaction time to complete the condensation reaction. However, the rate of condensation slows with time and leads to a weakly branched network. The collapse of a weak network results in a decrease in mechanical stability.

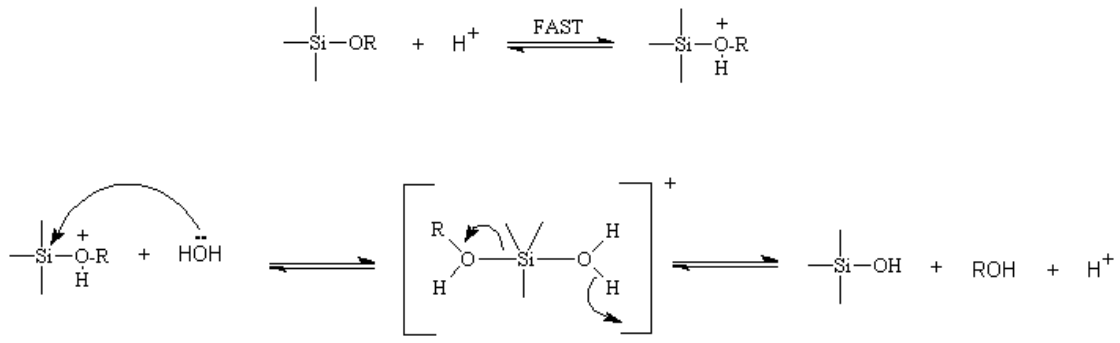

Figure 2.5: Acid-catalyzed hydrolysis

When the condensation reaction is complete, the gel needs to be dried to remove any solvent encapsulated within it. Since the gel structure is not static during curing and continues to undergo hydrolysis and condensation, it is necessary to have a slow rate of solvent and water removal. Cracks in the glass structure can be minimized by monitoring curing time and temperature. Therefore, optimization of the sol-gel parameters can produce a dense, tough silica network to be used as a glass membrane. Conductivity and

permeability will be measured for each sample with different process conditions to find the optimized glass membrane.

2.3 Compliant Inorganic Electrodes Development

2.3.1 Platinum Glass Composite Electrodes

Although the efficiency of the DMFC was improved due to the methanol permeability of the glass vs. polymer membrane [26], the stability of the glass-based direct methanol cell performance was not adequate because a traditional polymer-based catalyst was used with the glass membranes. Using a different ionomer material in the catalyst layer from the membrane itself causes several problems. For example, the contact resistance between the glass membrane and the electrodes is likely to be lowered if the materials are more compatible. The coefficient of thermal expansion of the polymer-based electrodes is significantly different from the glass electrolyte, putting the long term stability into question. Further, using a water-rich polymer ionomer in the catalyst layer is a reliability concern, since the catalyst structure is soaked for long periods in aqueous methanol. The polymer-based ionomer could swell and change the catalyst structure resulting in loss of the three phase boundary, which is a key parameter to achieving high performance. Therefore, it is important to develop glass-based electrodes for use with glass membranes in fabricating polymer-free membrane electrode assemblies (MEA).

In the sol-gel processing of silanes, the catalyst (Pt/C) can be encapsulated in the matrix. It is believed that the size and distribution of the Pt/C particles can be controlled by changing the microstructure and properties of the gel matrix [8]. Water to silane ratio, gelation time, curing time and the ratio of metal to glass are considered as essential

parameters in this process. Figures 2.6 and 2.7 show the effect of the water ratio and the curing time, respectively. Since high water content sols may give larger free volume after evaporation than low water content sols, the metal particles can be dispersed far apart, leading to high sheet resistance. As the gelation time increases, the sol particles grow in solution, resulting in less free volume. Metal particles could be agglomerated during long curing time.

The ratio of metal to glass could significantly affect two properties. More Pt/C particles in the catalyst layer would provide higher electrochemical surface area and higher electric and ionic conductivity.

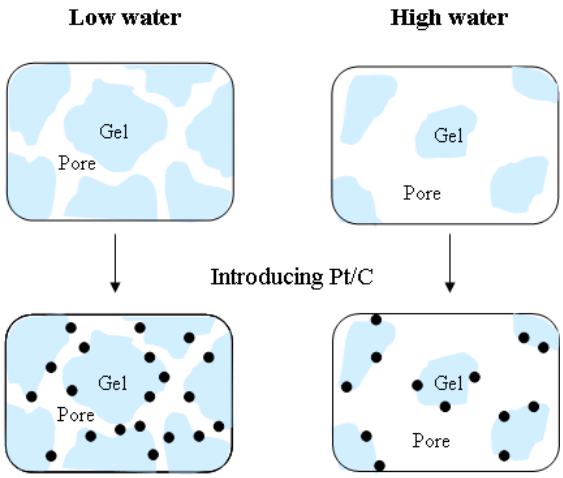

Figure 2.6: The effect of water content

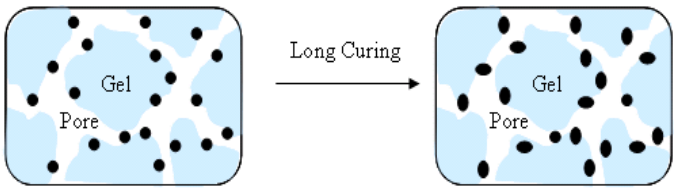

Figure 2.7: Agglomeration due to long curing

The introduction of additional glass material in the electrode could improve the resistance to methanol permeation. It is interesting to consider if electrode-shape and area

engineering could be used to make A_2 smaller than A_1 resulting in lowered cross-over by blocking the membrane area exposed to fuel while maintaining a large value for A_1. When the blocking effect is considered, the total loss can be further reduced.

2.3.2 Pt_xRu_{1-x} Catalyst for Methanol Oxidation

Platinum-only anode electrodes suffer from severe performance degradation due to adsorbed carbon monoxide, which is a strongly bonded reaction intermediate during the methanol oxidation reaction [27]. It has been shown that the methanol oxidation reaction proceeds through the so-called "bifunctional mechanism"[28].

$$CH_3OH + H_2O \rightarrow CO_2 + 6H^+ + 6e^-,\ E^o = 0.02V \quad (2.10)$$

The first active site, M_1, is associated with the methanol adsorption and oxidation. In this mode, it has been found that the adsorbed methanol molecule is oxidized to adsorbed carbon monoxide. This is summarized in Equations 2.11-2.15.

$$CH_3OH + M_1 \rightarrow M_1 - CH_3OH \quad (2.11)$$

$$M_1 - CH_3OH \rightarrow M_1 - CH_2OH + H^+ + e^- \quad (2.12)$$

$$M_1 - CH_2OH \rightarrow M_1 - CHOH + H^+ + e^- \quad (2.13)$$

$$M_1 - CHOH \rightarrow M_1 - COH + H^+ + e^- \quad (2.14)$$

$$M_1 - COH \rightarrow M_1 - CO + H^+ + e^- \quad (2.15)$$

The second active site, M_2, is responsible for adsorbing the water molecule and activating it to yield an adsorbed hydroxyl species (Equations 2.16 and 2.17). The resulting hydroxyl species then provides the second oxygen atom, facilitating the complete reduction of methanol to CO_2, shown in Equation 2.18.

$$H_2O + M_2 \rightarrow M_2 - H_2O \quad (2.16)$$

$$M_2 - H_2O \rightarrow M_2 - OH + H^+ + e^- \quad (2.17)$$

$$M_1 - COH + M_2 - OH \rightarrow M_1 + M_2 + CO_2 + H^+ + e^- \quad (2.18)$$

For methanol oxidation on Pt electrodes, steps 2.11-2.15 proceed quickly, yielding the carbon monoxide intermediate. However, the water activation step, Equation 2.17, occurs slowly at potentials below 0.6 V. This makes Pt electrodes cumbersome for use in direct methanol fuel cells where the oxygen reduction reaction at the cathode already experiences working potential drops greater than 300 mV. Therefore, ruthenium is often alloyed with platinum since it represents a more oxyphilic active site, facilitating the water activation step. This leads to significant improvement in the methanol oxidation behavior of anode electrodes.

2.3.3 Empirical Model for Pt_xRu_{1-x} Electrodeposition

An empirical model for the Pt_xRu_{1-x} deposition process was developed in our previous work [29], taking into account reactant concentration, temperature and surface potential.

The standard reduction potentials for platinum and ruthenium chloride are separated by 0.33 V with platinum the more noble metal, Equations 2.19 and 2.20, respectively [30].

$$PtCl_6^{-2} + 4e^- \rightarrow Pt(s) + 6Cl^-, \; E^o = 0.73V \quad (2.19)$$

$$RuCl_5^{-2} + 3e^- \rightarrow Ru(s) + 5Cl^-, \; E^o = 0.4V \quad (2.20)$$

Thus, the deposition of platinum is favored at potentials near their standard potentials. At potentials sufficiently negative of their standard potentials, mass transfer is expected to limit the deposition rate of each metal. In this development, the relationship between

current and overpotential (E-E^o) is given by the Butler-Volmer kinetic expression, Equation 2.21.

$$N_j = \frac{i_j}{n_j F} = Ak_j C_j \exp\left[\frac{F\alpha_j}{RT}\left(E - E_j^o\right)\right] \tag{2.21}$$

where N_j is the number of moles of either Pt or Ru deposited, i_j is the current associated with the deposition of either Pt or Ru, n is the number of equivalents per mole, F is Faraday's constant, A is the electrode area, k_j is the electrochemical rate constant, C_j is the bulk concentration of the species j, α_j is the effective transfer coefficient for each reduction process, R is the ideal gas constant, and T is the absolute temperature. It is recognized that the standard potential for alloy deposition for each metal may differ from the pure metal's standard potential.

The percentage of ruthenium in the deposit, X, can be expressed in terms of the reduction current going to each ion, $PtCl_6^{-2}$ and $RuCl_5^{-2}$, Equation 2.22.

$$X = 100\left(\frac{N_{Ru}}{N_{Pt} + N_{Ru}}\right) = 100\left(\frac{1}{\frac{N_{Pt}}{N_{Ru}} + 1}\right) \tag{2.22}$$

The relative reaction rate for the two species, i_{Pt}/i_{Ru} can be found by first applying Equation 2.21 to both species and dividing them, yielding Equation 2.21.

$$\frac{N_{Pt}}{N_{Ru}} = \frac{Ak_{Pt}C_{Pt}\exp\left[\frac{F\alpha_{Pt}}{RT}\left(E - E_{Pt}^o\right)\right]}{Ak_{Ru}C_{Ru}\exp\left[\frac{F\alpha_{Pt}}{RT}\left(E - E_{Ru}^o\right)\right]} \tag{2.23}$$

These exponential terms can be merged and expanded.

$$\frac{N_{Pt}}{N_{Ru}} = \frac{k_{Pt}C_{Pt}}{k_{Ru}C_{Ru}}\exp\left[\frac{FE}{RT}\left(\alpha_{Pt} - \alpha_{Ru}\right) + \frac{F}{RT}\left(\alpha_{Pt}E_{Pt}^o - \alpha_{Ru}E_{Ru}^o\right)\right] \tag{2.24}$$

The constant terms in Equation 2.24 can be combined to give two parameters, a and b.

$$\frac{Ni_{Pt}}{N_{Ru}} = a\left(\frac{C_{Pt}}{C_{Ru}}\right)\exp\left[\frac{b}{T}E\right] \tag{2.25}$$

where

$$a = \frac{k_{Pt}}{k_{Ru}}\exp\left[\frac{F}{RT}\left(\alpha_{Pt}E^{o}_{Pt} - \alpha_{Ru}E^{o}_{Ru}\right)\right] \tag{2.26}$$

and

$$b = \frac{F}{R}\left(\alpha_{Pt} - \alpha_{Ru}\right) \tag{2.27}$$

where b is a temperature independent constant and the inverse of the Tafel slope. Rearranging Equation 2.25 yields a simple expression for the relative deposition rates of Pt and Ru.

$$\ln\left(\frac{N_{Pt}}{N_{Ru}}\right) = \ln\left(a\left[\frac{C_{Pt}}{C_{Ru}}\right]\right) + \frac{b}{T}E \tag{2.28}$$

The parameter 'a' has complicated temperature dependence. This approach requires that the heterogenous rate constant and transfer coefficient for each metal on the alloy surface remain essentially constant with alloy composition. The rate constant data is contained in parameter 'a' as well as the thermodynamic effect, E_j^o's, for the metals. Accurate determination of 'a' is needed in order to reliably describe the deposition process.

2.4 DMFC Stack Design

In order to achieve higher voltage than values obtained from a single fuel cell, and high power-density, multiple fuel cells can be connected in series in a stack. Three different types of stack design for PEMFC have been discussed[31-35]. The bipolar

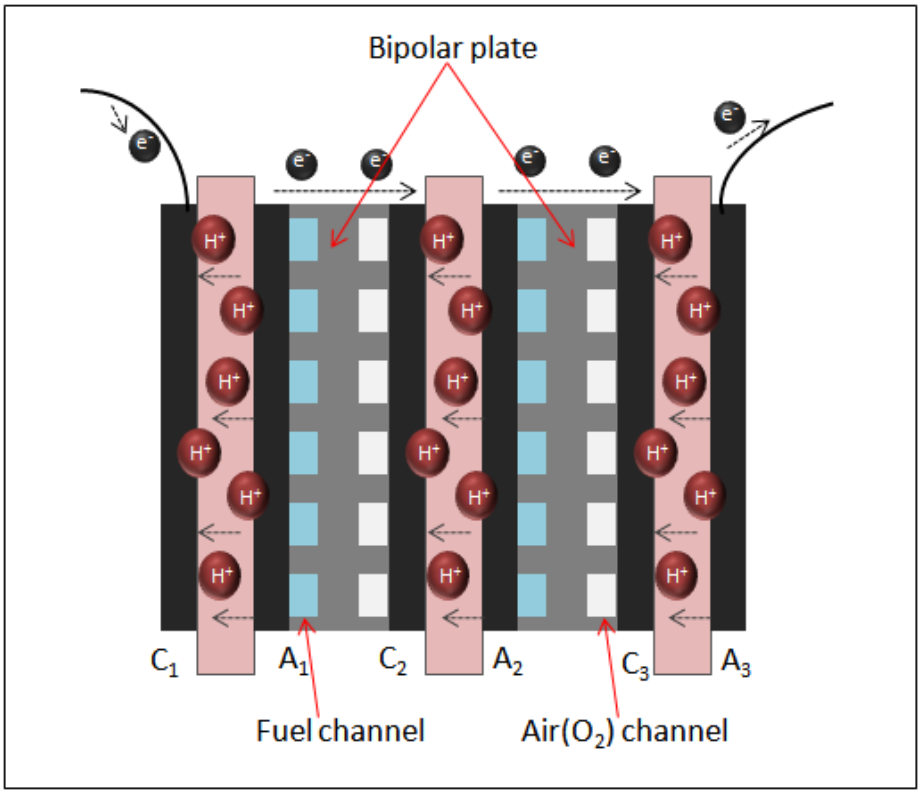

Figure 2.8: A schematic of bipolar stack design

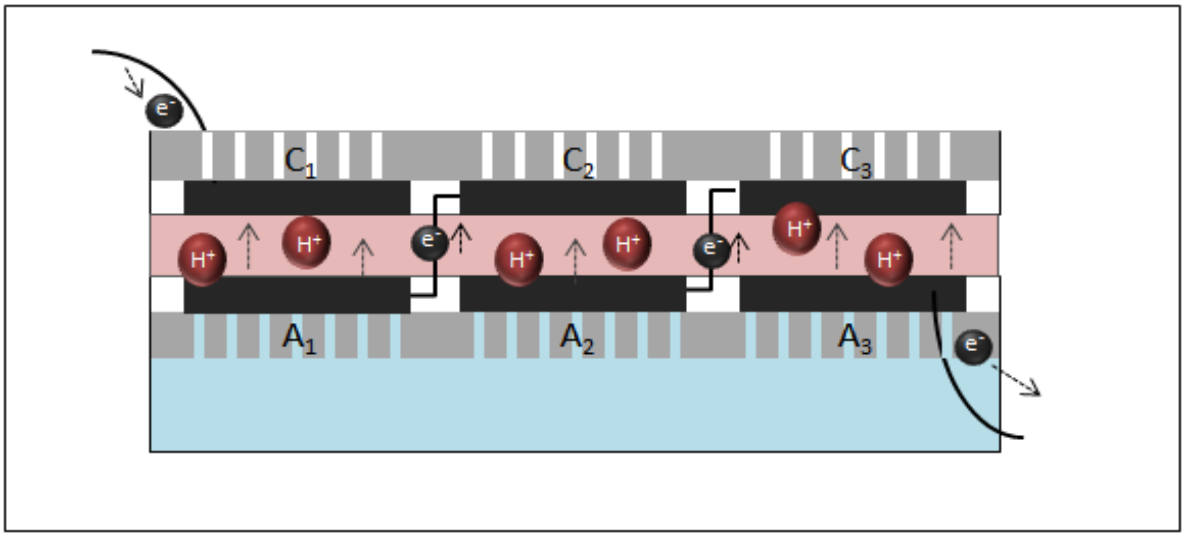

Figure 2.9: A schematic of monopolar stack design

stack in Figure 2.8 connects the anodes and cathodes in series through a metallic bipolar plate, which also serves as a fuel distribution channel. The second design is a monopolar stack where multiple anodes are serviced by the same fuel supply as shown in Figure 2.9. The series connection is accomplished by electronically connected to the cathode of the next cell in a series configuration. Although it has attractive features, such as light weight and low cost, it was hard to achieve high power due to the high internal resistance [36-37]. Moreover, in case of DMFC application, there is a concern about possible electrolysis of the water in the fuel, because more than 1.2V could be produced with several electrodes sharing the same fuel tank.

Chu et al. [33] published a bi-cell stack design (or pseudo bipolar), as described in Figure 2.10. Each unit consists of two PEM single cells. The two anodes (A_1 and A_2) operate with a common fuel source or channel, and the cathode (C_2) faces the cathode (C_3) in the next bi-cell unit. The anode (A_x) is electronically connected to the next cell's cathode (C_{x+1}) to form a series connection. It is easy to assemble the stack and the overall volume is smaller than the normal bi-polar stack due to the common fuel tank. Also, the bi-cell design reduces the need for expensive bipolar plates.

However, there is a potential difference between anode A_1 and cathode C_2. When these two electrodes are shorted together in the series configuration, the liquid methanol fuel provides an ionic path for anode A_1 to act as the anode to cathode C_2. Since A_1 and C_2 are electrically shorted, no electrical current flows in the external circuit as a result of this electrochemical reaction. Under acidic conditions, the standard potential for the two electrochemical reactions is given in Equations 2.29 and 2.30, respectively, and the overall reaction is given by Equation 2.31.

Anode: $CH_3OH + H_2O \rightarrow 6H^+ + 6e^- + CO_2$ ($E°_a$=-0.02 V vs. NHE at 25°C) (2.29)

Cathode: $3/2\ O_2 + 6e^- + 6H^+ \rightarrow 3H_2O$ ($E°_c$= 1.23V vs. NHE at 25°C) (2.30)

Overall: $CH_3OH + 3/2\ O_2 \rightarrow 2H_2O + CO_2$ (E_{cell} = 1.21V vs. NHE at 25°C) (2.31)

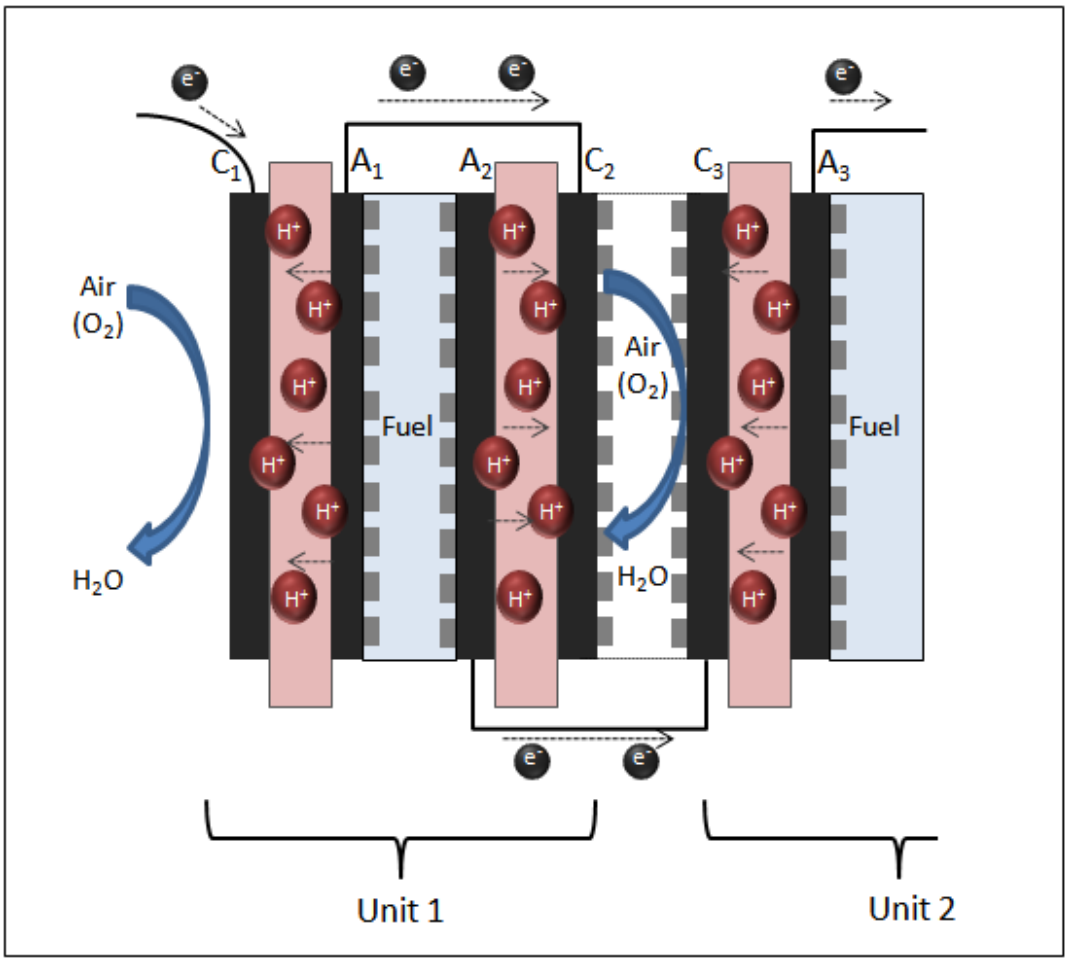

Figure 2.10: A schematic of bi-cell stack design using PEM-PEM in series for H_2/Air fuel cell (A: anode, C: cathode)

Thus, the origin of this electrochemical short circuit between anode A_1 and cathode C_2 is the field developed between the electrodes and ionic path through the liquid methanol. This results in a self-discharge mechanism and loss of fuel efficiency. This same short circuit can also occur in the monopolar stack, since the anode in one cell is

shorted to the cathode in the next cell and the two are ionically connected through the common methanol fuel tank. The magnitude of the undesired proton transport through the fuel tank could be lessened by spacing the cells farther apart or forming an insulating barrier between adjacent cells, however, this is at the expense of compact designs.

2.5 The Challenge in AEM Electrode Development

Alkaline direct methanol fuel cells (ADMFC), made of anion exchange membranes, have the potential to address many of the problems faced by acidic counter parts made with proton exchange membranes. The high pH environment in ADMFCs provides faster kinetics for both electrode reactions, methanol oxidation reaction (MOR) and oxygen reduction reaction (ORR). ADMFCs can pave the way for use of non-noble catalysts, such as silver and nickel [38-41] . The fuel crossover is expected to be lower due to the migration of hydroxide ions from cathode to anode, the opposite direction of fuel crossover [42-43]. Yet, the beneficial effects of alkaline media are not reflected compared to acid media in terms of fuel cell performance.

One of the major reasons for the limited performance might be due to the immature electrode structure for AEM electrodes [44-45]. The major issue in developing an efficient electrode is to achieve high effective catalyst surface area, which is a function of three phase boundary (TPB) between catalyst, ionomer and reactants. The ionomer plays a dominant role in obtaining high TPB and provides mechanical stability. Therefore, the properties and content of ionomer in the electrode should be delicately controlled when developing a high performance fuel cell.

In the earlier development of ADMFCs, PTFE and Nafion were used as a binder and additional alkaline electrolyte was added to the fuel since a soluble form of an anion conducting ionomer was not available.[39, 43, 46] The electrodes using PTFE and Nafion provided good adhesion, however the fuel cell performance was poor because PTFE and Naion could not conduct the hydroxide ions. Recently, an anion conducting ionomer, A3, was developed by Tokuyama. Yamazaki et al. [44] evaluated A3 for alkaline direct methanol fuel cells (DMFCs) and found that A3 could reduce the electrode polarization. However, they concluded that the ionic conductivity of A3 should be further improved to increase the fuel cell performance so a supporting metal hydroxide solution would not need to be added to the fuel. Also, Liang et al. [47] found that the film-like, compact structure of the A3 in the catalyst layer decreased the effective surface area and blocked mass transport.

In our previous study [45], the solubilized ionomer of poly (arylene ether sulfone) containing trifluoromethyl groups, functionalized with quaternary ammonium groups, was studied for ADMFC in static mode. The electrode overpotentials were investigated using a half-cell test to find the optimum content and properties of the ionomer. Although the fuel cell performance was improved by the optimization, the benefits of the alkaline environment were still not reflected. The overpotential of the electrodes was high possibly due to the high water uptake of the ionomer. The swelling of ionomer during operation resulted in blocking reactants to the TPB and also decreasing mechanical stability.

CHAPTER 3

SOL-GEL BASED SULFONIC ACID-FUNCTIONALIZED SILICA PROTON CONDUCTIVE MEMBRANE

3.1 Objective

Minimizing the fuel loss due to methanol cross-over is the most important issue for creating long-life, low-power DMFC sources. The inorganic glass membrane is of interest due to its low methanol permeability compared to polymer membranes. Sulfonic acid-functionalized glass membranes have been synthesized via sol-gel reactions for low power DMFCs. Three different alkoxy silanes reactants were investigated in the sol-gel reaction: 3-glycidoxypropyltrimethoxysilane (GPTMS), 3-mercaptopropyl trimethoxysilane (3MPS), and tetraethoxy orthosilicate (TEOS). The effect of oxidation time of the thiol group on the 3MPS, the mole fraction within the sol, and the water ratio in the reactant mixture were investigated. The ionic conductivity and methanol permeability has been characterized and optimized. The goal was to find a balance between the ionic conductivity and methanol permeability, which determines the fuel conversion efficiency and device lifetime. The work presented in this chapter has been previously published in the Journal of Power Sources [26].

3.2 Experimental

The inorganic glass membranes were prepared using three alkoxy silanes: TEOS, 3MPS, and GPTMS. GPTMS and 3MPS were obtained from Gelest Corporation, and TEOS was obtained from Tokyo Kasei. Mixtures containing 90 mol% of 3MPS, x mol% of GPTMS, and (10-x) mol% of TEOS were prepared and dissolved in methanol and water. HCl was added drop-wise to the mixture and the solution was stirred for 4 hrs to allow hydrolysis and polycondensation to occur in forming the gel. To make free-standing membranes, the gel was infiltrated into a fiber glass matrix (Fisher Scientific), which was 600 um thick and 2.5 um average pore size. The composite membrane was pressed with two Teflon plates and air-dried at room temperature for 12 hrs. The glass membrane was then cured by heating to 60°C, 100°C, 150°C, and 225°C for three hrs at each temperature. The highest three temperatures were done under vacuum. The samples were allowed to cool via convection for 12 hrs followed by conversion of the thiol to the sulfonic acid. The thiol groups in the glass membrane were oxidized with 10% hydrogen peroxide for 3 hrs at 60^{o}C.

The voltammetry and impedance spectroscopy experiments were performed with a Perkins Elmer PARSTAT 2263 potentiostat. The membrane was placed between the two glass cells and a 1.0 M H_2SO_4 electrolyte solution was filled and impedance was measured at room temperature. The two platinum electrodes were placed on either side of the membrane at a fixed distance from either face of the membrane and connected to a potentiostat. The frequency of the impedance measurements ranged from 100 mHz to 1 MHz with an AC signal amplitude of 10 mV. At least one hour equilibrium time was allowed to take the data point and the final value was confirmed by undertaking multiple

runs ensuring equilibrium. The conductivity measurements were reproducible with about 0.2% error, which was insignificant. The methanol permeability of the membrane was determined by sealing the membrane to the end of a methanol filled tube. The loss of methanol was determined gravimetrically. The permeability coefficient value was obtained within 1.8% error. The water uptake of the synthesized membrane was evaluated by comparing the weight of dry and wet membrane. The weight of dry membrane was measured after nitrogen dried for 24 hours at 100°C. The weight of wet membrane was measured after soaked in water for 24 hours at room temperature. The thermal stability of the synthesized membrane was measured through thermogravimetric analysis (TGA) using TA Instruments Q50 with a N_2 flowrate of 40 mL min^{-1}, and a heating ramp rate of 5°C min^{-1} from 25°C to 500°C. Fourier transform infrared spectroscopy (FTIR) data were collected between 400 and 4000 cm^{-1} using a Perkin-Elmer 1600. Pt/C-SiO_2 composite glass electrodes were fabricated on the membranes to test the performance of the glass membranes synthesized here [48].

3.3 Results

The first issue faced in the creation of a proton conducting silica membrane was the formation of a stable glass matrix. SiO_2 glass membranes were prepared via the sol-gel reaction with a 1:3:7 mole ratio of TEOS: water: methanol. A three-fold excess of water with respect to silane was used to ensure complete hydrolysis and condensation of the TEOS. A seven-fold excess of methanol was used so that the mixture was miscible. One mole percent of hydrochloric acid per mole silane was added to catalyze the sol-gel reactions. P_2O_5 was added to the mixture in order to increase the ionic conductivity of the

glass membrane by forming a phosphor-silicate glass matrix. The silicon-to-phosphorous atomic ratio was 19:1.

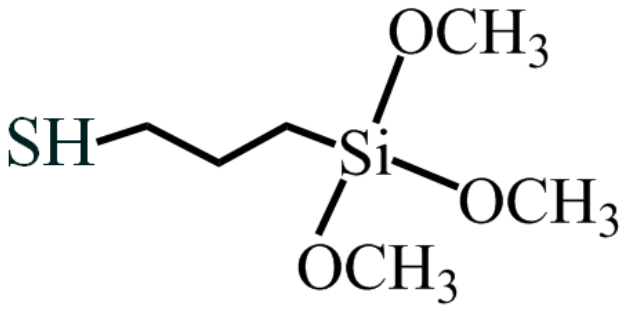

(a)

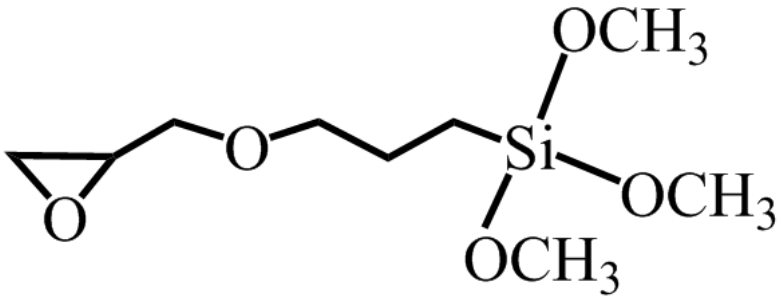

(b)

Figure 3.1: Molecular structure of (a) 3MPS, and (b) GPTMS

The conductivity of the phosphorous doped glass increased with increasing phosphorous content, however, the mechanical stability of the glass was reduced resulting in films with cracks, pores, and brittleness at the highest phosphorous loadings. Increasing the curing time helped to mitigate crack formation. The sol-gel reaction was allowed to proceed for 4 hrs at ambient temperature, followed by curing at 75, 150, and 250°C for 3 hrs each. The glass membrane was fragile even when the phosphorous content (with respect to the silicon content) was as low as 5 wt%. The resulting

conductivity of the 5 wt% phosphorous membrane was 10^{-5} S cm^{-1}, which is an order of magnitude lower than the PECVD fabricated phosphor-silicate glass membrane [6].

The incorporation of sulfonic acid groups attached to the glass matrix is a possible means to increase the conductivity and stability of the glass membrane while keeping a moderately fast curing process. Glass membranes with embedded sulfonic acid groups, controlled porosity, and mechanical toughness were synthesized by including two functionalized alkoxysilanes in the sol: 3MPS and GPTMS, as shown in Figure 3.1. 3MPS has been previously investigated as a proton conducting moiety [4, 19, 49-51]. The thiol group within the 3MPS was converted to a sulfonic acid group before or after membrane fabrication by mild oxidation with hydrogen peroxide [4, 52]. GPTMS has epoxide and trimethoxy silane functionalities so that it can provide cross-linking and flexibility to the silica structure.

The conditions for conversion of the 3MPS thiol to a sulfonic acid were first investigated. Two micrometer thick glass membranes containing 3MPS were prepared by the sol-gel reaction using a starting mixture with a mole ratio of 1:3:5 (3MPS: water: methanol). One drop of HCl was added to 6 ml of solution to catalyze the sol-gel reaction. The mixture was stirred for 1 hour at ambient temperature. The film was deposited on a metalized wafer and cured at 180°C for 12 hrs. The thiol moiety in glass film was oxidized to sulfonic acid by soaking the film in 10% hydrogen peroxide at 60°C for 2 hrs. The conversion from thiol to sulfonic acid was confirmed by FTIR analysis. Figure 3.2 shows the FTIR spectrum of the cured and oxidized film. The thiol peak at 2570 cm^{-1} is seen before oxidation. The thiol peak was smaller after an hour of oxidation, and full conversion occurred within 2 hrs of oxidation in peroxide. However, when the

thiol groups were converted to sulfonic acid by adding the hydrogen peroxide during the sol-gel reaction (before membrane fabrication), the sol was not fully condensed to form the glass structure because the negatively charged sulfonic acid groups present during the reaction prevented silanes from undergoing condensation. The pretreated membrane lost their mechanical structure and easily dissolved in methanol. The oxidation conditions for conversion of the thiol to sulfonic acid may be different for thicker films, such as a 600 um thick glass membrane. A thick membrane (632 um) was oxidized with 10%

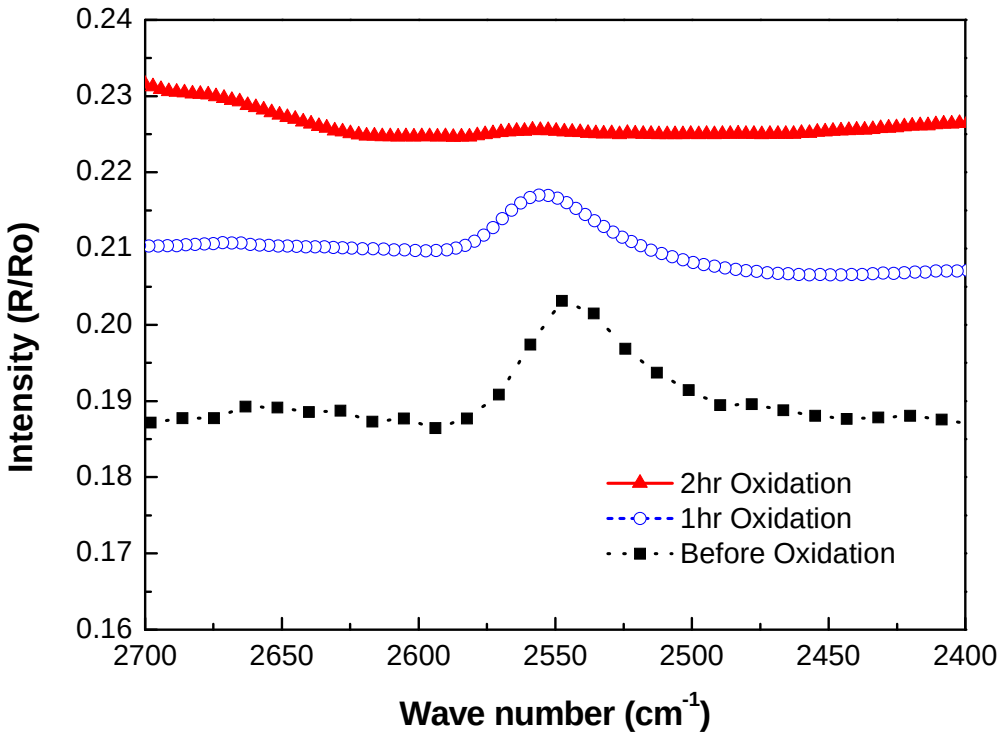

Figure 3.2: Fourier Transform Infrared Spectra of the thiol peaks assigned at 2570 cm^{-1} before the oxidation step, after an hour and two hours of oxidation

hydrogen peroxide at 60°C for varying times and examined by FTIR. The conductivity and permeability of the synthesized glass membranes were measured as a function of

oxidation time. Figure 3.3 shows that the ionic conductivity increased with the oxidation time up to three hours. The initial ionic conductivity of the glass membrane was 2.24 x 10^{-4} S cm^{-1}, and it increased to 5.26 x 10^{-4} S cm^{-1} after 1 hr of oxidation, and further increased to 1.7 x 10^{-3} S cm^{-1} after 3 hrs of oxidation. The slope of ionic conductivity is related to the conversion rate of thiol groups to the sulfonic acid groups.

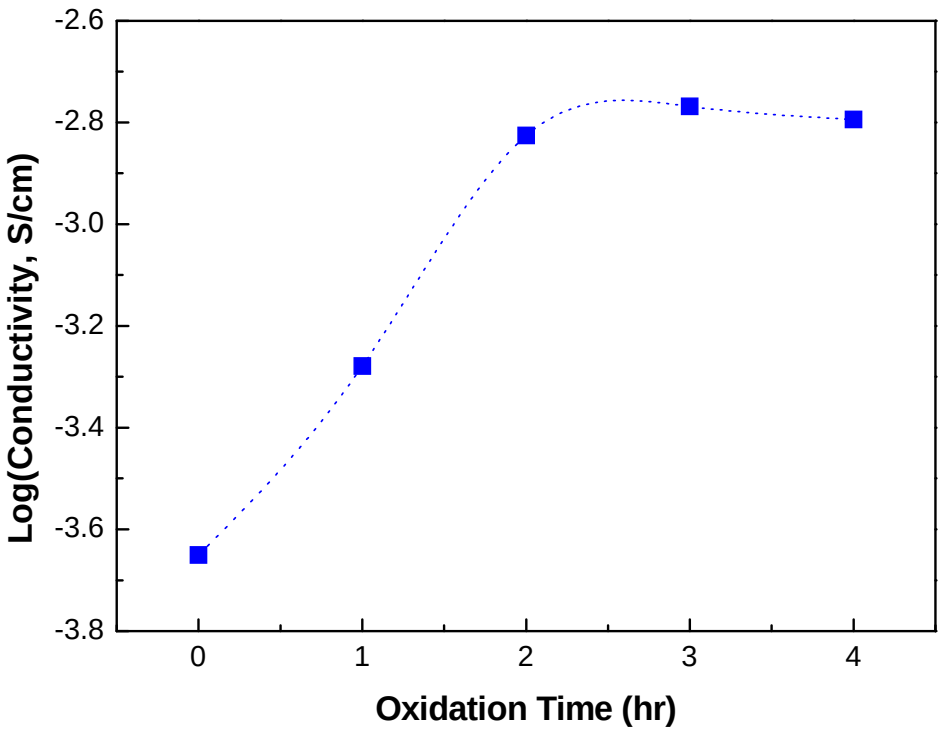

Figure 3.3: Ionic conductivity as a function of oxidation time at 60°C by 10% hydrogen peroxide

An increase in conductivity is a benefit, if the methanol permeability does not increase at as fast a rate. Figure 3.4 shows the methanol permeability for the same samples as reported in Figure 3.3. The permeability decreased with oxidation time until it reached a steady-state value after 3 hrs oxidation time. The initial permeability

coefficient was 6.52 x 10^{-9} mol cm $cm^{-2}day^{-1}Pa^{-1}$ and after 3 hrs oxidation it decreased to 3.19 x 10^{-9} mol cm $cm^{-2}day^{-1}Pa^{-1}$. The chemical stability in methanol was tested by soaking the synthesized membranes in a 10 M methanol solution followed by measuring the change in conductivity. Figure 3.5 shows that the conductivity of the 3 hr oxidized glass membrane was stable for more than 30 days, after which the test was terminated.

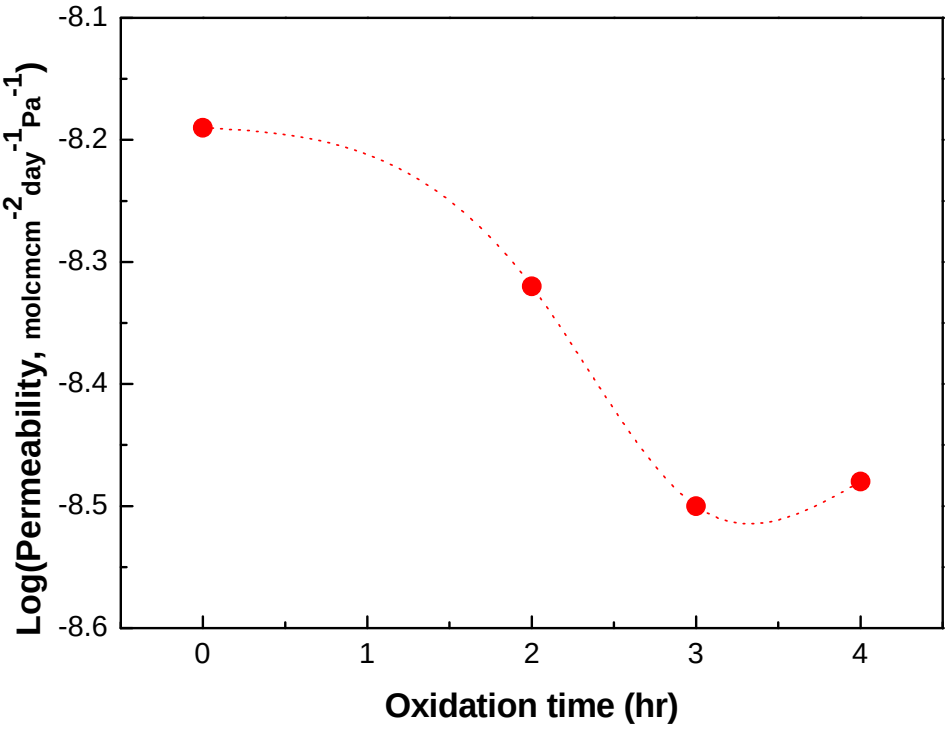

Figure 3.4: Methanol permeability as a function of oxidation time at 60°C by 10% hydrogen peroxide

The physical properties, particularly the fracture toughness and robustness, have been found to be a strong function of the sol mixture. 3MPS-GPTMS membranes have been synthesized with varying amounts of 3MPS ranging from 10% to 90%. It was found that the mole ratio of 3MPS had to be kept above 90% to maintain mechanically

stable, crack-free membranes. When samples were prepared with less than 90% 3MPS, the glass membranes fractured during curing.

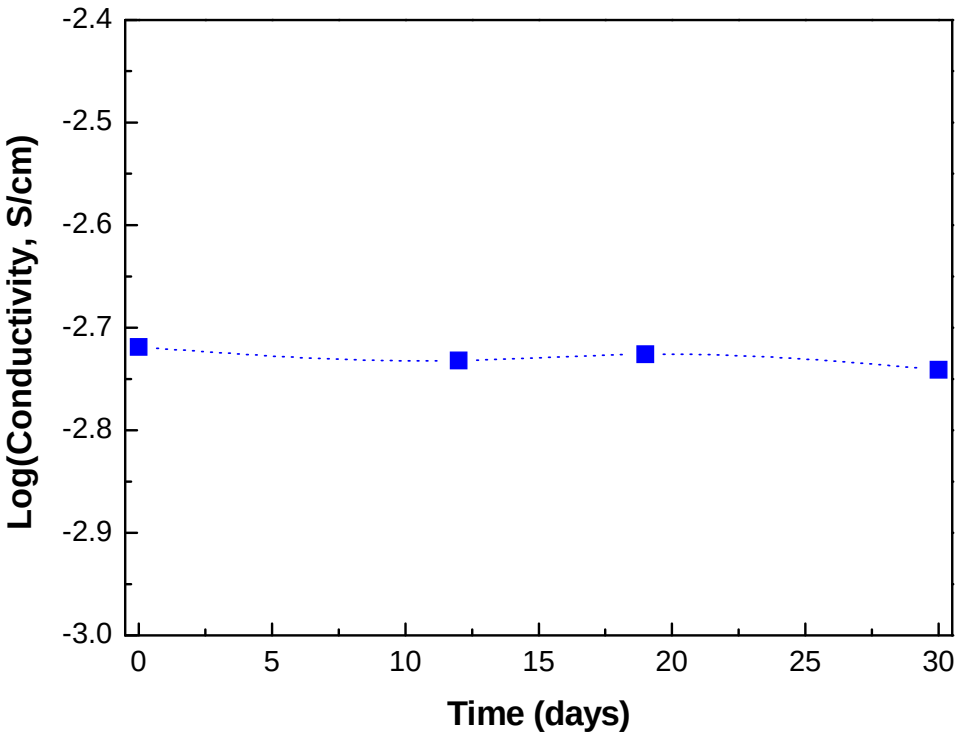

Figure 3.5: Stability in ionic conductivity of a three hour oxidized membrane soaked in 10M methanol over 30 days

TEOS was added to the 3MPS-GPTMS glass membrane in order to densify the matrix and promote a high degree of cross-linking. It was found that in the absence of TEOS, the glass membrane cracked easily when only GPTMS and 3MPS were used. GPTMS and 3MPS are larger molecules than TEOS which would result in fewer cross-links per unit volume. In addition, it would be harder to achieve complete reaction because of the distance between functional groups [53]. The addition of TEOS increased

the cross-link density resulting in membranes without cracks. In addition, TEOS reduced the degree of phase separation [49].

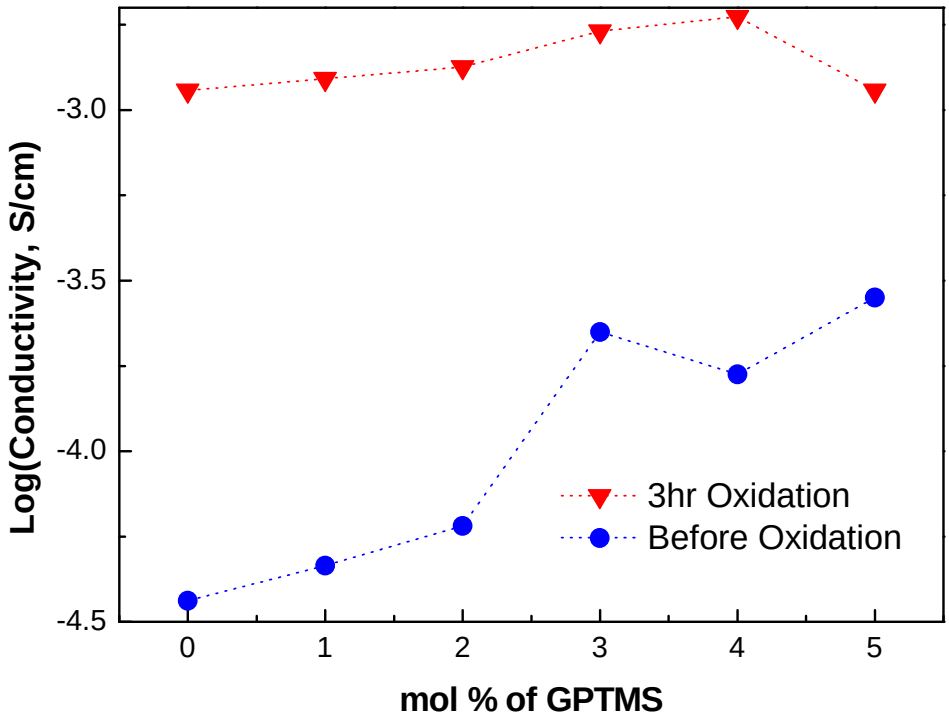

Figure 3.6: Ionic conductivity as a function of a molar ratio of GPTMS before oxidation and after three hours of oxidation

In the optimized membranes, the mole ratio of TEOS and GPMTS was varied but the sum remained 10 mole%. The conductivity and permeability of the synthesized membranes were measured and are shown in Figures 3.6 and 3.7. The conductivity of the membranes before oxidation increased with GPTMS mole ratio, as shown in Figure 3.6. GPTMS by itself provides limited proton conduction through the ethylene oxide moiety. Cations can migrate between the oxygen sites of ethylene oxide [18, 54-55]. Thus, the conductivity of GPTMS-TEOS membrane was greater than 10^{-7} S cm^{-1}. After three hours

oxidation in hydrogen peroxide, the conductivity of each sample increased to more than 10^{-3} S cm^{-1}. The highest conductivity, 1.9 mS cm^{-1}, was obtained with 4% GPTMS.

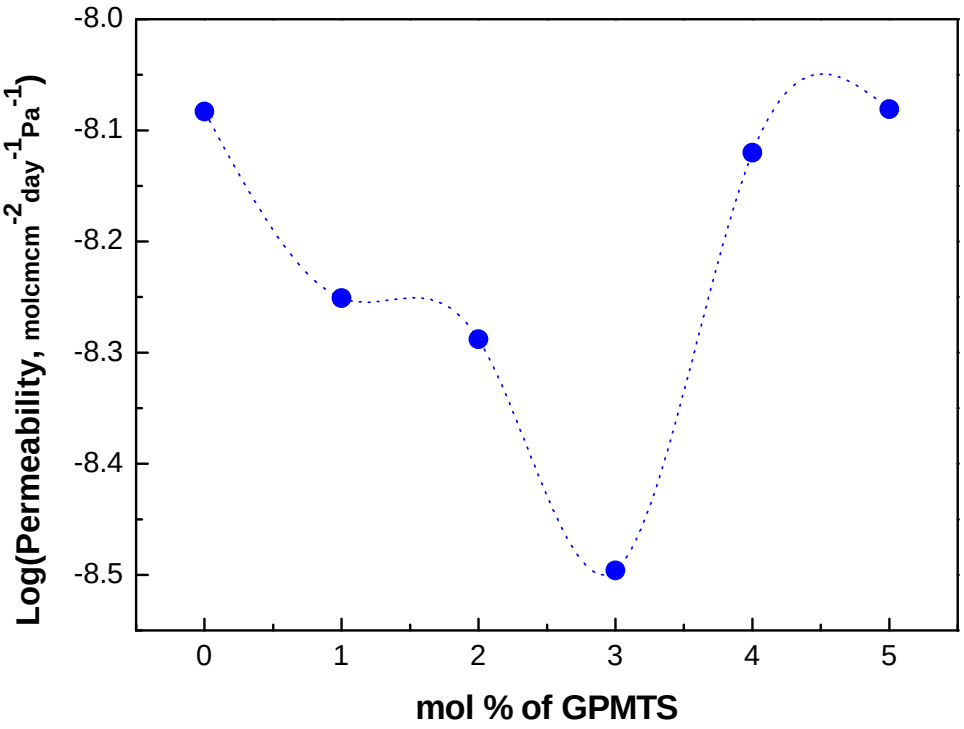

Figure 3.7: Methanol permeability as a function of the molar ratio of GPTMS

The methanol permeability was evaluated for each of the membranes in Figure 3.6, as shown in Figure 3.7. The permeability improved with addition of GPTMS and was lowest at 3 mol%. For a sample with no GPMTS, the permeability of the membrane was measured to be 8.25 x 10^{-9} mol cm cm^{-2} day^{-1} Pa^{-1}. The permeability decreased to 3.19 x 10^{-9} mol cm cm^{-2} day^{-1} Pa^{-1} for a sample with 3 mol% GPTMS and then increased again because excess epoxy groups might tighten the glass structure resulting in cracks. Even though the conductivity of the 4 mol% GPTMS membrane was higher than the 3 mol% membrane, the selectivity (conductivity/permeability) of the 3 mol% membrane

was highest due to the lower methanol permeability. The optimization membrane was fabricated from a 90-7-3 mol% of 3MPS-TEOS-GPTMS mixture.

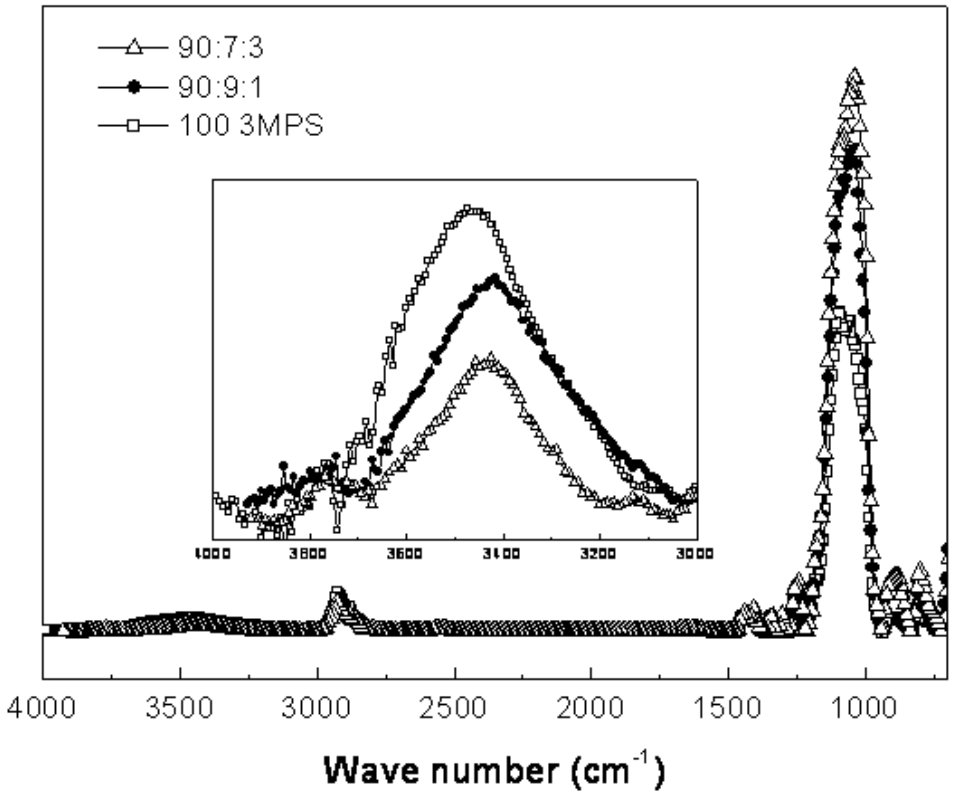

Figure 3.8: Fourier Transform Infrared Spectra of different composition of 3MPS to TEOS to GPTMS. (90:7:3, 90:9:1 of 3MPS: TEOS: GPTMS, 100% 3MPS)

Figure 3.8 shows that as the GPTMS content increased, the intensity of the FTIR peak at 1100 cm^{-1}, which corresponds to silicon dioxide vibrations, increased while the silanol peak at 3200~3600 cm^{-1} decreased. The peaks were normalized to the peak height of the thiol group in 3MPS, which remained constant in the samples. This result supports the previous observations that the methanol permeability was lowest at 3 mol%, since a

more complete silicon dioxide matrix will likely block methanol transport compared to the samples with a greater number of hydrophilic silanol groups.

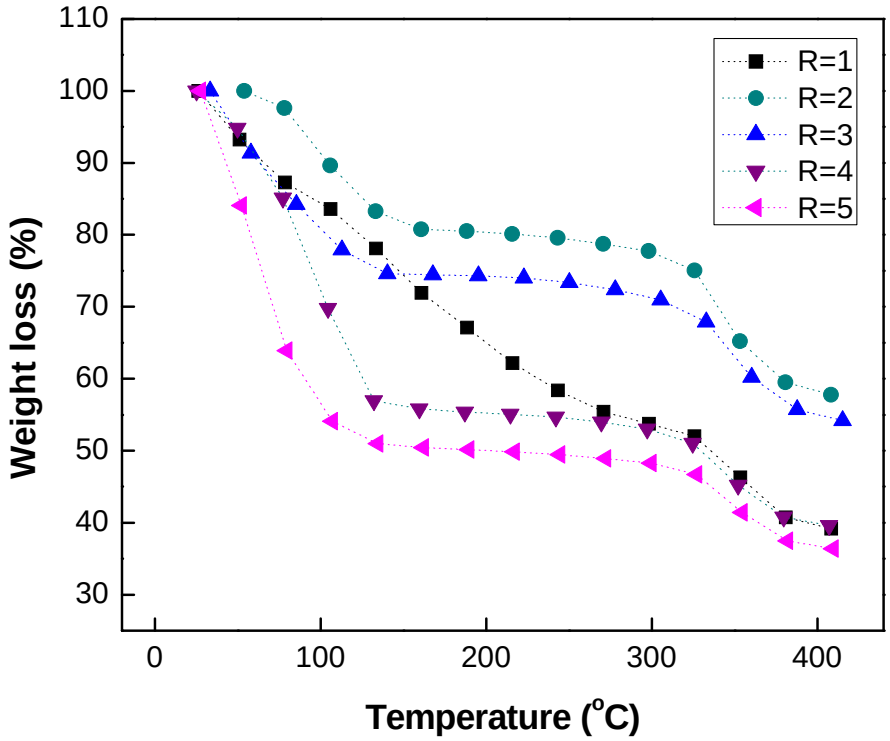

Figure 3.9: Thermogravimetric analysis of glass membranes synthesized by varying the molar ratios of water to silicon (R) from 1 to 5

One of the important parameters in the reactivity of the sol-gel is the amount of water. The effect of water-ratio on the glass membrane structure has been investigated by varying the mole ratio of water-to-silicon (R) from 1 to 5 and carrying out the sol-gel reaction, holding other variables constant (4 hr sol-gel reaction, 90-7-3mo% 3MPS-TEOS-GPTMS, curing temperature at 60°C, 100°C, 150°C, and 225°C for three hrs at each temperature, 3 hrs oxidation in hydrogen peroxide at 60°C). As seen in Figure 3.9, the weight loss in the TGA was fairly linear for a water ratio of R=1. The thermal

instability in the final film was likely due to insufficient water in the sol-gel for the gelation reaction. When R was increased from 2 to 5, the weight loss at 100°C was due to evaporation of excess water and methanol. Higher values of R resulted in more excess water and methanol (17.95% loss for R=2, 24.89% loss for R=3, 41.28% loss for R=4, and 48.36% loss for R=5). The glass membrane itself was stable up to 340°C. At R=5, the free-standing membrane cracked due to excessive water evaporation.

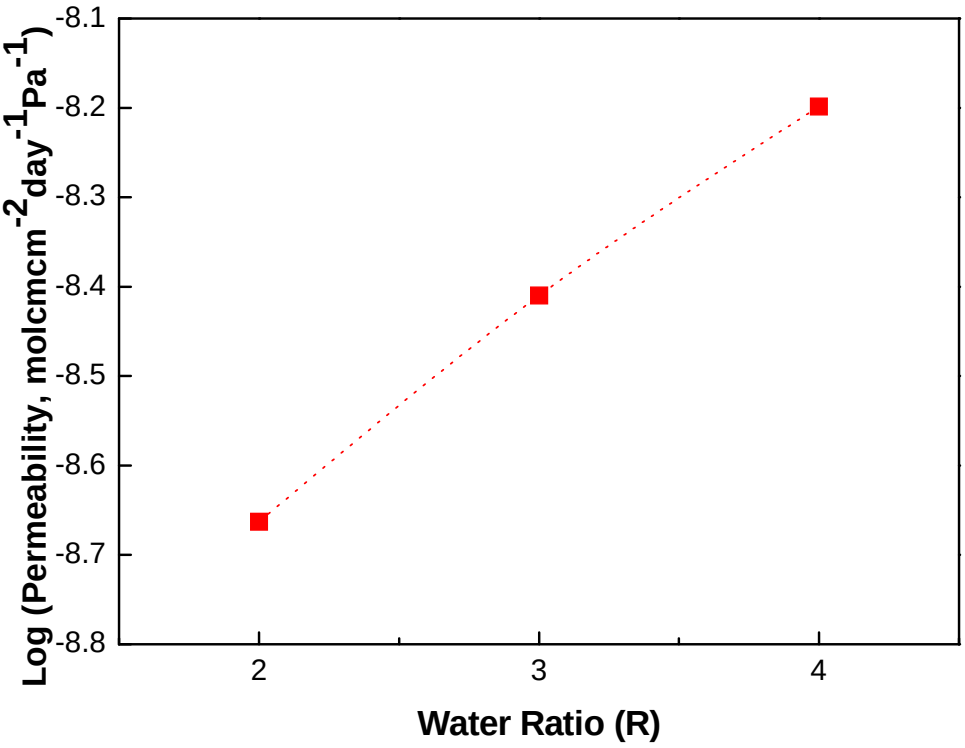

Figure 3.10: Methanol permeability as a function of water ratio to silicon (R)

The effect of the water ratio on conductivity and permeability of the glass membranes are shown in Figure 3.10 and 3.11. Figure 3.10 shows that the methanol permeability increased with an increase in R. The minimum permeability coefficient of 2.17×10^{-9} mol cm $cm^{-2}day^{-1}Pa^{-1}$ was achieved with an R value of 2. Figure 3.11 shows

that ionic conductivity decreased from 3.71 mS cm^{-1} to 1.46 mS cm^{-1} as the R value increased from 2 to 4. The highest selectivity in this experiment was achieved at R=2.

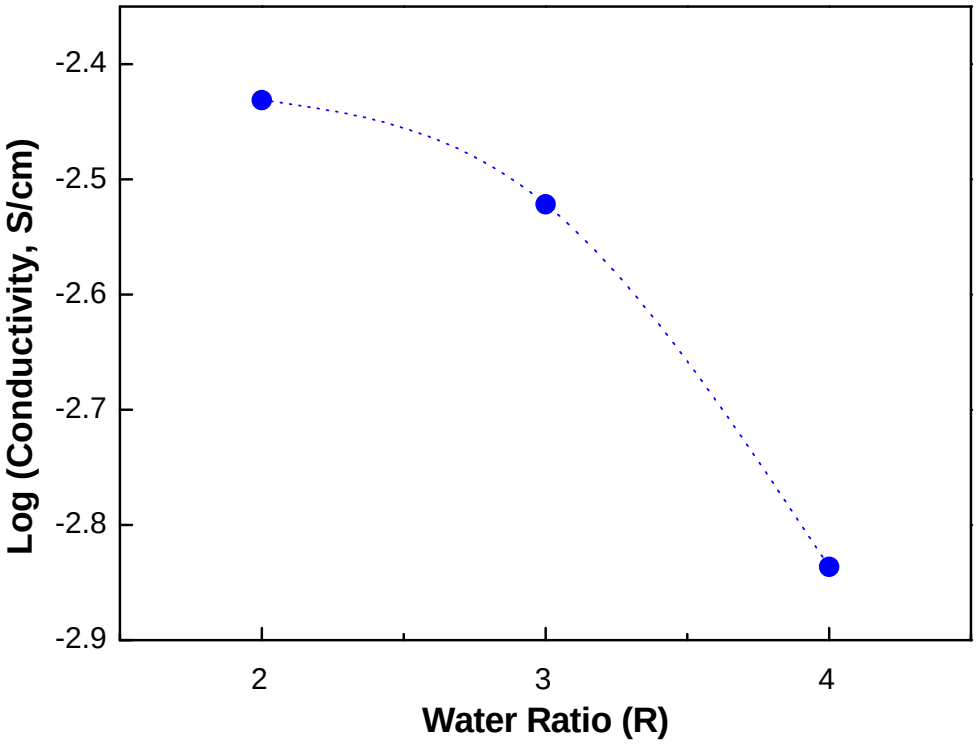

Figure 3.11: Ionic conductivity as a function of water ratio to silicon (R)

The difference in conductivity between the sol-gel glass and Nafion is of interest. The conductivities of two optimized glass membranes were measured as a function of temperature from 25°C to 90°C. Figure 3.12 shows that the conductivity of the glass membranes was less dependent on temperature than Nafion. The activation energy was calculated from an Arrhenius relationship, Equation 3.1.

$$\sigma = k \exp(-Ea/RT) \qquad (3.1)$$

Where σ is the conductivity, Ea is the activation energy, T is the temperature, R is the gas constant, and k is a pre-exponential term. The activation energy of the optimized glass membrane was 2.38 kJ mol^{-1}. This value was clearly smaller than the activation energy of Nafion, which was 9.34 kJ mol^{-1}. The water uptake of glass membranes was 4~6%, which was also much less than Nafion which has about 30% water [56].

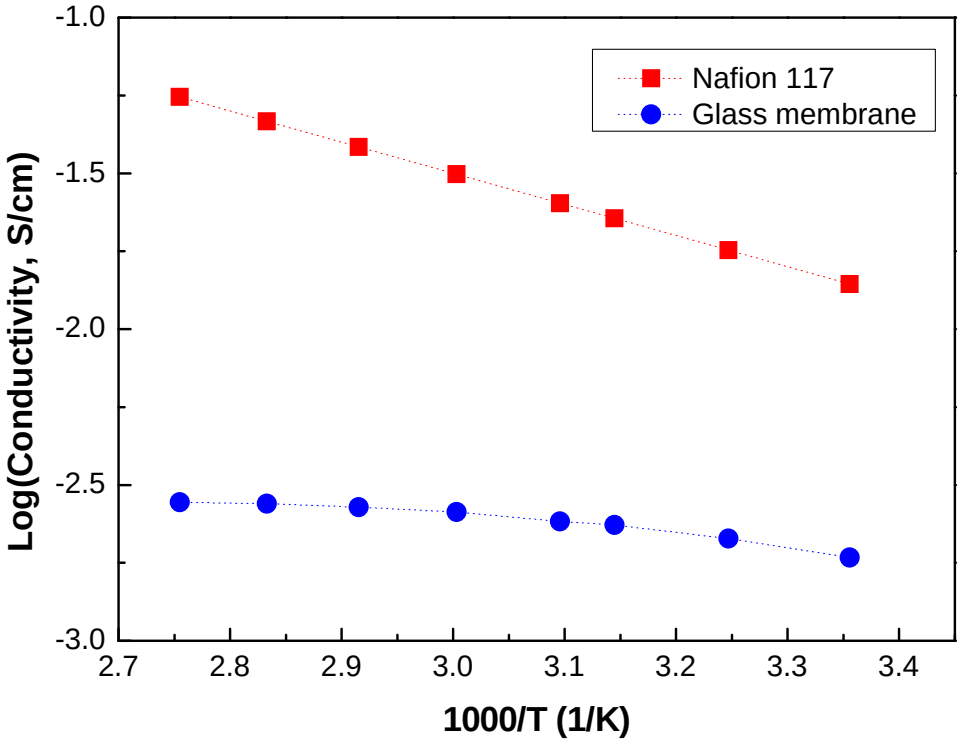

Figure 3.12: Ionic conductivity dependence on the temperature

An MEA was fabricated from a 90-7-3 mol% (3MPS-TEOS-GPTMS) glass membrane oxidized for 3 hrs in hydrogen peroxide. The compliant glass anode and cathode were prepared by incorporating the Pt/C nanoparticles in the silicon dioxide

matrix, and the glass catalyst were painted on both sides of the glass membrane.

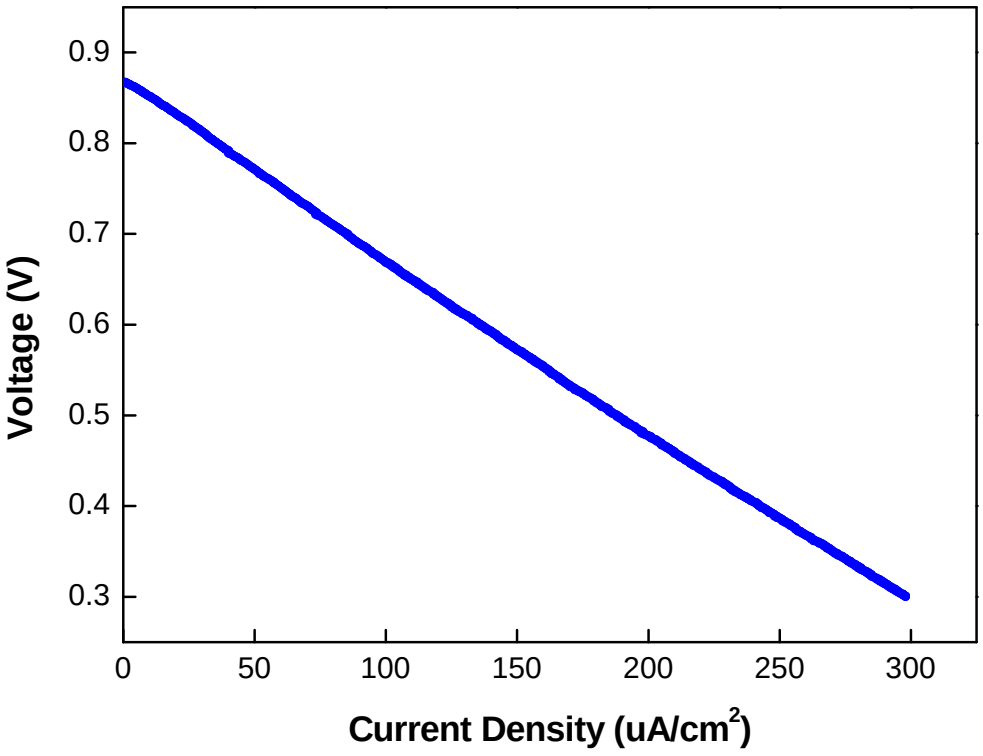

Figure 3.13: A linear polarization curve for a fully passive DMFC with a synthesized glass membrane and glass electrodes; 23°C 2 M methanol, 10 mV s^{-1}

The silicon dioxide matrix for the catalyst layer was made from the sol-gel reaction of 3-(trihydroxysilyl)-1-propanesulfonic acid (3TPS) and GPTMS. The sulfonic acid group in the 3TPS provided proton conductivity in the catalyst layer. The mole ratio of 3TPS and GPTMS was 1:1. Four mL of methanol and 3 drops of HCl were added to 5 mL of the mixture. After reacting the sol-gel for three hours, an equal mass of sol-gel and Pt/C were combined and mixed together for 1 hr. The mixture was painted on the

membrane and cured at 50°C for 12 hrs. The final Pt loading was 1 mg cm^{-2}. Additional studies on the metal catalyst and its optimization are addressed in the later chapters.

The electroless deposition of platinum was used to increase the total platinum loading on the MEA. The total amount of platinum deposited electrolessly was about 0.1 mg cm^{-2}. The electroless platinum also improved the sheet conductivity of the MEA, as described previously [48]. Figure 3.13 shows the polarization curve for a passive (no recirculation) DMFC operated at room temperature with 2 M methanol as the fuel at the anode and an air cathode. The open circuit voltage was 868 mV and the current density at 600 mV was 132 uA cm^{-2}.

3.4 Discussion

Sulfonic acid-functionalized glass membranes have been synthesized via a sol-gel reaction using 3MPS, GPTMS and TEOS for low-power DMFCs. The inorganic glass membrane is of interest due to its lower methanol permeability than polymer membranes. Minimizing the fuel loss through cross-over is the most important issue in long-life DMFCs. The goal of this study was to find the balance between the conductivity and permeability which determines the efficiency and performance. The conversion of thiol to sulfonic acid, contribution of the different sol components to the membrane properties, and water ratio in the sol have been investigated.

The overall methanol permeability coefficient of the samples, shown in Figure 3.4, 3.7 and 3.10, were on the order of 10^{-9} mol cm cm^{-2} day^{-1} Pa^{-1}, which is at least three orders of magnitude lower (improvement) compared to Nafion, 2.1 x 10^{-6} mol cm cm^{-2} $day^{-1}Pa^{-1}$ [22]. However, the ionic conductivities shown in Figure 3.3, 3.6, and 3.11 were

on the order of 10^{-3} S cm^{-1}, which is two orders of magnitude lower than Nafion, 0.08 S cm^{-1} [22, 57].

The particular behavior of conductivity and permeability for the glass membranes with respect to polymeric ones was shown in Figure 3.3 and 3.4. While the conductivity increased with thiol oxidation time (i.e. higher conversion of the thiol to sulfonic acid), the permeability decreased. This is contrary to the linear relationship between conductivity and permeability for polymeric membranes where an increase in conductivity leads to an increase in permeability. It is likely that the conversion of the thiol to sulfonic acid in the rigid glass matrix lowers the free volume while increasing the density of acid sites. Lowering the free volume reduces methanol permeability.

A similar behavior was observed by varying the mole fraction of GPTMS. Figure 3.6 and 3.7 show that the permeability decreased with additional GPTMS (zero to 3 mol% GPTMS), while the ionic conductivity increased with increasing GPTMS. The additional GPTMS provided a greater fraction of silica matrix, Figure 3.8, and likely less free volume. Less free volume results in lower methanol permeability and closer packing of the sulfonic acid groups providing a pathway for protons. The higher permeability and lower conductivity with excess water during reaction, Figure 3.10 and 3.11, can also be the result of added free volume due to trapped water during reaction.

Table 3.1, 3.2 and 3.3 shows the selectivity of samples examined in the different experiments here. The highest selectivity, 6.23, was achieved with an oxidation time of 3 hrs, a membrane composition of 90-7-3 mol% 3MPS-TEOS-GPTMS, and an R ratio of 2. For comparison, a Nafion membrane has a conductivity of 0.08 S cm^{-1} and permeability

Table 3.1: The effect of oxidation time on selectivity

Oxidation time(hr)	Selectivity
0	4.54
2	5.50
3	5.73

Table 3.2: The effect of mol% GPTMS on selectivity

mol% of GPTMS	selectivity
0	5.14
1	5.34
2	5.41
3	5.73
4	5.39

Table 3.3: The effect of water ratio on selectivity

water ratio	Selectivity
2	6.23
3	5.89
4	5.36

of 2.6 x 10^{-6} mol cm $cm^{-2}day^{-1}Pa^{-1}$, resulting in a selectivity of 4.48. Thus, the glass membranes had a 56 times improvement (linear scale) in selectivity compared to Nafion.

Finally, the energy conversion efficiency of a DMFC with a glass membrane can be compared to a Nafion membrane, using the energy loss analysis presented previously [23]. Figure 3.14 shows the two relationships in the case of the optimized glass membrane with a selectivity of 6.23 for a fuel cell operating at 200 uA and 0.5V. The total loss varies between 57.1% and 99.8% as a function of α. The lowest energy loss, 57.1%, can be achieved by adjusting the thickness and area of the glass membrane.

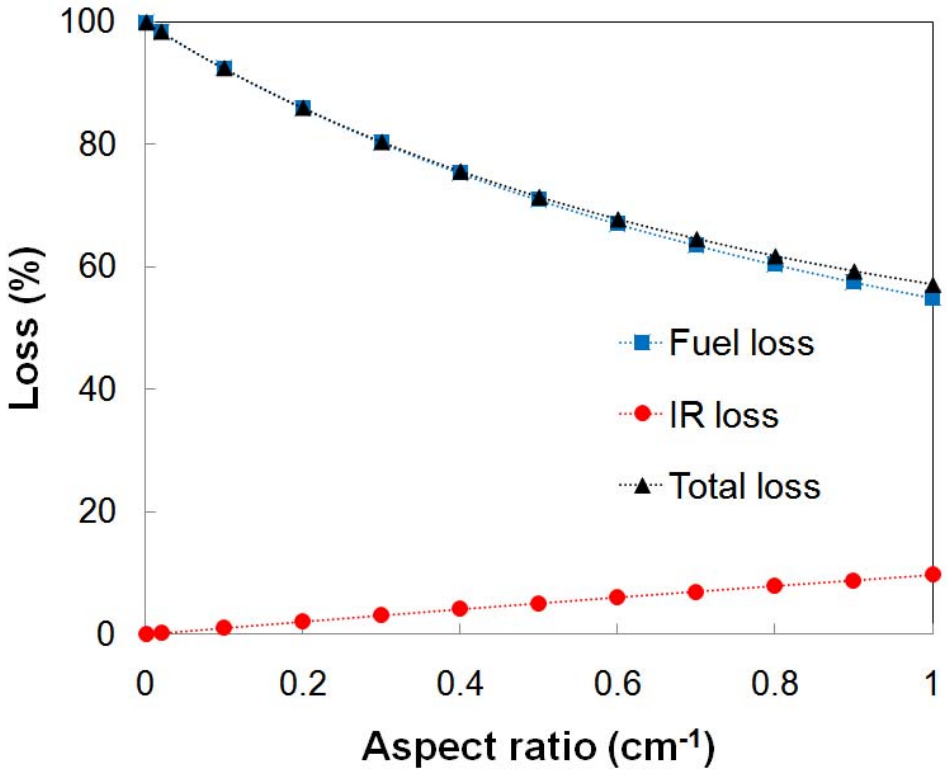

Figure 3.14: Energy losses as a function of alpha of optimized glass membrane with a selectivity of 6.23 when fuel cell operates at 200 uA and 0.5V

3.5 Summary

Inorganic glass membranes were of interest to reduce the methanol permeability for low power system application. High selectivity glass membranes have been successfully synthesized via sol-gel reaction using three different functional silanes, 3MPS, GPTMS and TEOS. The conversion of the thiol in 3MPS to sulfonic acid, contribution of the different sol components to the membrane properties, and water ratio in the sol have been investigated in terms of ionic conductivity and methanol permeability. The highest selectivity, 6.23, was achieved with 3 hr oxidation time, 90:7:3 of 3MPS: GPTMS: TEOS and R ratio of 2. The ionic conductivity of the optimized membrane was 3.71 mS cm^{-1} and the permeability was 2.17 x 10^{-9} molcm $cm^{-2}day^{-1}Pa^{-1}$**.** The fuel cell performance of glass membrane with the Pt/C-SiO_2 electrodes for both anode and cathode was demonstrated. The OCV was 868 mV and the current density at 600 mV was 132 uA cm^{-2}. The total energy loss of the DMFC decreased from 99.9% to 57.1% by replacing the Nafion to the synthesized glass membrane.

CHAPTER 4

SOL-GEL BASED PLATINUM-GLASS COMPOSITE ELECTRODE

4.1 Objective

In this chapter, novel catalyst layers are developed for low power direct methanol fuel cells. To utilize the inorganic membranes, compliant electrodes are important for stable fuel cell performance. Thin film electrodes were prepared by incorporating carbon-supported Pt nanoparticles into a silicon dioxide glass matrix. The SiO_2 was synthesized via a sol-gel technique where TEOS was hydrolyzed by H_2O in the presence of methanol. The electrode was exposed to an aqueous electroless plating bath in order to both increase the electrochemically active area and make electrical contact between the catalytic islands. Physical characterization of the Pt/C-SiO_2 glass composite electrodes has been done by SEM. The electrochemical performance of the resulting films for methanol oxidation has been studied ex-situ by cyclic voltammetry in sulfuric acid electrolyte. The work presented in this chapter has been previously published in the Electrochemical and Solid-state Letters [48].

4.2 Experimental

The Pt/C-SiO_2 composite electrodes were prepared by incorporating commercial carbon-supported platinum nanoparticles (E-TEK) into a silicate glass matrix. The glass was prepared by the sol-gel hydrolysis reaction between TEOS (Sigma-Aldrich) and deionized water in the presence of methanol in a 1:3:7 molar ratio. In order to increase the ionic conductivity of the film, phosphorus was added to the film with P_2O_5 so that the silicon-phosphorus atomic ratio was 19:1. During the hydrolysis reaction, the Pt/C nanoparticles were introduced to the system under vigorous agitation. The sol reaction was allowed to proceed for 30 minutes, then deposited on a glass substrate (Dow Corning) by the doctor-blade method and exposed to three 15 minute curing steps at 75, 150 and 275 ^{o}C, respectively, where the solvent was evaporated and the reaction completed.

Electroless deposition of Pt on the resulting Pt/C-SiO_2 films was accomplished in a modified aqueous, acidic Leaman bath [30, 58]. The composition of the bath is presented in Table 4.1. Also, the reaction was thermostated to 70 ± 0.2 ^{o}C. The electrodes were immersed in the bath for various times ranging from 15 to 1800 seconds. The electrical resistance of the resulting films was measured with a two-point probe by painting two 1 cm silver contacts onto the film, separated by 1cm. Physical characterization of the Pt/C-SiO_2 glass composite electrodes was done by scanning electron microcopy (Zeiss Ultra 60 FESEM).

Electrochemical investigations were performed at room temperature, 23 ^{o}C, with a PARSTAT 2263 (Princeton Applied Research) potentiostat. Cyclic voltammetry was performed in a three electrode cell with the prepared thin film electrodes as the working

electrode, Pt foil (Sigma-Aldrich) as the counter electrode and a saturated calomel (CH Instruments) reference electrode (SCE). All voltammograms were obtained in 0.5 M H_2SO_4 electrolyte and were electrochemically cycled at least 20 times between 0.25 and 1.0 V vs. SCE to both clean and activate the surface until repeatable voltammograms were obtained.

Fuel cells were prepared by painting the cathode and appropriate anode catalyst layers onto an electrolyte-impregnated substrate and drying at 150 ^{o}C for 30 minutes. The electrolyte-filled substrate was prepared by soaking a 1 mm thick porous glass frit (Ace Glass) in Nafion® dispersion (DE 520, Dupont) for 30 minutes and exposing it to a 150 ^{o}C curing step for 90 minutes. The process was repeated 10 times in order to fill a sufficient amount of the void space in the substrate with the polymer electrolyte. The conventional anode and cathode catalyst inks and were made with 40 wt % Pt/C and contained 15 wt % Nafion® after drying.

4.3 Results and Discussion

A SEM micrograph of the doctor blade deposited Pt/C-SiO_2 composite electrode is shown in Figure 4.1. The films appear to be high quality and have several characteristics that are advantageous to catalytic layer. First, it is clear from Figure 4.1 that the film is highly porous, with a mean pore size of approximately 150 nm. It also appears from the micrograph that the composite film is homogeneously distributed. Film thickness measurements with a DEKTAK 3 Surface Profilometer show that the film thickness was 1.9 ± 0.2 μm. Finally, the film also showed excellent adhesion to the glass substrate, immune to abrasion testing, which indicates that the sol-gel glass likely forms a

chemical bond with the substrate, continuing the oxide lattice. However, in order to utilize the catalytic material as well as collect the current, the electrical resistance of the layer should be sufficiently low so that minimal energy is wasted conducting the current. Measurements taken with a two point probe indicate that the sheet resistance of the raw deposited catalyst layer is in excess of 5000 Ω cm^{-2}.

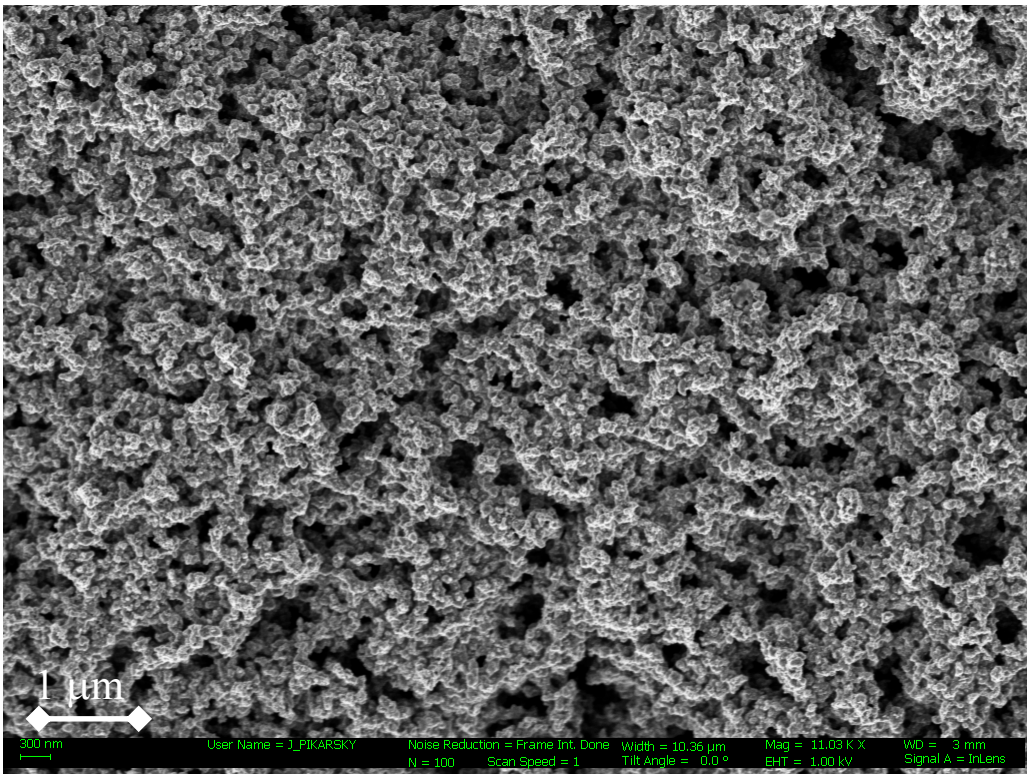

Figure 4.1: Scanning electron micrograph of Pt/C incorporated SiO_2 thin film; 11 kX magnification.

In order to determine the role that the catalyst distribution within the composite layer plays in the elevate sheet resistance, split in-lens and backscatter scanning electron micrographs are shown in Figures 4.2(a) and 4.2(b), respectively. From the backscatter micrograph, where large, conductive elements, like Pt, are easily seen as spots with higher brightness intensity, it is clear that though some of the islands are over 100 nm in

diameter, most of the platinum islands are have diameters on the order of 5 nm and are separated by approximately 25 nanometers of glass. Though the glass has been made to be ionically conductive by adding small amounts of phosphorus, the electrical resistance is quite high and the film remains a true dielectric.

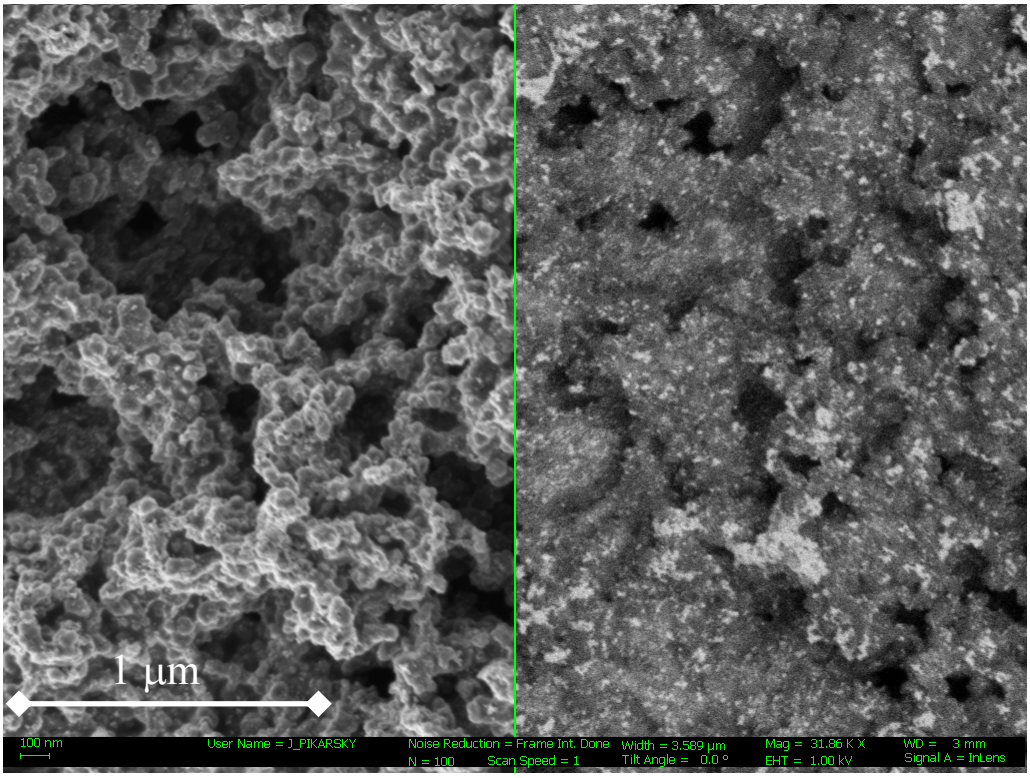

Figure 4.2: Split in-lens (a) and backscatter (b) scanning electron micrographs of Pt/C incorporated SiO_2 glass films; 32 kX magnification. The bright spots in the backscatter micrograph show the Pt catalyst distribution.

Therefore, the film can be described as distributed conductive islands separated by a dielectric. Though this is also the case in conventional membrane electrode assemblies, where the SiO_2 glass is replaced by an ion-conducting polymer, traditional catalyst layers are deposited onto conductive surfaces such as carbon cloth or paper, where the electrons are conducted a short distance from the catalyst to the conductive

substrate gas diffusion layer. In this case the catalyst is deposited on a non-conductive substrate, which means that the charge must be carried from catalyst to catalyst over the entire length of the material; with a 5 nm particle size and 25 nm separation, it is no surprise that the resistance is prohibitively high.

Therefore, in order to de-isolate the particle and increase the electrical conductivity, we must consider a way to connect the catalyst particles to one another. Though several methods can be considered, an optimal choice would not only connect the conductive islands, it would also utilize the void space in the pores and potentially increase the electrochemically active area. To this end, the method employed in this investigation is electroless Pt deposition in a modified Leaman plating bath [58]. Unlike most physical deposition methods, electroless deposition in an aqueous bath will allow Pt to be deposited both on top of as well as deep within the porous structure. Also, the existing platinum islands will be the deposition anchors, facilitating island growth and coalescence.

During the electroless process, the surface will likely go through several transitions. Initially, the catalyst is well distributed, though the particles are too far apart to be electrically conducting, forcing the catalytic current to travel through the dielectric. As Pt deposition ensues and islands grow, the pore size will decrease, thus increasing the electrochemically active area, though likely decreasing catalyst utilization. However, the resistance should still be high as the current is still carried through the glass separation layers. Then, after some time, the islands should grow until they just barely merge, reaching the so-called propagation threshold. This should be met with a drastic decrease in the electrical resistance as the current is now passed through the Pt catalyst. This is the

likely optimum point for the available electrochemically active area. Further deposition should only decrease both the electrochemically active area and catalyst utilization, leading to decreases in the current as well wasting precious catalyst.

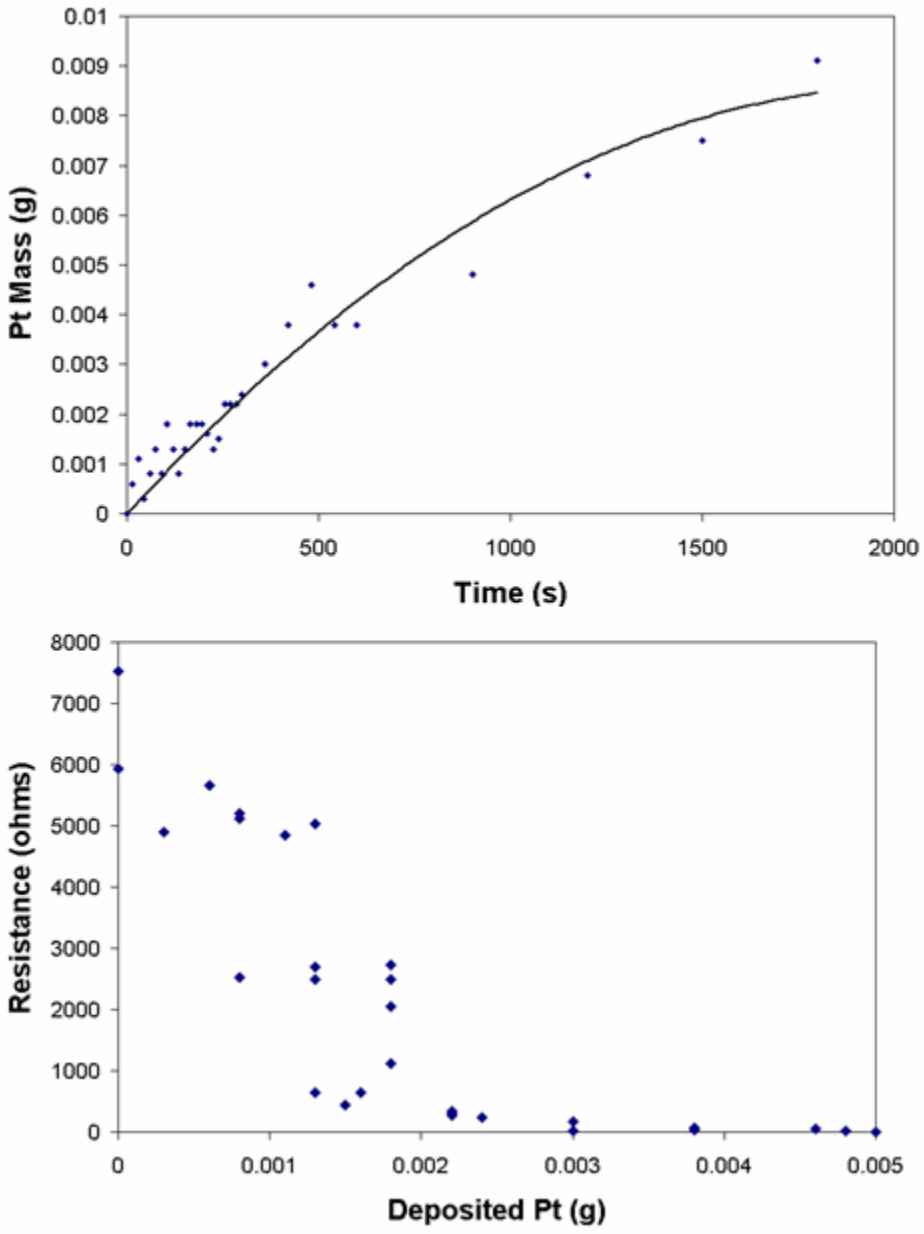

Figure 4.3: Pt mass increase (a) and sheet resistance decrease (b) of the catalyst-glass composite layer during the electroless deposition of Pt.

In order to observe this, the Pt mass and sheet resistance was measured for several samples, 2.0 cm^2 in area, and presented in Figure 4.3. The electrodes show the expected behavior where the Pt mass increased as a function of time (Figure 4.3(a)). Also, the resistance (Figure 4.3(b)) goes through an initial steady decrease, followed by an abrupt change at a deposition time of approximately 300 s, corresponding to approximately 1 mg Pt cm^{-2}. In order to observe the structural changes during the electroless process, several samples were prepared for various deposition times ranging from 0 s to 1800s.

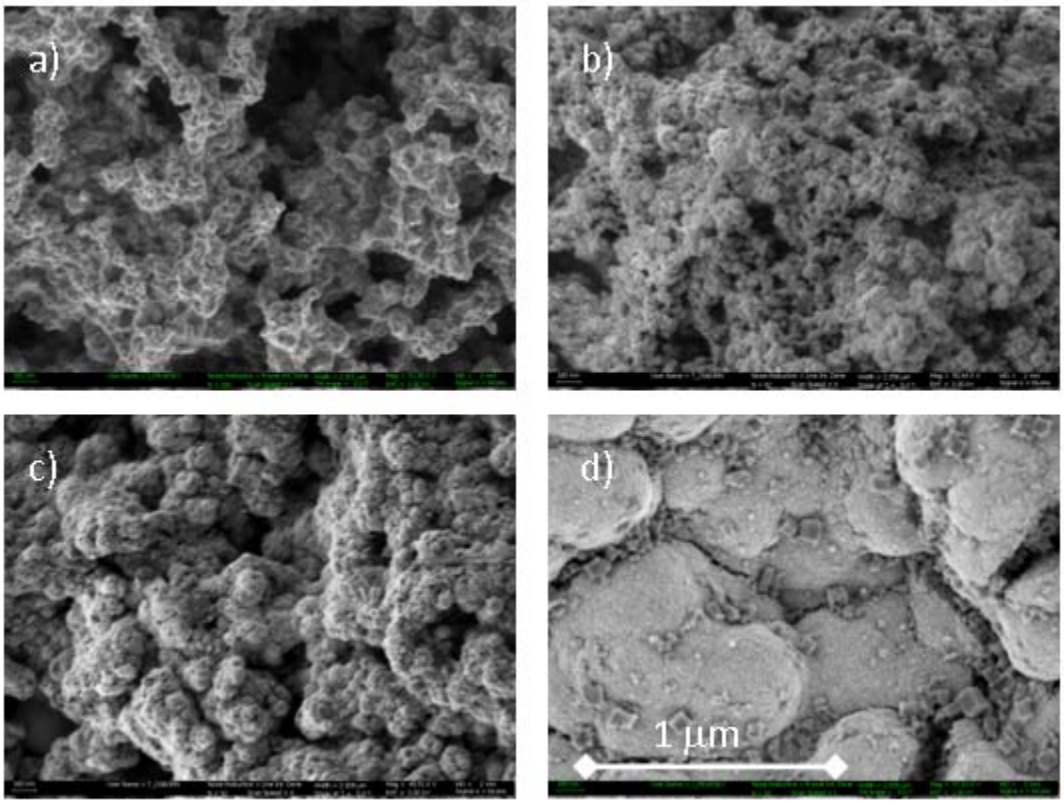

Figure 4.4: Scanning electron micrographs of Pt/C – SiO_2 glass thin-film electrodes following the electroless deposition of Pt for 0s (a), 180s (b), 300s (c) and 1800s (d); 50 kX magnification.

Figure 4.4(a) shows the raw electrode structure one with no deposited Pt, where the measured sheet resistance is in excess of 5000 Ω cm^{-2}. As expected, the structure is

identical to the one presented in Figure 4.2. Figure 4.4(b) presents a sample exposed to the electroless bath at 70 ^{o}C for 180s. It is clear from the micrograph that the film structure has been significantly changed. The islands are larger than the raw sample, typically around 20 nm, with islands as large as 50nm, and the average pore size has been decreased from 150 nm to approximately 100 nm, confirming the growth of the catalytic islands. However, from Figure 4.3, it is clear that the average film sheet resistance is still quite high, nearly 3000 Ω cm^{-2}, though more than 0.5 mg cm^{-2} of Pt has been deposited. After a 300 s deposition time, the islands have continued to grow and are typically 50 nm in diameter, though as large as 100 nm in some cases. The average pore size has further decreased to around 80 nm. As previously mentioned with a 300 s deposition, the film sheet resistance experiences a significant drop, down to approximately 100 Ω cm^{-2}, indicating that the film has reached the propagation threshold, indicating that the optimum deposition condition has been reached. Finally, the electroless reaction was allowed to proceed to near completion, 1800 s, and the bath utilization was approximately 95%. It is clear from Figure 4.4(d) that the electrode is significantly overplated, as expected. Island sizes are on the order of 1 micron and the pores have been completely covered.

Following initial film application and electroless Pt deposition, ex-situ cyclic voltammetry (CV) was performed in 0.5 M H_2SO_4 and 0.5 M MeOH at room temperature. A representative voltammogram for a 300 s electroless sample is given as Figure 4.5. It is clear that the deposited layer is highly active for the methanol oxidation reaction with forward reaction peak currents more than two orders of magnitude higher

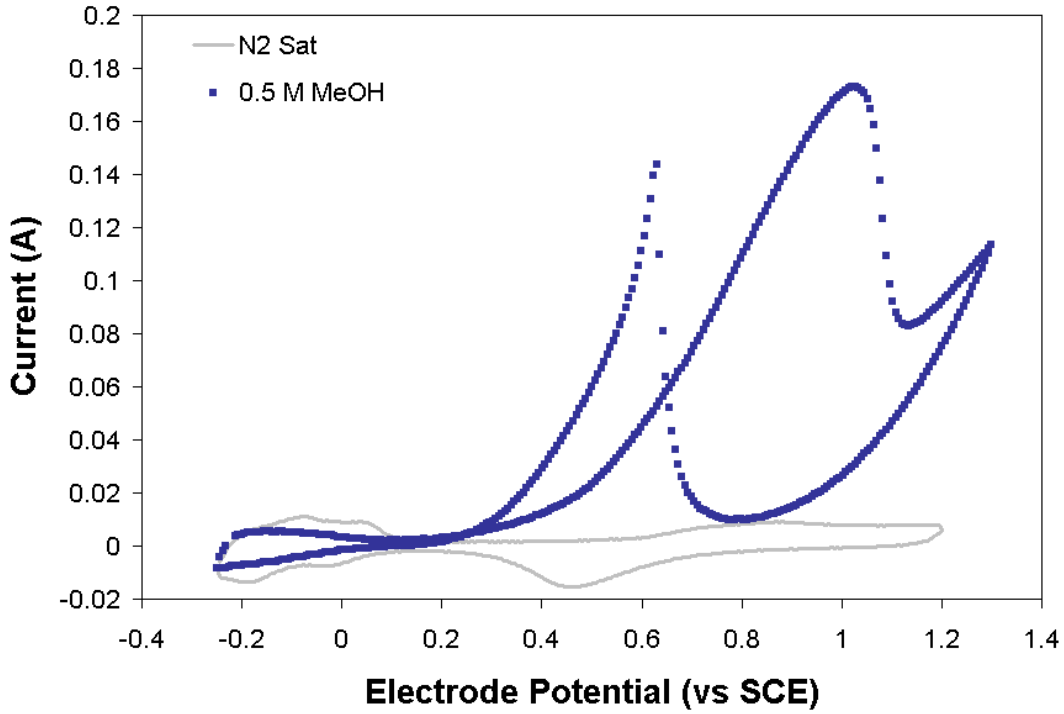

Figure 4.5: Cyclic voltammograms for 300s electroless Pt electrode in 0.5 M H_2SO_4 before and after the addition of methanol, 1 cm^2, 23 ^oC, 50 mV/s.

than planar electrodes under similar conditions [59]. This indicates that the roughness of the deposit is very high and that the pores are likely accessible to the solution phase. It is also seen that the reaction is initiated where expected, around 0.4 V vs. NHE, though the peak potential is nearly 200 mV higher than that observed in the literature. This is most likely due to the mass transport of both methanol and carbon dioxide within the pores at high scan rates. The mass transport effect is also evidenced by the sharp peak on the reverse scan at 0.5 V vs. SCE, where the remaining reaction intermediates are completely oxidized and CO_2 must desorb and escape through the porous matrix.

4.4 Summary

A complaint glass electrode was developed for utilizing the glass membrane. Pt/C-SiO_2 glass composite electrodes were prepared by incorporating the Pt/C into the gel matrix made of phosphorous doped TEOS. The catalyst particles were uniformly distributed and the composite electrodes were highly porous. However, it showed high electrical sheet resistance due to the isolation of catalytic islands by the silicon dioxide dielectric. In order to reduce the sheet resistance and collect the current, acidic Leaman bath was used to deposit Pt electrolessly within the composite catalyst. The sheet resistance dropped sharply by the deposition time and the electrochemically active area of the electrode layer was increased. It was found that the optimum Pt deposition time was 300 s, where the propagation threshold was reached. Consequently, the resulting electrodes showed higher methanol oxidation activity compared to planar electrodes.

CHAPTER 5

ELECTROLESS DEPOSITION AND CHARACTERIZATION OF Pt_XRu_{1-X} CATALYSTS FOR METHANOL OXIDATION

5.1 Objective

Pt_xRu_{1-x} has been known as the most efficient catalyst for methanol oxidation reaction, so it is important to apply the high activity Pt_xRu_{1-x} catalysts to the glass composite electrodes. Electrodeposition of Pt_xRu_{1-x} was first performed to investigate the deposition characteristics and performance as described in our previous work [60]. An empirical model for the Pt_xRu_{1-x} deposition process was developed and its kinetic parameters were estimated.

In this chapter, the electroless deposition of Pt_xRu_{1-x} catalysts is addressed and compared to the model developed. The acidic Leaman bath used for Pt deposition was modified for Pt_xRu_{1-x} deposition. An improved empirical relationship for deposit composition as a function of bath concentrations, temperature and surface potential is studied. The work presented in this chapter has been previously published in the Journal of Fuel Cell Science and Technology and the Israel Journal of Chemistry [29, 60].

5.2 Experimental

The electrodeposition of the Pt_xRu_{1-x} alloys was carried out on gold electrodes. The electrodes were immersed into an electrolyte which contained 3 g/100 mL HCl (Sigma Aldrich), 0.4 g/100 mL H_2PtCl_6 (Sigma Aldrich), and 0.1 g/100 mL $RuCl_3$ (Sigma Aldrich), which corresponds to a Pt-to-Ru mole ratio in solution of 1.6:1. The counter electrode was a 1 mm diameter platinum wire (Sigma Aldrich). The reference electrode was $Hg/HgSO_4$ (Pine Instrument Company) (E^o=0.64 V vs a normal hydrogen electrode (NHE)) and all potentials are reported vs. NHE. Chronoamperometric experiments were carried out at potentials between -1.1 and -0.3 V (-0.46 and 0.34 V vs. NHE) with a PARSTAT 2263 Potentiostat.

Electroless deposition of the Pt_xRu_{1-x} was conducted on the glass composite electrodes in a modified acidic Leaman bath [30, 58]. The aqueous bath contained 3.0 g/100 mL HCl, 0.2 g/100 mL 5-sulfosalycylic acid hydrate (Sigma Aldrich), 0.05 g/100 mL 1,3,6 sodium naphthalene trisulfonate tribasic hydrate (Sigma Aldrich) and 0.06g/100 mL benzene 1,3 disulfonate (Sigma Aldrich). The reducing agent was hydrazine dihydrochloride (1g N_2H_4*2HCl/100 mL) or formic acid (1g/100mL). Again, hexachloroplatinic acid and ruthenium (III) chloride precursors were used as the source for Pt and Ru ions, respectively.

The Pt_xRu_{1-x} electrodes were electrochemically characterized by cyclic voltammetry in a 1.0 M H_2SO_4, 1.0 M CH_3OH solution. The reference electrode for the cyclic voltammograms was $Hg/HgSO_4$ and the counter electrode was a Pt foil. The electrodes were cycled at least 20 times between -0.7 and 0.6 V vs. $Hg/HgSO_4$ until a reproducible voltammogram was achieved.

The composition of the deposited Pt_xRu catalysts was estimated using a Zeiss Ultra 60 scanning electron micrograph with an integrated EDX analysis. Light elements, such as nitrogen, sulfur and oxygen were neglected in the analysis. The primary electron energy for the analysis was 15 kV.

5.3 Results and Discussion

In the previous work [60], gold electrodes were immersed in the plating solution with a Pt^{+4}/Ru^{+3} ion ratio of 1.6 at various working potentials between -0.46 and 0.34 V at 23, 50, 70 and 90^{o}C. This was done in order to develop an empirical model (addressed in Chapter 2) and to determine the deposition parameters 'a' and 'b' in the equation 2.25. The calculated values for 'a' were 0.247, 0.262, 0.292 and 0.324 at 23, 50, 70 and 90^{o}C respectively. The value for 'b' was 4080.

The electroless metal deposition process occurs through a surface-catalyzed galvanic reaction between the metal ions and the reducing agent. The reductant and oxidant electrochemically react on active surface sites. The oxidation and reduction reactions can occur at different sites. Since the distance between active sites and the resistance of the conductive substrate are negligibly small, the surface potential is essentially constant and the reduction and oxidation occur at a single potential, often called the mixed potential. The resulting mixed potential is between the equilibrium potential of the oxidant and reductant such that the oxidation and reduction currents are equal.

Hydrazine was used as a reducing agent in the electroless process in order to assess the possibility of using a typical Leaman bath to codeposit both Pt and Ru. The

hydrazium ion is electrochemically active and its standard reduction potential is –0.23 V vs NHE [61]. The acid-base behavior and electrochemical oxidation are shown in Equations 5.1 and 5.2, respectively.

$$N_2H_4 + H_3O^+ \rightarrow N_2H_5^+ + H_2O \quad (5.1)$$

$$N_2H_5^+ \rightarrow N_2 + 5H^+ + 4e^-, E^o = -0.23V \quad (5.2)$$

Formic acid was also used as a reducing agent in the electroless process. The standard potential for formic acid oxidation is approximately -0.1V vs. NHE, Equation 5.3.

$$HCOOH \rightarrow CO_2 + 2H^+ + 2e^-, E^o = -0.1V \quad (5.3)$$

The standard potentials for hydrazine and formic acid are close to the lower end of the potential region of interest. However, a significant overpotential for the oxidation of hydrazine and formic acid is expected.

Several Pt/C-SiO_2 composite catalyst layers were prepared on glass substrates according to our previously described procedure [48]. The composite electrodes are homogeneous and porous, shown in Figure 5.1(a). Next, the electroless deposition of Pt_xRu_{1-x} electrocatalysts was carried out on the Pt/C-SiO_2 composite catalyst layers using the modified aqueous, acidic Leaman bath with hydrazine as the reducing agent.
In order to determine the electrode potential during the electroless process, several Pt/C-SiO_2 samples were immersed in the electroless bath at room temperature, 23°C. Four different bath compositions were investigated where the concentration of platinum and ruthenium ions in solution were adjusted such that their ratio (C_{Pt}/C_{Ru}) was equal to 1.6, 0.8, 0.4 and 0.2. A significant amount of metal was deposited on each sample, as shown in Figure 5.1 (b) (formic acid), in order to ensure a sample size large enough for accurate

determination of the composition using EDX. When used as a fuel cell anode, the amount of deposited metal may be different than the amount deposited here and would need to be optimized for electrical conductivity, active area, and porosity [48].

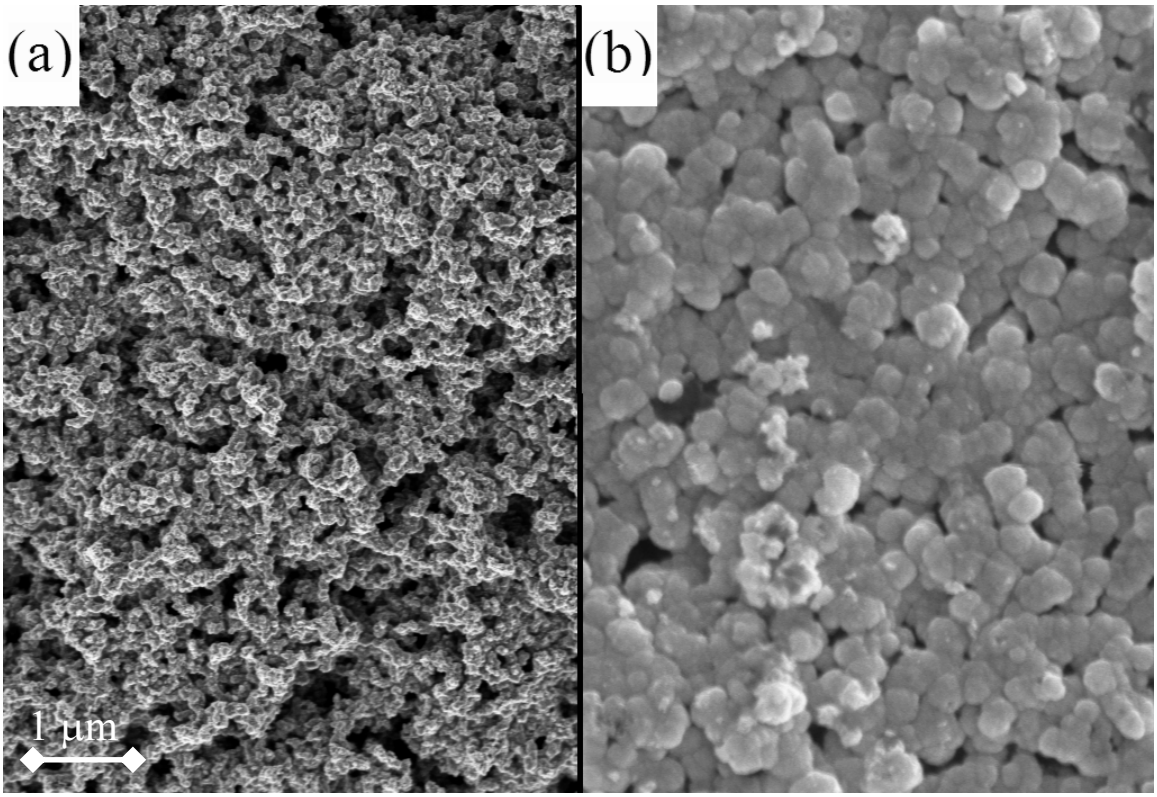

Figure 5.1: Anode catalyst layer before (a) and after (b) the electroless deposition of PtRu at 11000X and 60000X magnification, respectively.

The electrode potential in the empirical model was iteratively adjusted until an acceptable fit with metal composition was achieved. Here, the experimental data and empirical model agree well at approximately 0.40 V, as shown in Figure 5.2. This is consistent with expectations, where the overpotentials for both the anodic and cathodic reactions incur a significant overpotential. It should be noted that the surface potential could not be directly measured during deposition due to the extremely low electrical

conductivity of the Pt/C-SiO_2 electrolyte prior to reaching the percolation threshold where a significant amount of material has already been deposited.

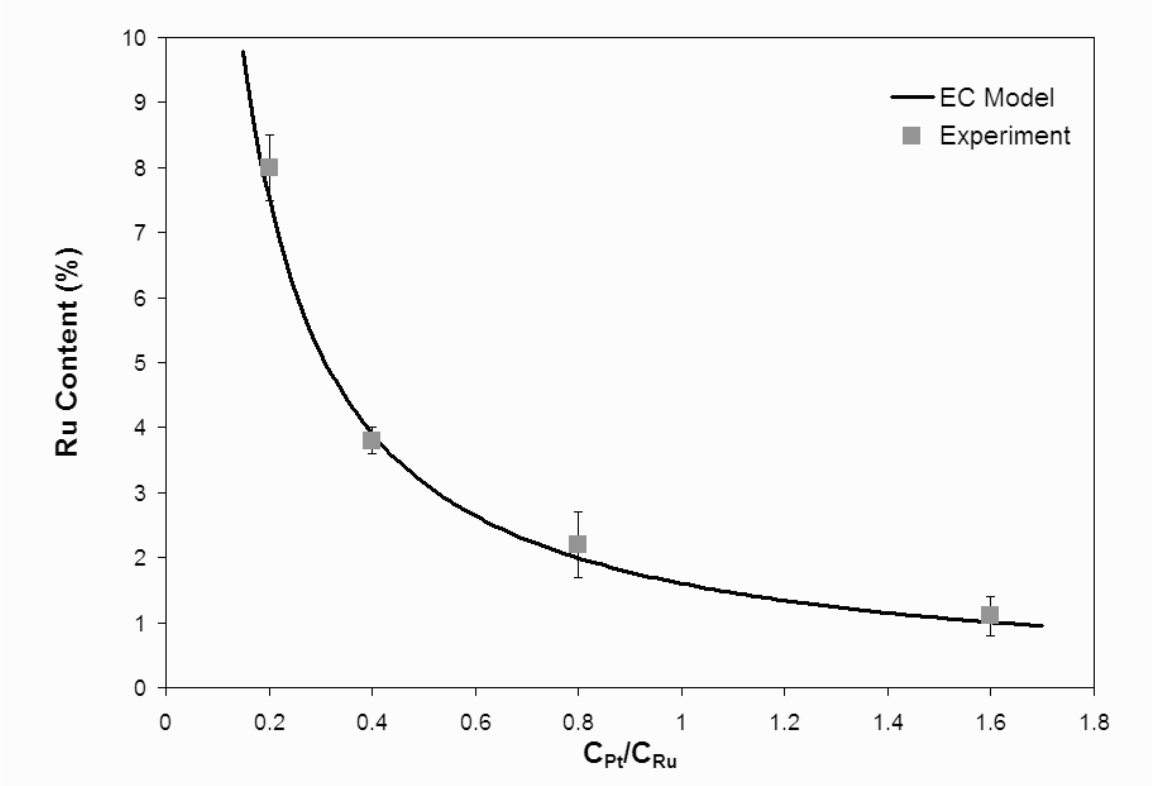

Figure 5.2: Agreement between the proposed deposition model at a surface potential of 0.4 V and experimental data for the spontaneous, electroless deposition of Pt_xRu_{1-x} with a hydrazine dihydrochloride reducing agent at various bath compositions, 23°C.

Unfortunately, even with a large excess of ruthenium ions in solution, the electroless deposition resulted in bimetallic layer with less than 8% Ru. Also, the empirical model suggests that C_{Pt}/C_{Ru} ratios of approximately 0.01 would be necessary to achieve equimolar deposition of the two metals and would be extremely sensitive to deviations in concentration. On the other hand, from the model parameters, it is expected that raising the temperature would provide a more controllable method by which to modify the deposit composition such that an optimum $Pt_{0.5}Ru_{0.5}$ could be obtained.

Pt_xRu_{1-x} was deposited at 90°C with a C_{Pt}/C_{Ru} ratio of 1.6, 0.4, 0.2 and 0.05. The resulting deposit compositions are shown in Figure 5.3. The deposit composition deviates from the values expected from empirical model with a large variance in the composition of the deposit at low C_{Pt}/C_{Ru} ratios. Also, it should be noted that after several minutes in the electroless bath at 90°C, the metal layer showed poor adhesion.

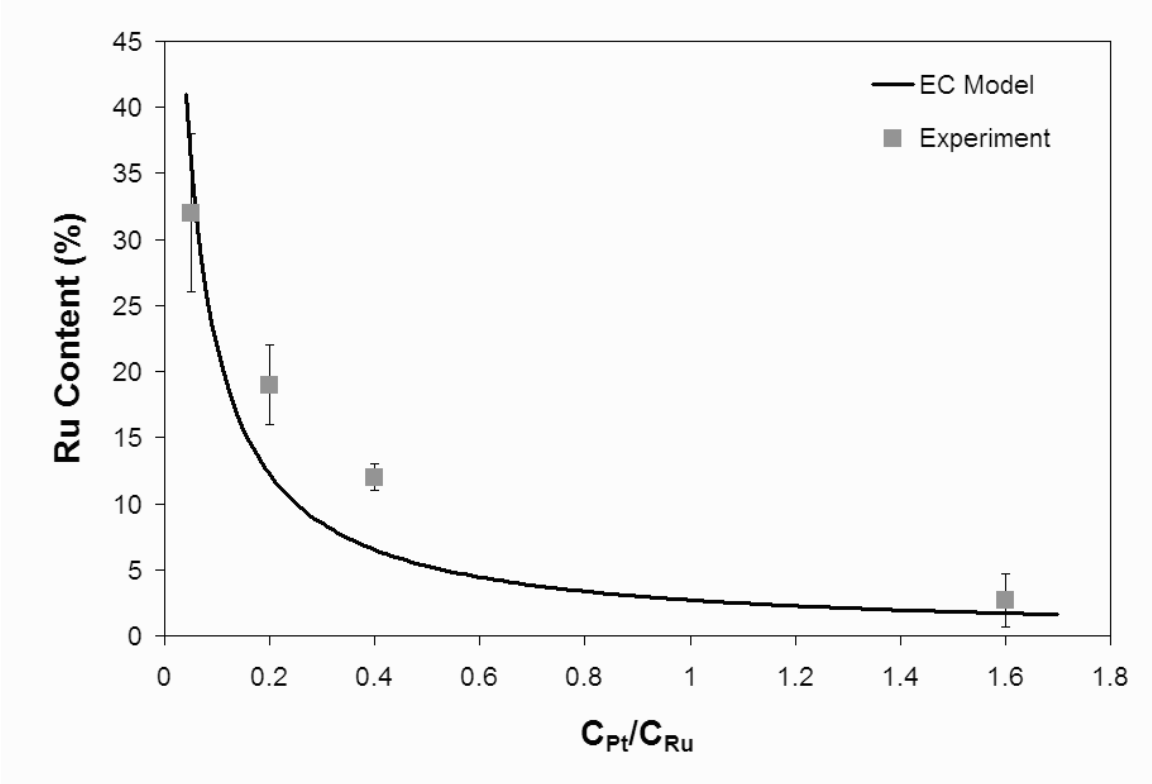

Figure 5.3: Model and experimental results for the electroless deposition of Pt_xRu_{1-x} with hydrazine dihydrochloride reducing agent and various bath compositions, 90°C.

Over only a few hours, the solution color turned from dark red, due to $RuCl_3$, to deep golden color. This is most likely due to the formation of a complex between ruthenium and hydrazine, which is favored at elevated temperatures. Specifically, $RuCl_3$ trihydrate readily reacts with hydrazine [61-63].

$$RuCl_3 \cdot 3H_2O \xrightarrow{N_2H_4} Ru(NH_3)_5 N_2^{+2} \quad (5.4)$$

This species can further reacted in the presence of water, Equation 5.5, or chloride, Equation 5.6.

$$Ru(NH_3)_5N_2^{+2} \xrightarrow{H_2O} Ru(NH_3)_5H_2O^{+2} \quad (5.5)$$

$$Ru(NH_3)_5N_2^{+2} \xrightarrow{Cl_2} Ru(NH_3)_6^{+2} \quad (5.6)$$

The formation of these ammoniacal species would significantly alter the deposition process, which was not accounted for in the model. The redox potential and kinetic parameters would be significantly different from the chloride complex.

Formic acid was investigated as an alternative reducing agent for electroless deposition of PtRu due to its favorable oxidation potential, solubility and electrochemical reactivity on Pt and PtRu surfaces [64]. Several Pt/C-SiO_2 composite electrodes were immersed in the electroless bath with formic acid as the reducing agent at 70°C. Several bath compositions were investigated with the C_{Pt}/C_{Ru} equal to 5.0, 1.0, 0.5, 0.67 and 0.2. This resulted in Pt_xRu_{1-x} deposits with a Ru content of 6.8 %, 35 %, 42 %, 52 % and 75 %, respectively. The ruthenium content of the electrodeposits was significantly higher when formic acid was used as the reducing agent instead of hydrazine, even though the Ru ion content in the bath and temperature were lower. The higher Ru content in the deposit suggests that the mixed potential during electroless deposition was more negative than with hydrazine. The mixed potential obtained from the empirical model developed in this study corresponds to approximately 0.15 V vs. NHE during the deposition process.

The platinum-ruthenium bath using formic acid as the reducing agent appears stable with time. The composition of the deposit vs. metal ratio in the bath is shown in Figure 5.4. The wide range of values and close correlation to the model shows that the

ruthenium ions are stable in the bath. The bath was also visually unchanged with time when aged at 70°C overnight.

The elemental distribution of platinum and ruthenium in the electrodeposit, shown in Fig. 5.1(b) was examined using EDX elemental mapping. This is shown in Figure 5.5 for a limited surface sampling. A uniform distribution of Pt and Ru were observed with no signs of metal segregation.

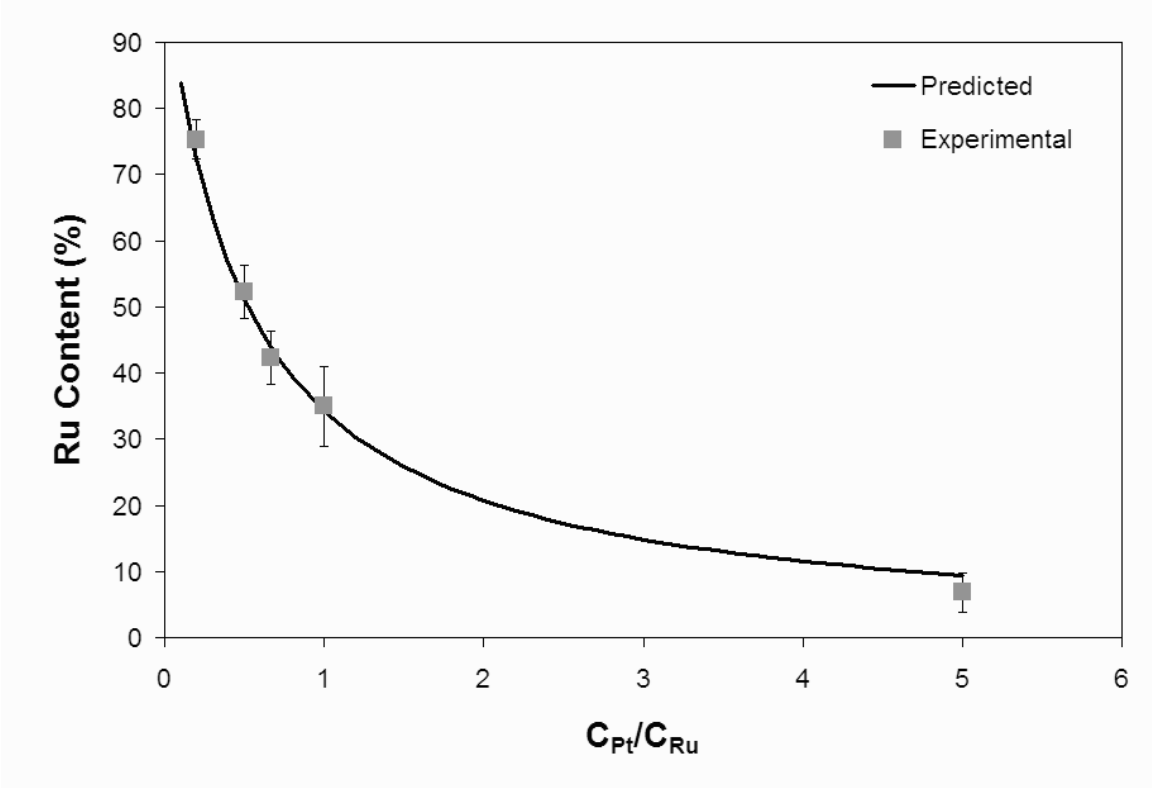

Figure 5.4: Model and experimental results for the electroless deposition of Pt_xRu_{1-x} with formic acid reducing agent and various bath compositions, 70°C.

Finally, the electroless deposition of ruthenium without platinum was investigated. Experiments were carried out using hydrazine or formic acid as the reducing agent. Only a very thin film of ruthenium was deposited on the Pt/C surface, after which no further metal was deposited. EDX showed little ruthenium metal was deposited on the

Pt/C surface. This leads to the conclusion that the catalytic surface for the reducing agent was platinum or the platinum-ruthenium alloy surface. Once the Pt/C surface is covered with ruthenium, the electrode is rendered essentially inert and no additional Ru is deposited. When platinum is codeposited with ruthenium, the electrodeposit was several micrometers thick.

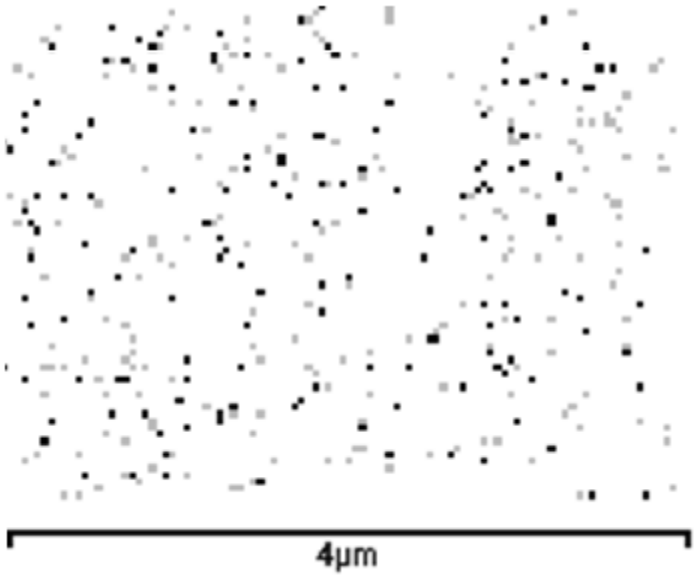

Figure 5.5: EDX map for Pt (■) and Ru (■) in the $Pt_{0.48}Ru_{0.52}$/C-SiO_2 composite catalyst layer

5.4 Summary

Pt_xRu_{1-x} bimetallic electrocatalysts for efficient methanol oxidation have been prepared by electroless deposition. The Leaman bath was modified for Pt_xRu_{1-x} deposition by varying the bath temperature or precursor compositions between the Pt and Ru. The model developed in the precious work was found to be accurate over a wide range of temperatures and bath compositions. Based on the empirical model, the surface potential was estimated to be 0.4V for hydrazine and 0.15 V for formic acid as the reducing agent during electroless deposition. Ruthenium forms an ammoniacal complex when hydrazine was used as the reducing agent leading to low bath efficiency and low Ru content. Formic acid was found to be an improved reducing agent to achieve 1:1 ratio of Pt and Ru at lower temperature.

CHAPTER 6

IMPROVED PtRu/C GLASS COMPOSITE ELECTRODE AND THE BLOCKING EFFECT ON MEHTHANOL CROSS-OVER

6.1 Objective

In this chapter, new SiO_2 matrix for glass composite electrodes was introduced to improve the properties of a glass ionomer and the Pt/C was replaced with PtRu/C for higher methanol oxidation activity. The silicon dioxide matrix was synthesized through the sol-gel reaction of 3-(trihydroxysilyl)-1-propanesulfonic acid (3TPS) and 3-glycidoxypropyltrimethoxysilane (GPTMS). The distribution of the PtRu/C particles can be controlled by changing the properties of the gel matrix. The effect of gelation time, mole fraction of reactants within the sol, curing temperature, and glass ionomer content were evaluated. Also, the adhesion of the catalyst layer on the membrane and catalytic activity for methanol oxidation have been characterized and optimized. The blocking effect of glass ionomer on methanol permeation was a special interest. The work presented in this chapter has been previously published in the Journal of Power Sources [65].

6.2 Experimental

The PtRu/C-SiO_2 electrodes were prepared by incorporating commercial PtRu/C catalysts into a silicon dioxide glass matrix. The PtRu/C catalyst (E-TAK) was 60wt% metal loading and 1:1 atomic ratio of Pt and Ru. The glass matrix for the catalyst layer was made via the reaction of 3TPS and GPTMS (Gelest Corporation). The mole percent of 3TPS-to-GPTMS was varied from 0, 50, 83, 90 to 95%. Four mL of methanol and 3 drops of HCl were added to 5 mL of the sol mixture. No water for the sol-gel reaction was added, since the 3TPS was obtained as an aqueous form with twenty fold excess water (by mole ratio). After reacting the sol for different gelation times (1-24 hrs), the gel solutions and PtRu/C were combined and mixed for 1 hr. The weight ratio of PtRu/C catalyst -to- glass was varied from 2 to 7, while maintaining the same PtRu/C loading in the electrodes (2 mg PtRu/cm^2). The catalyst and gel mixture was brush-painted on the membrane and cured at 80°C for 12 h.

The electroless deposition of the PtRu films was carried out on PtRu/C-SiO_2 electrodes in a modified acidic Leaman bath [30, 58]. The Pt/Ru electroless bath contained 3.3 g/100 mL HCl, 0.2 g/100 mL 5-sulfosalycylic acid hydrate (Sigma Aldrich), 0.05 g/100 mL 1,3,6 sodium naphthalene trisulfonate tribasic hydrate (Sigma Aldrich), and 0.06 g/100 mL benzene 1,3 disulfonate (Sigma Aldrich). The reducing agent was formic acid (1 g/100 mL). Hexachloroplatinic acid and ruthenium (III) chloride were used as the source of Pt and Ru ions, respectively. The preparation and characterization of the electrolessly-deposited PtRu bimetal has been described in the previous publication [29, 60]. The electroless deposition of Pt for the cathode electrode was performed using the

original Leaman bath with hydrazine dihydrochloride as a reducing agent. The Pt bath temperature was 70°C and the deposition time was 30 min.

The electrochemical experiments were performed with a PARSTAT 2263 (Princeton Applied Research) potentiostat. Linear sweep voltammogram (LSV) was carried out in a three electrode cell. Glass-based electrodes were fabricated on carbon paper and used as the working electrode with platinum foil (Sigma-Aldrich) as the counter electrode and a saturated calomel (SCE) reference electrode (CH Instruments). The voltammograms were obtained in an aqueous 0.5 M H_2SO_4, 1M methanol solution. The potential sweep was repeated at least 10 times between -0.4 and 1.5 V vs. SCE. The scan rate was 10 mV s^{-1}.

Adhesion of the composite electrode on the glass proton exchange membrane was evaluated by soaking the electrode/membrane structure in 1:1 vol% of water and methanol solution, and ultrasonicated for 1 h at room temperature. The weight loss of the electrode by ultrasonic vibration was measured. Methanol permeability of the bare membrane and MEA was determined by sealing the membrane to the open end of a methanol-filled vial. The loss of methanol was determined gravimetrically. The permeability coefficient was calculated using Equation 6.1.

$$P = \frac{N \times \delta}{\Delta P \times A} \qquad (6.1)$$

where P is the permeability coefficient of the membrane, Δp is the pressure drop across the membrane, A is the exposed membrane area available for fuel transport through the membrane, δ is the electrolyte thickness, and N is the number of moles lost by permeation. The relative error in the permeability coefficient was less than 2%. The relative methanol permeability was calculated by comparing the permeability coefficients

between the bare membrane and the same membrane with one electrode fabricated on it. The thickness of the membranes, with or without electrodes, was measured at five points and the average value is reported.

Impedance spectroscopy experiments were performed with a Perkins Elmer PARSTAT 2263 potentiostat. The membrane was placed between the two glass cells and filled with 1.0 M H_2SO_4 electrolyte. A platinum electrode was placed on each side of the membrane at a fixed distance from the membrane and connected to a potentiostat. The frequency of the impedance measurements ranged from 100 mHz to 1 MHz with an AC signal amplitude of 10 mV. The relative error in the conductivity measurements was about 0.2%, which was insignificant.

Fuel cells were prepared with the sol-gel based sulfonic acid-functionalized glass membrane. The synthesis and optimization process of the glass membrane has been described previously [26]. The PtRu/C-SiO_2 and Pt/C-SiO_2 catalysts were painted on the anode and the cathode, respectively. After curing both electrodes at 80°C for 12 h, the PtRu and Pt were electrolessly deposited on the anode and cathode, respectively. The linear polarization curves were obtained at a scan rate of 1 $mVsec^{-1}$.

6.3 Results and Discussion

The first step in the formation of a sol-gel based electrode is the creation of a stable, crack-free glass ionomer film, which can be loaded with metal catalyst and fabricated on the free-standing glass membrane. Among several candidates, 3-(trihydroxysilyl)-1-propanesulfonic acid (3TPS) has been selected, due to its similarity with 3MPS. The structural formula of the 3TPS is shown in Figure 6.1. The glass

ionomer was prepared via a sol-gel reaction with a 1:1 mole ratio of 3TPS-to-GPTMS. A four –fold excess of methanol by volume was added to the silane to make the mixture

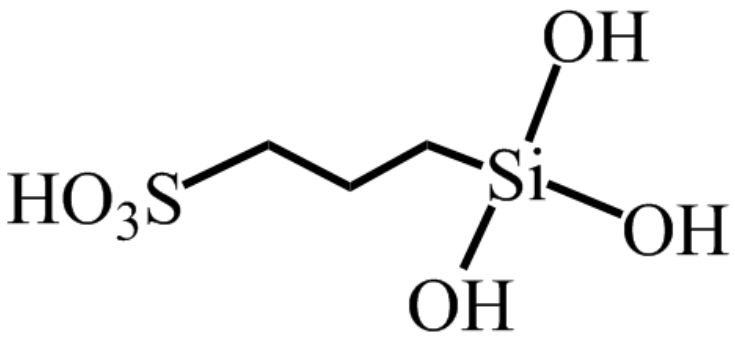

Figure 6.1: The chemical structure of 3TPS

miscible. The excess methanol also slowed the rate of sol-gel condensation. If the sol-gel reaction occurred too quickly, the heat generated from the reaction caused the temperature to rise which accelerated the condensation reaction rate resulting in cracks in the glass films. The PtRu/C nanoparticles were incorporated under stirring into the gel mixture for 1 h, described above, and painted onto the membrane surface. Uniform thickness glass electrode was formed on the membrane surface by curing the PtRu/C-SiO_2 gel on the membrane at 50°C for 12h.

The effect of sol-gel reaction time (gelation time) on the formation of a composite PtRu/C-SiO_2 film was investigated. Table 6.1 shows the glass electrode thickness depends on function of gelation time. The thickness of the catalyst layer increased from 7.8 μm to 32.6 μm, when the gelation time increased from 1 h to 24 h. The longer reaction time led to larger sol particles and the gel was more viscous, however, cracks were observed for reaction time greater than 6 h.

Table 6.1: The glass electrode thickness depending on the sol-gel reaction time

Reaction time (hr)	Thickness (μm)
1	7.8
3	9.5
6	12.5
9	16.8
12	24.5
24	32.6

The crack formation in the glass electrode also affected the methanol permeability through the MEA. Figure 6.2 shows the effect of gelation time on methanol permeability in the PtRu/C-SiO_2 catalyst layer. The additional glass layer in the electrode is expected to decrease the overall methanol permeability. The methanol permeability of a bare membrane was compared to one where one electrode was fabricated on one side of the membrane. When the sol-gel reaction time was increased to 3 h, the relative permeability was dropped by 62.1 %. As the gelation time increased, the larger sol-gel particles resulted in less free volume in the electrode structure. However, the relative permeability was increased when the reaction time was longer than 6 h. The cracks in the electrode film provided an easy pathway for methanol permeation. After 12 h reaction time, the permeability was similar to that of the bare membrane. That is, the electrode structure offered little resistance to methanol permeation due to the severe formation of the cracks.

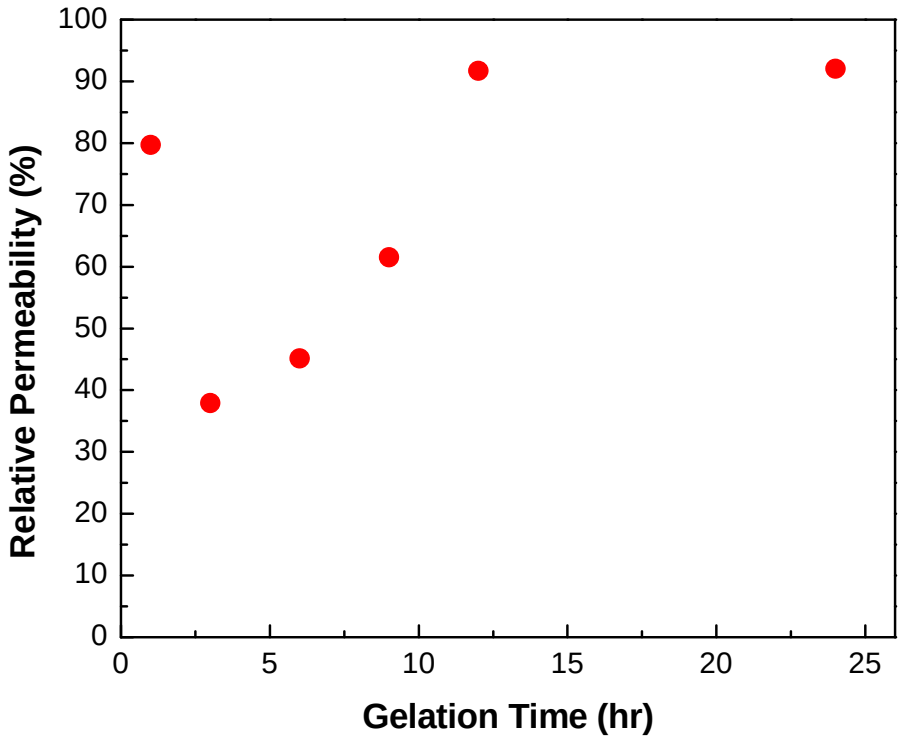

Figure 6.2: The relative permeability of the one-side MEA to that of the bare membrane as a function of gelation time

The effect of the 3TPS-to-GPTMS ratio was also investigated since they serve different functions within the sol-gel film. 3TPS provides the conductive, sulfonic acid moieties necessary for proton conductivity, and GPTMS provides epoxy cross-linking groups which enhance the mechanical strength of the catalyst layer and adhesion to the membrane. A higher mole fraction of 3TPS could increase the ionic conductivity, but may result in higher water adsorption and poor mechanical properties.

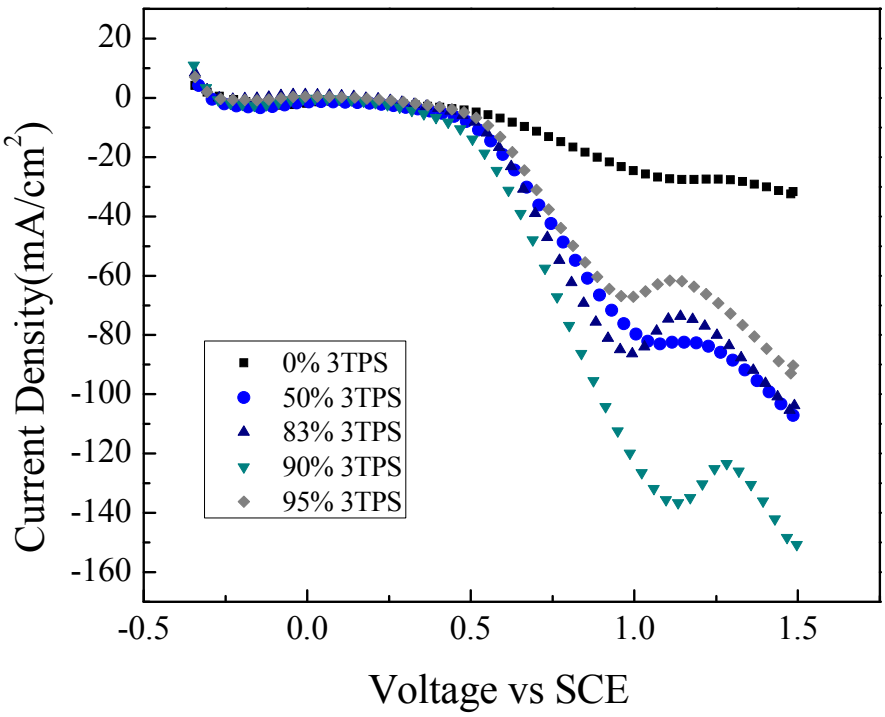

Figure 6.3: Linear sweep votammograms for different ionomer composition electrodes between 3TPS and GPTMS in 0.5 M H_2SO_4 and 1 M methanol, 1cm^2, 23°C, 50mVs^{-1}

The electrode activity of the catalyst on the membrane was investigated in an aqueous 0.5 M H_2SO_4/ 1M methanol solution. Figure 6.3 shows the LSV of the PtRu/C-SiO_2 electrodes with different ionomer compositions. The mole ratio of 3TPS-to-GPTMS was increased from 0 to 95%. The peak current increased with 3TPS content. The ionic conductivity of the ionomer was higher due to the higher sulfonic acid content. The maximum current density was -140 $mAcm^{-2}$ obtained with the 90 mol% 3TPS electrode (10 mol% GPTMS). This corresponds to 42,000 mAg^{-1} of PtRu/C catalyst. When the 3TPS was increased to 95 mol%, the current was lowered because there was an

insufficient amount of GPTMS to provide adequate adhesion of the electrode on the membrane. In this case, some of the catalyst nanoparticles fell off the membrane surface.

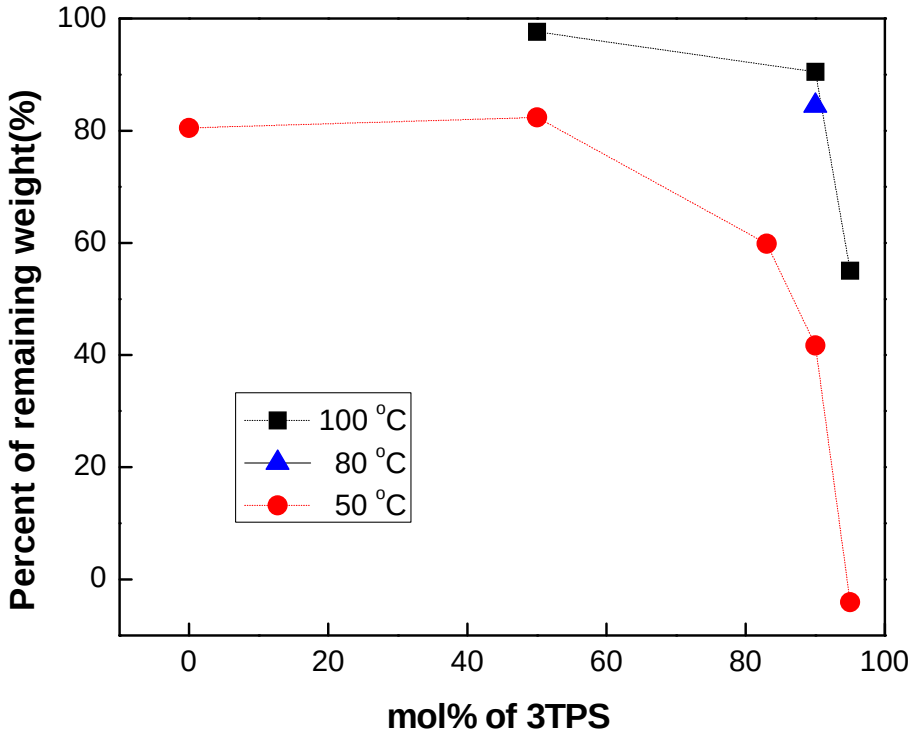

Figure 6.4: Percent of remaining weight of the electrode after ultrasonicating for an hour in methanol and water solution as a function of the curing temperature (50, 80 and 100°C) and different ionomer composition

In order to improve the adhesion of the glass electrode to the membrane, the PtRu/C-SiO_2 electrode was cured at a higher temperature, 100°C. The samples with different ionomer contents were soaked in the methanol/water solution (1:1 volume ratio), and ultrasonicated for 1 h. The weight of the electrode was measured before and after sonication. During the sonication, some of the catalyst layer flaked off the surface when the electrode adhesion was poor. Figure 6.4 shows the fraction of the electrode weight

remaining on the membrane as a function of the ionomer composition and cure temperature. Increasing the GPTMS content led to a higher catalyst content at both temperatures. The remaining weight of the samples cured at 100°C was higher than that of the samples cured at 50°C due to a larger extent of reaction in the electrode layer.

Although the adhesion of the glass electrodes on the membrane was improved by curing at 100°C, the sulfonic acid moiety was not stable at this temperature. The conductivity of the membrane decreased after curing at 100°C. The loss of conductivity is attributed to the fact that the $–SO_3H$ groups may react with the –OH groups to form –S-O-C bridges and water at high temperatures [16, 66]. Thus, the cure temperature was reduced to 80°C where the conductivity remained essentially constant. One can see in Figure 6.4 that for the 90% 3TPS sample the adhesion at 80°C was much better than that at 50°C. The remaining experiments were performed using membranes and electrodes with 90% 3TPS, allowed to gel for 3 h, and cured at 80°C.

The ratio of catalyst -to- glass ionomer was investigated, since it is highly desirable to have adequate sheet conductivity within the electrode and the correct three-phase boundary needs to be established [67-68]. Higher PtRu/C loadings generally result in higher electrochemical surface area and electrode activity. However, insufficient glass ionomer can lead to poor encapsulation and adhesion of the catalyst particles. Figure 6.5 shows that the relative methanol permeability and the sheet resistivity as a function of the catalyst-to-glass ratio. The relative permeability decreased significantly from 78.0 % to 28.8 % when the catalyst-to-glass ratio increased from 2 to 7. The excess glass in the catalyst layer assisted in blocking methanol cross-over. The sheet resistivity was 1.7 kΩcm when the catalyst-to-glass ratio was 2, however, it increased to 113 kΩcm when

the ratio was increased to 7. Although the glass ionomer was ionically conductive by virtue of the sulfonic acid content, the electrical resistance was high because it comes only from catalyst-to-catalyst contact.

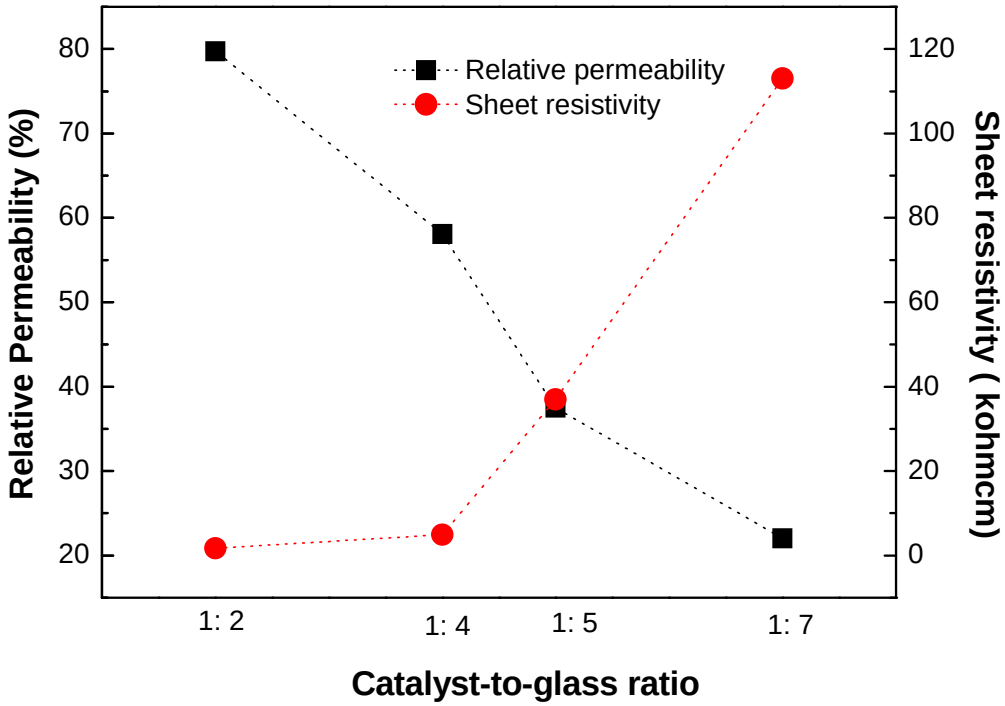

Figure 6.5: Relative permeability and sheet resistivity as a function of the glass ratio to catalyst

The electrochemical activity of the composite catalyst with different catalyst-to-glass ratios was evaluated by performing linear sweep voltammetry from negative to positive voltages, as shown in Figure 6.6. The electrode with a 1:2 catalyst-to-glass ratio provided the highest activity (highest current) in methanol in a potential range between 0.2 and 0.5 V vs. SCE. The 1:1 catalyst-to-glass sample had a higher metal content, however, the catalyst adhesion was poor and some of the catalyst particles flaked off the surface during use resulting in lower performance.

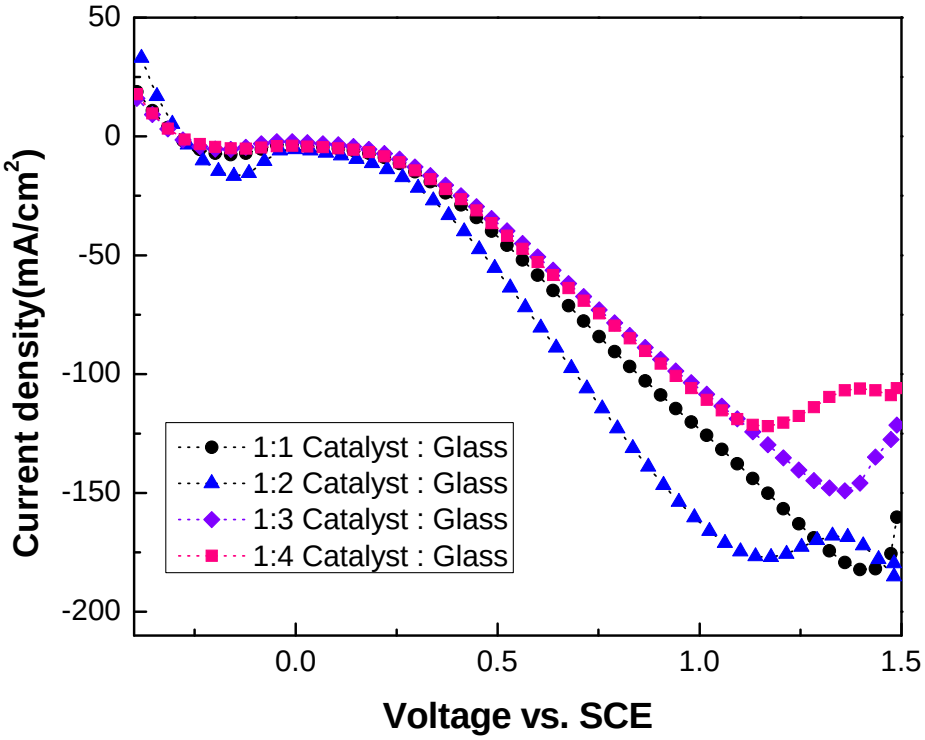

Figure 6.6: Linear sweep votammograms for different ratio of catalyst to glass electrodes in 0.5 M H_2SO_4 and 1 M methanol, 1cm^2, 23°C, 50mVs^{-1}

In order to decrease the sheet resistance by connecting the metal particles embedded in the glass ionomer, PtRu catalyst was electrolessly deposited onto the sol-gel fabricated electrode containing PtRu/C by using a modified acidic Leaman bath. As the metal islands grow, the void spaces between PtRu/C particles are reduced and the electrochemical area changes. Initially, the active area increases as PtRu/C islands merge together and the sheet resistivity drops. Once the islands have merged together, additional deposition yields larger particles but may not yield an increase in real surface area or electrochemical activity.

Table 6.2: The sheet resistivity (Ωcm) as a function of the deposition time and catalyst–to-glass ratio

	Catalyst –to-glass ratio			
Deposition time (min)	1:2	1:4	1:5	1:7
0	1450	7250	36500	121000
10	801	2550	8050	9650
20	250	2600	6900	7250
30	158	2450	5000	3700
40	106	1350	2200	3800
50		733	911	6550
60		146	237	10300

The catalyst-to-glass ratio in the PtRu/C-SiO_2 composite catalyst might affect the PtRu electroless deposition. The sheet resistivity was measured as a function of the deposition time for the samples prepared at different the catalyst-to-glass ratio from 2 to 7. Table 6.2 shows that the resistivity decreased with deposition time. At a given deposition time, the sample with lower glass ionomer content showed lower sheet resistivity than the sample with higher ionomer content. The sample with a 1:2 catalyst-to-glass ratio showed 106 Ωcm in 40 min deposition time, while the 1:4 and 1:5 catalyst-to-glass ratios required 60 min to achieve 146 and 236 Ωcm sheet resistivity, respectively. Only the 1:7 catalyst-to-glass ratio sample did not achieve lower than 1 kΩcm resistivity. It was observed that some of the deposited metal films delaminated, which caused an increase in

the resistivity after 60 min deposition time. This could be because the metal film deposited on top of the glass ionomer was less intimately attached to the glass electrode.

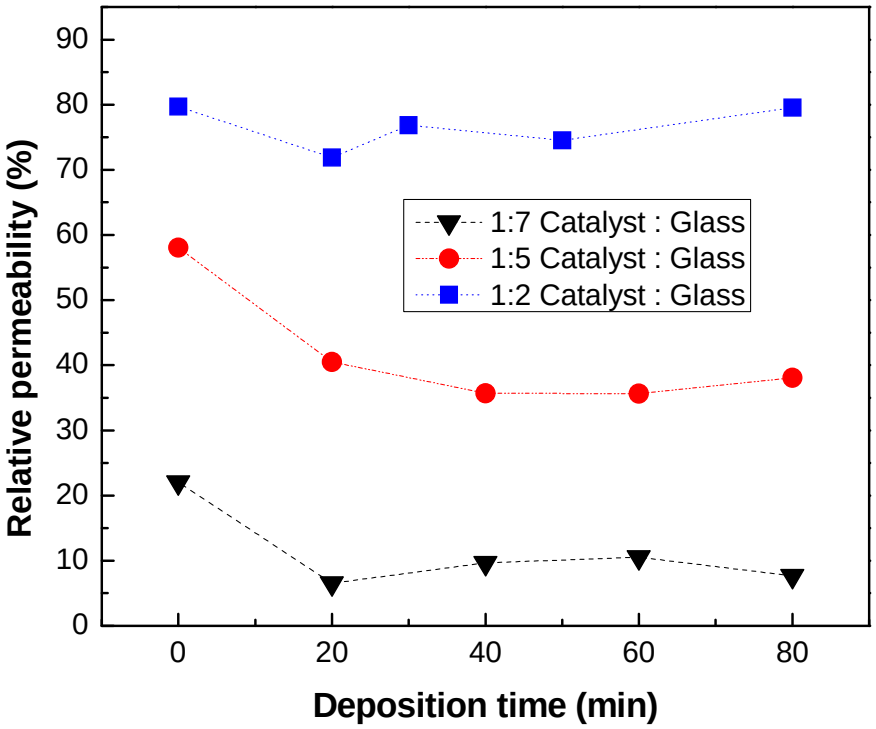

Figure 6.7: Relative methanol permeability as a function of the PtRu electroless deposition time with a different catalyst to glass ratio electrodes

The methanol blocking effect of the added, electrolessly-deposited metal layer was investigated. Glass electrodes with 1:2, 1:5, and 1:7 catalyst-to-glass ratios were prepared on one side of a bare membrane. The methanol permeability of the single sided MEA was measured as a function of electroless deposition time. As seen in Figure 6.7, the relative permeability of the single sided-MEA decreased by more than 15% when the PtRu deposition time was 20 min. This is due to metal ions filling the void space in the catalyst layer resulting in lower methanol permeability. However, the relative

permeability for both the 1:5 and 1:7 catalyst-to-glass samples did not decrease further. The additional metal film electrolessly-deposited on the metal-filled glass catalyst did not change the methanol permeability. The catalyst layer of the 1:2 catalyst-to-glass sample flaked off in the acidic electroless bath, so the permeability coefficient did not decrease from the initial value. It is clear that additional glass is necessary to hold the catalyst particles on the membrane during immersion in the acidic electroless bath, when immersed for a longer time.

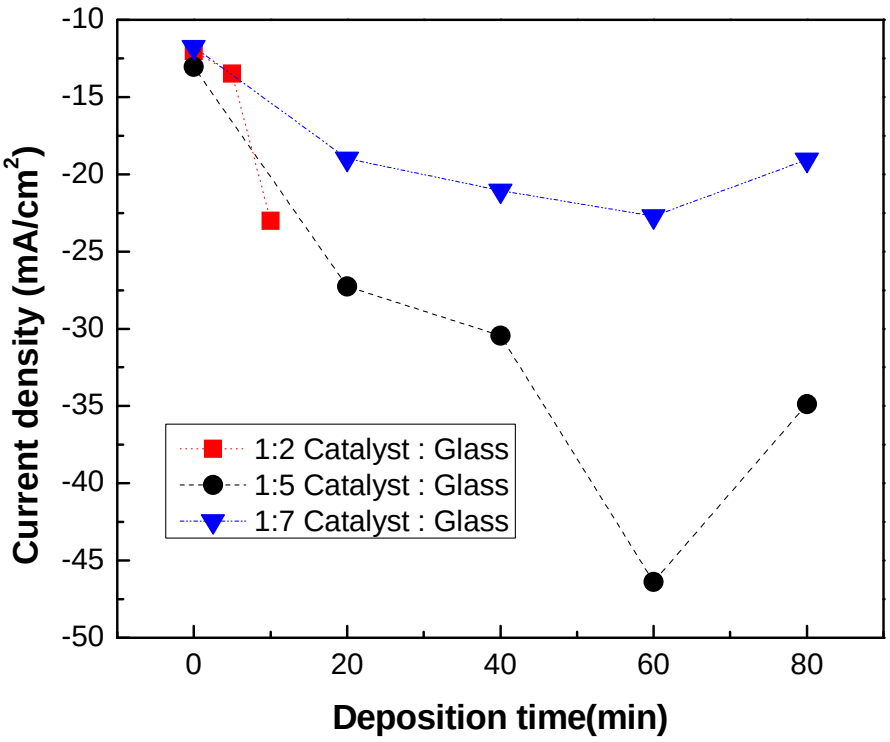

Figure 6.8: Current density at 0.2V (vs SCE) as a function of the PtRu electroless deposition time with a different catalyst to glass ratio electrodes

A decrease in methanol permeability is a benefit, if a corresponding decrease in catalytic activity does not occur when additional metal is electrolessly deposited. The

effect of additional metal layers on the electrochemical activity for methanol oxidation was investigated. Figure 6.8 shows the current density as a function of deposition time, ranging from 0 to 80 min. The current density was taken at 0.2V (vs SCE) from the voltammograms obtained in 0.5 M H_2SO_4/1M methanol solution, since it is potential range of interest for methanol oxidation in a fuel cell [69-70]. As seen in Figure 6.8, the current density increased with PtRu electroless deposition time, because a greater catalyst area is available for methanol oxidation. However, the current density decreased after 60 min. The excess electroless plating decreases the actual surface area of the catalyst, making large metal islands. Evaluation of 1:2 catalyst-to-glass sample was not possible because of poor adhesion of the catalyst layer to the carbon paper due to insufficient glass in the electrode mixture. From the results shown in Table 6.2, Figure 6.7, and 6.8, it is clear that the deposited metal improves three key parameters of the glass electrode, including the catalyst performance, methanol permeability, and the sheet resistivity.

The voltammetric results shown in Figure 6.3, 6.6 and 6.8 are valuable in assessing the activity of the PtRu surface for methanol oxidation, however, the configuration is different from an actual fuel cell because the protons produced in the oxidation of methanol do not travel through the membrane itself. In the fuel cell, protons are produced at the catalyst surface, and travel through the ionomer in the electrode and membrane. Protons generated at the anode migrate toward the cathode through the PEM glass membrane. In order to evaluate the effectiveness of the electrodes on the membranes for use in a fuel cell, an electrode was fabricated on one side of the membrane, which was used as the working electrode of a three-electrode cell. The counter electrode was placed on the opposite side of the membrane so that the protons

produced had to travel through the membrane, as they would in an operating fuel cell. The SCE reference electrode was located in the same compartment as the working electrode. A 1M methanol solution with 0.1M sodium sulfate was used in the anode side.

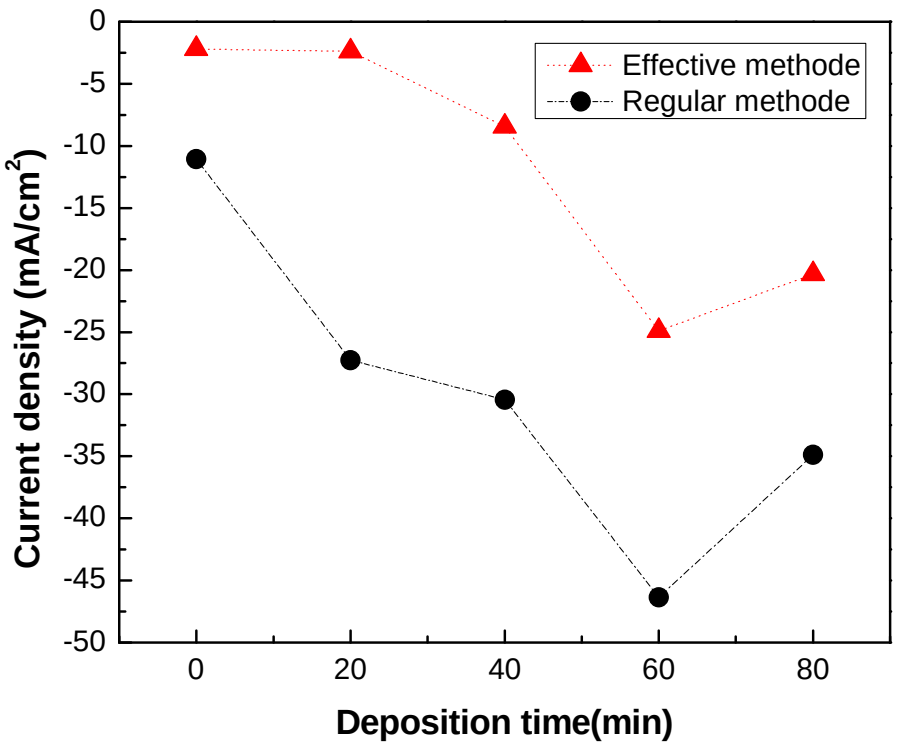

Figure 6.9: Current density at 0.2V (vs SCE) evaluated with more effective method as a function of the PtRu electroless deposition time with a 1:5 catalyst to glass ratio electrode, compared to the previous method

The compartment on the other side of the membrane was filled with the 1 M H_2SO_4 solution. IR compensation was used to correct uncompensated resistance. The optimized, 1:5 catalyst-to-glass electrode was used as the anode. Figure 6.9 compared the current densities from linear sweep voltammetry when the counter electrode is placed on the opposite side of the membrane to those from the previous experiments where the

counter electrode was placed in the same compartment as the working electrode, shown in Figure 6.8. When the protons had to flow through the membrane, the current density, at the same potential, and for the same electrode material, was lowered by about 50%.

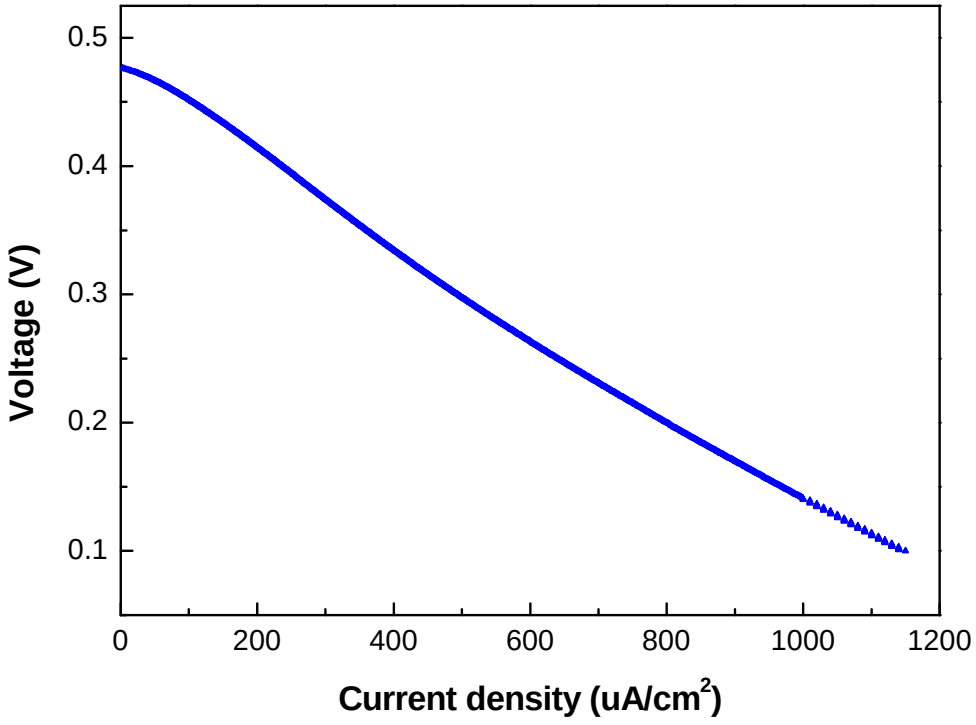

Figure 6.10: A linear polarization curve for a fully passive DMFC with a glass membrane and glass electrodes; 23°C ,0.5M methanol, 1mV/s

A glass MEA was fabricated with an electrode on each side using the sulfonic acid-functionalized glass membrane [26] in order to test the fuel cell performance with the optimized glass anode. At the cathode, the PtRu/C was replaced with Pt/C (40wt% metal loading) from the optimized glass anode. After curing both electrodes at 80°C for 12 h, the PtRu and Pt were electrolessly deposited on the anode and cathode, respectively. Figure 6.10 shows the polarization curve for a passive fuel delivery DMFC operated at

room temperature with 0.5 M methanol in the anode compartment and ambient air at the cathode without circulation at either electrode. The open circuit voltage was 476 mV and the current density at 400 mV was 236 μA cm^{-2}. The fuel cell life time-test was performed at constant voltage, 400 mV, shown in Figure 6.11. The current density was ca. 200~250 μA cm^{-2} for the first 100 h, and increased to 340 μA cm^{-2} and remained constant thereafter.

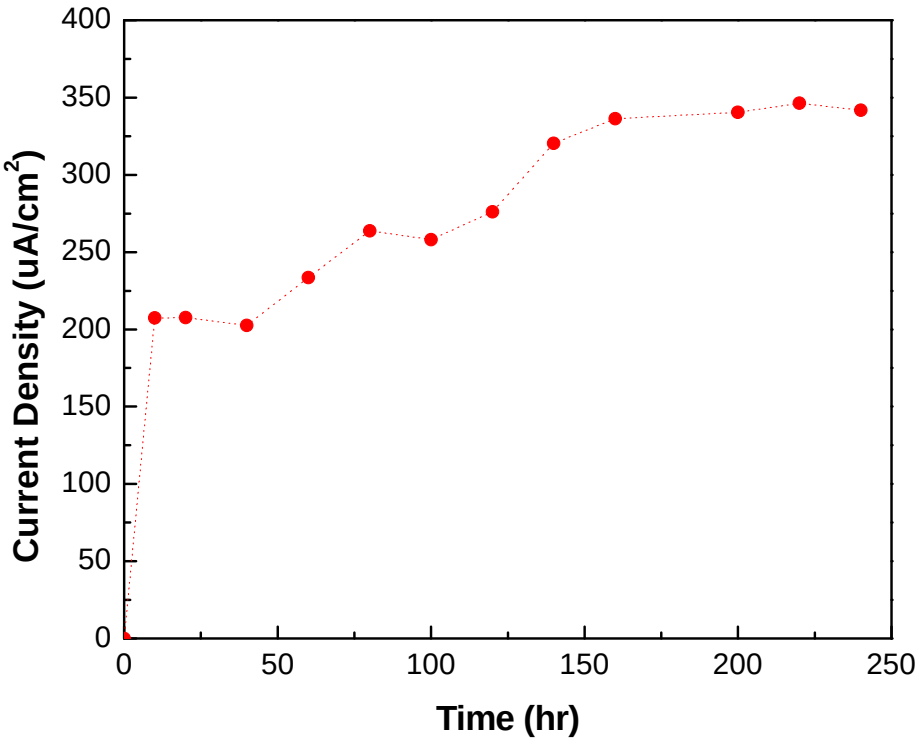

Figure 6.11: Life time test for a fully passive DMFC with a glass membrane and glass electrodes at 0.4 V; 23°C, 0.5M methanol

Finally, the energy conversion efficiency of a DMFC with the glass electrode was calculated. The lowest permeability coefficient of 2.28x 10^{-10} mol cm $cm^{-2}day^{-1}Pa^{-1}$ was

achieved from the 1:7 catalyst glass ratio sample with 60 min deposition time. The permeability coefficient was lowered by 89.5% compared to the bare glass membrane.

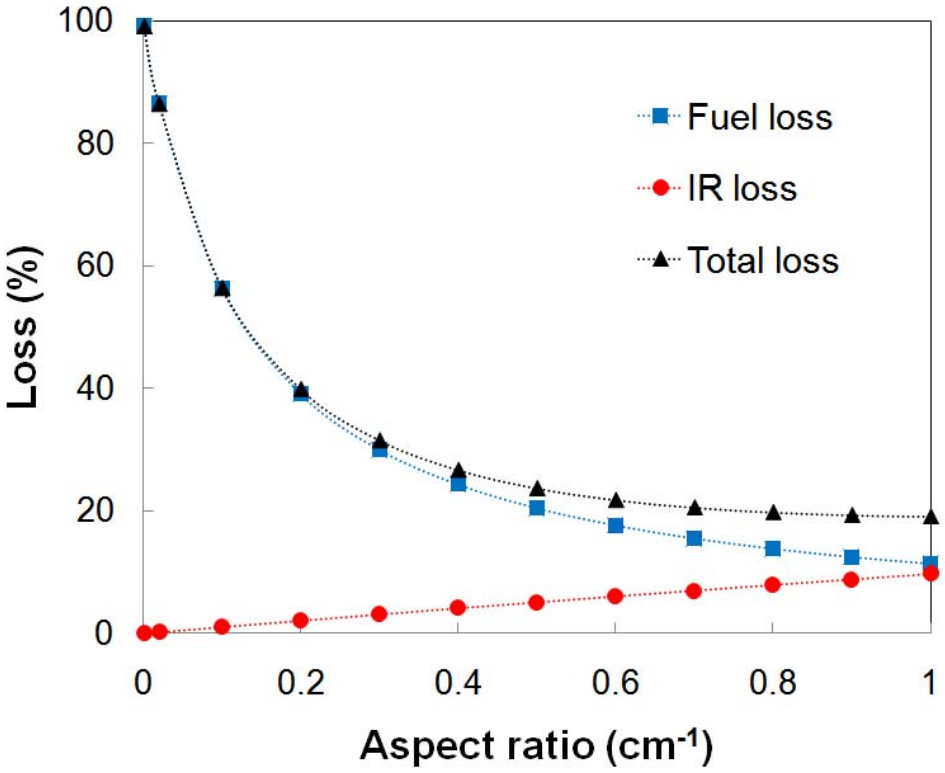

Figure 6.12: Energy losses as a function of alpha for the optimized glass membrane attached with a glass electrode with a selectivity of 7.21, operating at 200 uA and 0.5V

The selectivity was increased from 6.23 to 7.21 by the blocking effect of the glass composite electrode. In a linear scale, it is 537 times higher selectivity. As a result, Figure 6.12 shows the lowest total loss of 19.1 % can be achieved by adjusting the thickness and area of the glass membrane. It is 80.8 % improvement by replacing the polymer materials with inorganic glasses.

6.4 Summary

Inorganic PtRu/C glass composite electrodes have been synthesized via a sol-gel reaction using 3TPS and GPTMS. The gelation time, curing temperature, the mole ratio of the sol components, and the ratio of catalyst to glass in the electrode were optimized. PtRu was electrolessly deposited on top of the glass electrode using the modified Leaman bath. It was found that additional PtRu layer improved the sheet conductivity, catalytic activity on methanol oxidation and the methanol crossover. The inorganic MEA showed stable performance for more than 10 days. The selectivity was increased from 6.23 to 7.21 with the sample which showed the lowest permeability. By the blocking effect of glass composite electrode, the fuel loss further decreased from 57.1 to 19.12%.

CHAPTER 7

ANIONIC-CATIONIC BI-CELL DESIGN FOR DIRECT METHANOL FUEL CELL STACK

7.1 Objective

In order for utilizing the small volume allowed for low power devices, a new fuel cell stack design is proposed using an AEMFC and a PEMFC in series with a single fuel tank servicing both anodes in a passive direct methanol fuel cell configuration. The anionic-cationic bi-cell stack has alkaline and acid fuel cells in series (twice the voltage), one fuel tank, and simplified water management. The series connection between the two cells involves shorting the cathode of the anionic cell to the anode of the acidic cell. The aim of this chapter is to address the concern about the short circuit by investigating the actual electrode potential on each cell. The effect of ionomer content on the AEM electrode potential and the activity of methanol oxidation were investigated. The viable bi-cell stack design is demonstrated. The work presented in this chapter has been previously published in the Journal of Power Sources [45].

7.2 Experimental

The PEM electrode was made with Nafion ionomer (5wt% suspension), 40wt% Pt/C catalyst for cathodes, and 60wt% PtRu/C for anodes. The catalyst ink was prepared by mixing the catalyst, water (75 mg), Nafion ionomer and isopropyl alcohol (1:5 by mass of catalyst and ionomer to isopropyl alcohol). The catalyst ink was sonicated for 30 minutes and then sprayed onto hydrophobic carbon paper (TGPH-090) for the cathode, and hydrophilic carbon paper (2050L) for the anode. The electrodes had a surface area of 2 cm^2 and the metal loading was 4.0 mg cm^{-2}. Nafion 117 was pretreated with 3% H_2O_2, 1 M H_2SO_4, and water at 80 °C, each for one hour. The electrode was pressed onto Nafion 117 at 2 MPa gauge pressure and 135^oC for 3 min.

The AEM electrode was made using an AEM ionomer, poly (arylene ether sulfone) functionalized with quaternary ammonium groups. The synthesis was described previously [71]. The physical properties of the AEM are summarized in Table 7.1. Two different ionomers with different ion exchange capacity (IEC), L-AEM (low IEC AEM) and H-AEM (high IEC AEM), were used in this study. The AEM ionomer was diluted to 5wt% with dimethyl formamide (DMF). The catalyst ink for the AEM electrode was prepared by mixing the catalyst, water, AEM ionomer and a mixture of DMF (400 mg) and methanol (300 mg). The catalyst ink was sonicated for 30 minutes and sprayed onto the carbon paper, as described above for the PEM electrodes. Also, the resulting AEM electrodes had the same surface area and metal loading as the PEM electrodes. Before fabricating a membrane electrode assembly (MEA), the AEM electrodes and membrane were immersed in aqueous 0.1 M KOH to exchange OH^- for Cl^-. The AEM electrodes were then pressed onto the membrane at 0.5 MPa and 50^oF for 20 min. For half-cell MEA

tests, a commercial Tokuyama AMX membrane was used. For performance test, H-AEM membrane was used and the membrane thickness was 140 μm.

Table 7.1: Physical properties of the AEM membranes used in this study

	L-AEM	H-AEM
DC[a]	0.8	1.2
Conductivity (mS/cm)	14.0	23.0
Water-uptake (%)	48.0	78.0
Ion-exchange Capacity (mmol/g)	0.92	1.14

[a]Degree of chloromethylation = number of chloromethyl groups/repeat unit, calculated from ^{1}H NMR
All measurements were made at room temperatures.

The electrochemical experiments were performed with a PARSTAT 2263 (Princeton Applied Research) potentiostat. Linear sweep voltammetry (LSV) was carried out with carbon cloth as a counter electrode and a saturated calomel (SCE) reference electrode (CH Instruments). In order to evaluate the effectiveness of the electrodes on the membranes in a fuel cell, an electrode was fabricated on one side of the membrane and tested as a half-cell in a three electrode configuration. A one sided electrode membrane assembly (half-MEA) was placed between the two glass cells and the electrode was a working electrode [65]. The counter and reference electrode were placed on the opposite side of the working electrode so that the protons produced traveled through the membrane, as they would in an operating fuel cell. The compartment on the membrane side containing the counter and reference electrodes was filled with the 1 M

H_2SO_4 solution for PEM electrode and 1 M NaOH for the AEM electrode. The working electrode side was filled with concentrated methanol for anodes and air (or O_2) for cathodes. The potential was cycled at least 10 times at a scan rate of 10 mVs^{-1} until steady state voltammometric behavior was obtained. Linear polarization was performed at a scan rate of 1 mVs^{-1} and IR compensation was used to correct uncompensated resistance.

PEM and AEM single cells were fabricated for testing the fuel cell performance. The fuel cell hardware was made of graphite with small holes for fuel diffusion. The graphite was used as the current collector. The total exposed area was 0.3 cm^2. The current from the I-V polarization curves was reported without normalizing because of the difference in the electrode area ($2cm^2$) and the fuel exposed area. All MEAs were preconditioned by operating them as a fuel cell at a constant cell voltage of 400 mV for at least 2 hours before performing I-V polarization experiments. The scan rate was 1 mVs^{-1}. All tests were performed at an ambient pressure and temperature.

7.3 Results and Discussion

Recently, the development of anion exchange membranes (AEM) and anionic fuel cells has been reported [71-75]. Although AEM technology is not yet as mature as PEM (high ionic conductivity and stability of AEMs are still under investigation), AEM technology is promising because it could address several drawbacks with PEM fuel cell. The high pH environment in AEMFC provides faster kinetics for both oxygen reduction and methanol oxidation, which allows non-Pt catalysts such as silver and nickel to be

used. The methanol cross-over is expected to be lower due to the opposite direction of electro-osmotic drag.

AEMs can be used to improve the design and performance of the bi-cell stack. The fuel cell reactions for a DMFC with an AEM are shown in Equations 7.1, 7.2 and 7.3.

Anode: $CH_3OH + 6OH^- \rightarrow CO_2 + 5H_2O + 6e^-$ ($E°_a$=-0.81 V vs. NHE at 25°C) (7.1)

Cathode: $3/2\ O_2 + 3H_2O + 6e^- \rightarrow 6OH^-$ ($E°_c$= 0.40V vs. NHE at 25°C) (7.2)

Overall: $CH_3OH + 3/2\ O_2 \rightarrow 2H_2O + CO_2$ (E_{cell} = 1.21V vs. NHE at 25°C) (7.3)

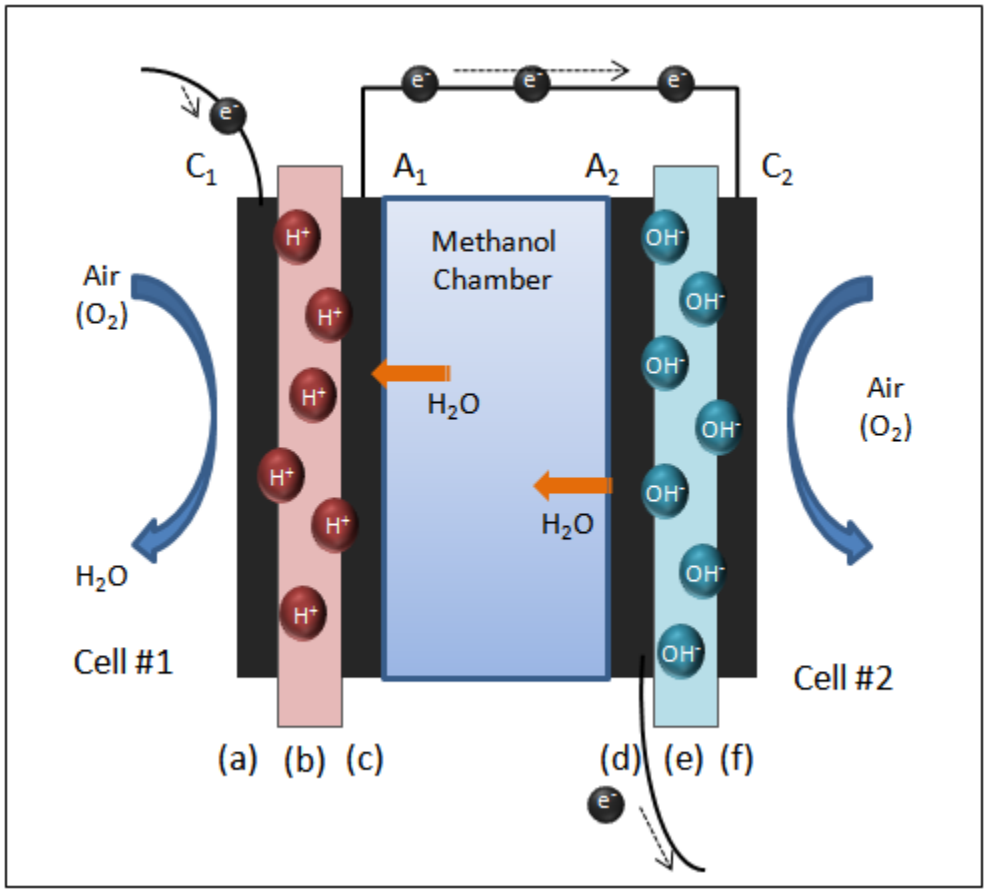

Figure 7.1: A schematic of the AEM-PEM bi-cell stack for passive DMFC (PEM cathode (a), PEM (b), PEM anode (c), AEM anode (d), AEM (e), AEM cathode (f))

In the alkaline fuel cell, the potentials are shifted to more negative values as a result of the high pH. This feature will be exploited in the study to improve the bi-cell design. The potential difference between the anode A_1 and cathode C_2 of the all PEM bi-cell design can be changed by combining an AEM cell with a PEM cell as shown in Figure 7.1. If cell #2 were changed from an acid cell to an alkaline one, then the cathode of cell #2 would be shifted to more negative potentials, as compared to the acid case (compare Equation 2.30 to 7.2). The cathode of cell #2, C_2 is closer in potential to that of the anode of cell #1, A_1.

The electrode potentials of the AEM and PEM anode and cathodes were first investigated to examine the potential shift of the oxidation and reduction reactions with pH. The low pH electrode reactions were evaluated with an electrode fabricated with Nafion ionomer on a Nafion 117 membrane. The ionomer content was 30% of the mass of the carbon in the final dry electrode structure, which was previously optimized [76]. Figure 7.2 shows the anode and cathode polarization curves for the PEM electrodes, as would occur in a PEM fuel cell. The potential of zero current for the reduction of oxygen from air was 0.91 V, and 0.95 V for the reduction of pure oxygen. This is approximately 0.3 V negative of the standard potential for oxygen reduction. The potential of zero current for methanol oxidation at the PEM anode was between 0.22 V to 0.35 V. As the methanol concentration was increased from 0.5 M to 12.0 M, the potential of zero current shifted to more negative values.

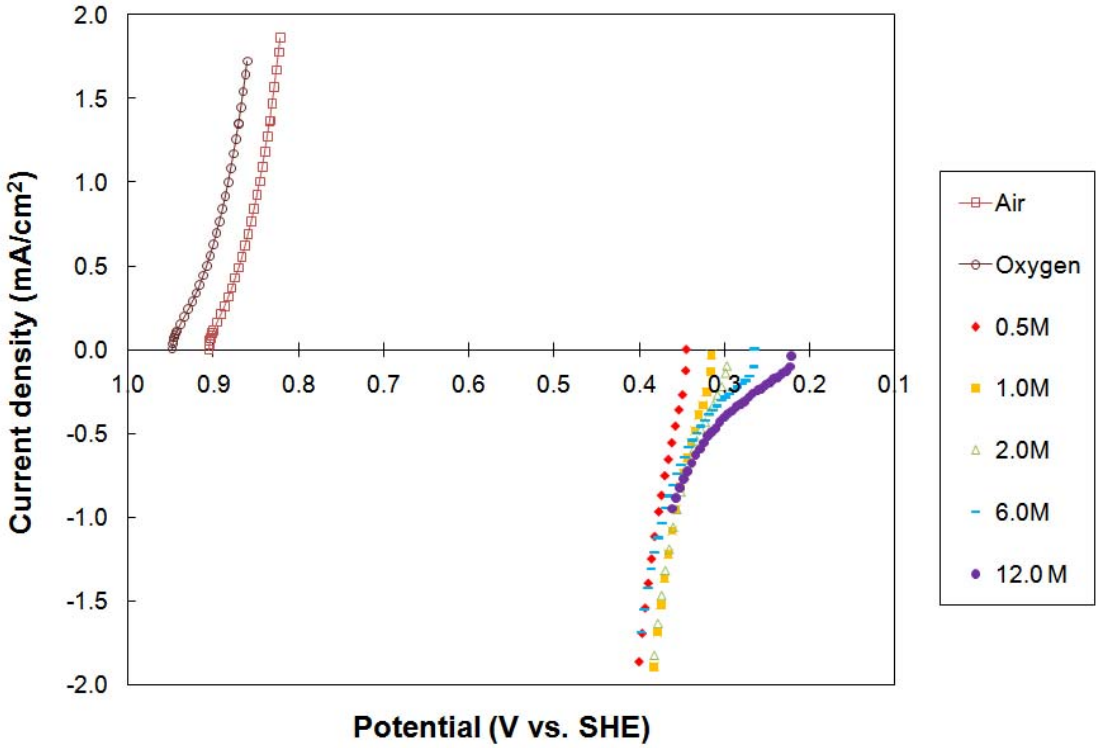

Figure 7.2: Polarization curves of PEM anode with different methanol concentration and PEM cathode with air or oxygen

The anode and cathode polarization curves for the AEM electrodes were investigated in a similar manner as the PEM electrodes. Two half-cell MEAs were fabricated using commercial a Tokuyama AMX membrane and the high IEC ionomer, H-AEM. The ionomer content was 30wt% of the carbon in the final dry electrode structure. Figure 7.3 shows the anode polarization curves under alkaline conditions, as in an AEMFC for methanol concentrations of 1.0 M, 2.0 M and 4.0 M. The onset of the oxidation of methanol occurred at about -0.5 V. This value is 0.8 V negative of the oxidation of methanol under acidic conditions at the PEM anode due to the shift in pH, as shown in Figure 7.2. At higher methanol concentration, the potential of zero current shifted to more negative potentials, just as with the PEM anode. Concentrations higher

than 4.0M could not be used due to the solubility and swelling of the ionomer in the AEM samples. The potential of zero current for the reduction of humidified air and oxygen at the alkaline AEM cathode was 0.30V and 0.31V, respectively. The values are within 0.1 V of the standard potential for oxygen reduction under alkaline conditions, Equation 7.2.

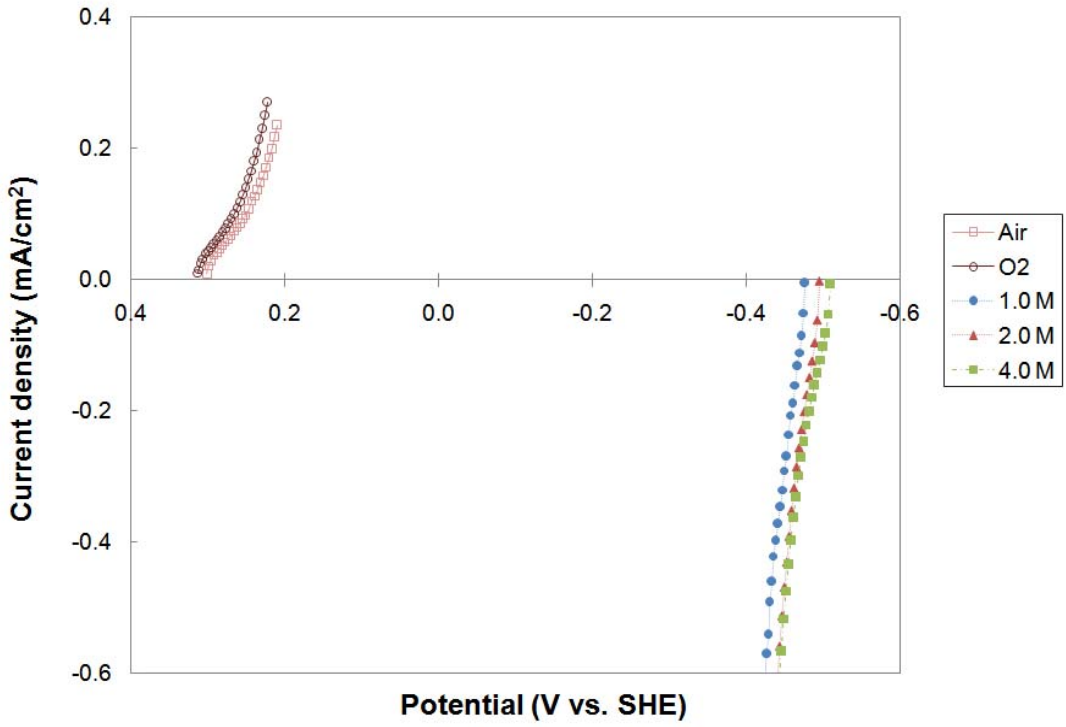

Figure 7.3: Polarization curves of AEM anode with 1.0M, 2.0M and 4.0M methanol and AEM cathode with air or humidified oxygen

Figure 7.4 shows the current-voltage curves for the oxidation of 1M methanol at the AEM and PEM electrodes, and the reduction of air at the AEM and PEM cathodes, plotted in one figure. The reduction of air at the AEM cathode is at essentially the same potential as the oxidation of methanol at the PEM anode. If used in a bi-cell configuration, where the high pH AEM air-cathode is shorted to the acid PEM anode, there is essentially

no potential difference between the two electrodes, which mitigates the short circuit in an all-PEM bi-cell, as discussed in the introduction section.

On the other hand, Figure 7.4 also shows one of the challenges facing high pH AEM based fuel cells. It is known that the kinetics for methanol oxidation and oxygen reduction in alkaline media are faster than in acid media [73, 77]. However, the beneficial

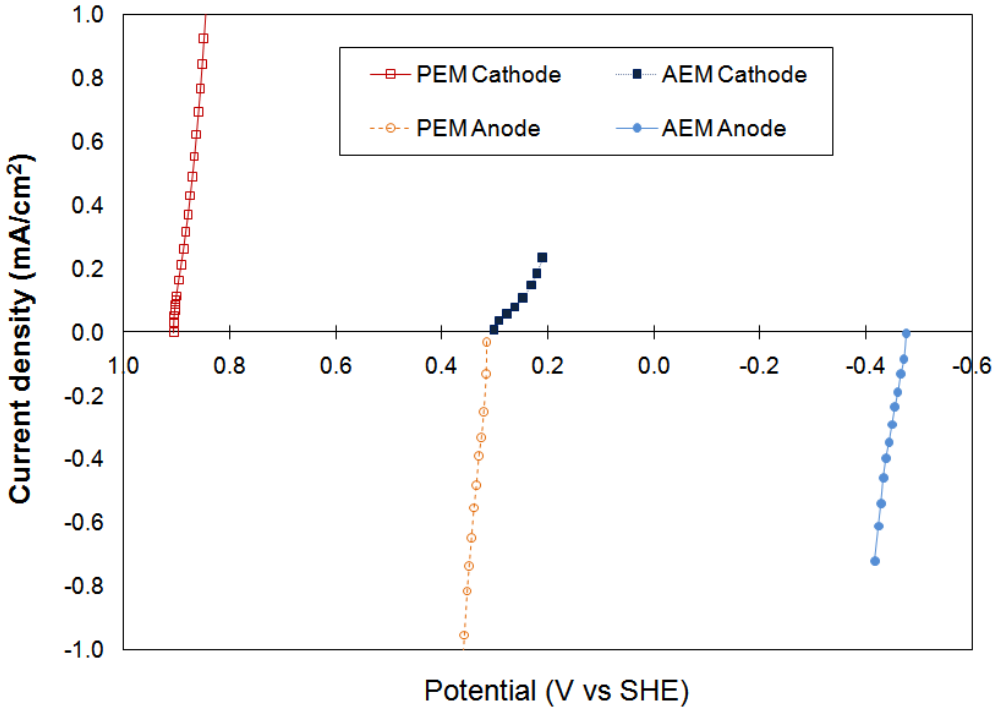

Figure 7.4: Actual electrode polarization curves
(AEM and PEM anode with 1.0 M methanol and AEM and PEM cathode with air)

effects of alkaline media is not reflected in the current density for oxidation and reduction in alkaline media, compared to acid media in Figure 7.4 due to the immature electrode fabrication technology for AEM electrodes. Advances in AEM electrode assemblies will

improve the AEM fuel cell performance by decreasing the overpotential.

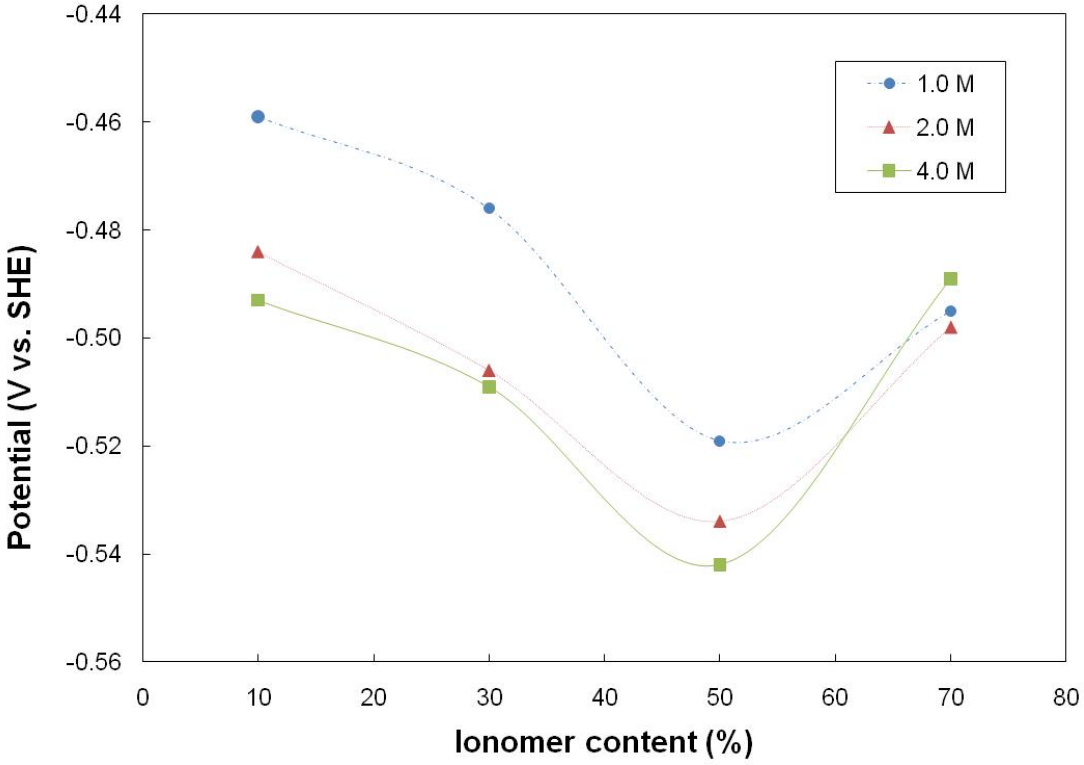

Figure 7.5: AEM anode OCV depending on ionomer content and methanol concentration

The effect of the ionomer content on the electrode potential of AEM anode was investigated. Figure 7.5 shows that increasing the ionomer content from 10% to 50% shifted the potential of zero current to more negative values. The total hydroxide content and ionic pathway was increased with higher ionomer content inside of the electrode. However, when the ionomer content reached 70%, the potential of zero current shifted to more positive potentials. The methanol oxidation reaction occurs in the active surface area at the three-phase boundary of catalyst, reactant, and ionomer. With excess ionomer in the electrode, the reactants are obstructed from reaching the catalyst surface. Additionally in Figure 7.5, there was a negative shift in the oxidation potential with

higher methanol concentration.

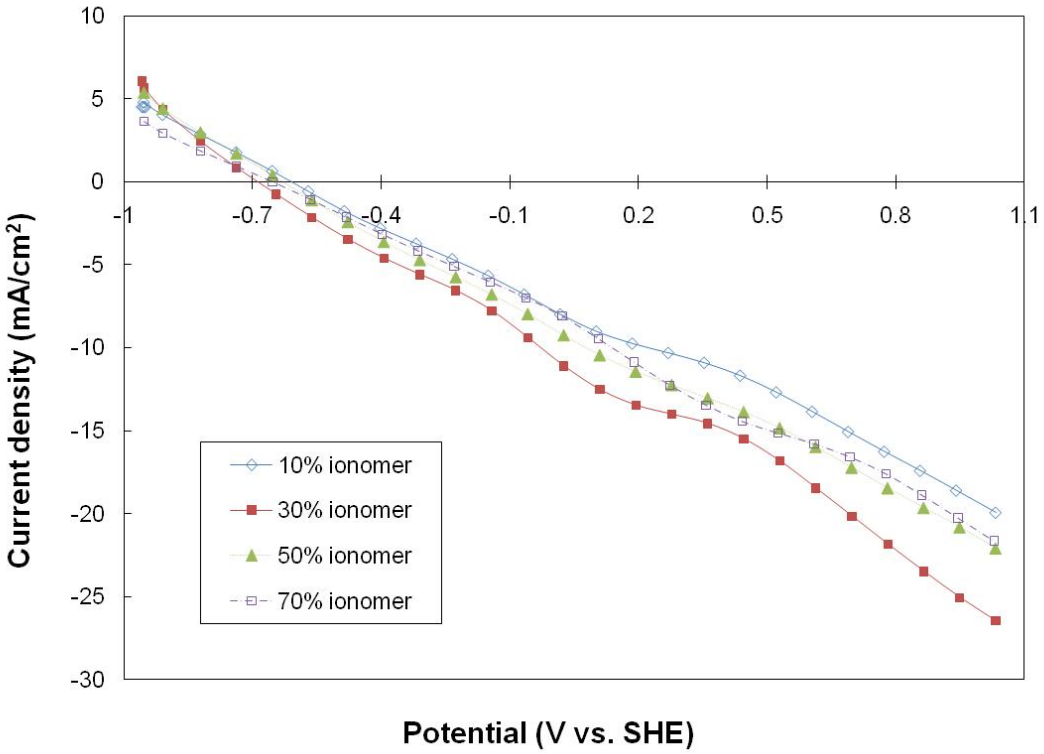

Figure 7.6: Linear polarizations for methanol oxidation depending on ionomer content of H-AEM

The effect of ionomer content on the catalyst activity for methanol oxidation was also investigated. Figure 7.6 shows the linear polarizations for methanol oxidation at the high pH AEM electrode as a function of the ionomer content. In this experiment, the same ionomer, H-AEM, was used to find the optimum content. An ionomer content of 30% was shown to yield the highest peak current for methanol oxidation at 0.15 V vs. SHE, which is near the operating point of an alkaline AEM fuel cell. The poor performance of the 10% ionomer content is likely due to the lack of an adequate three-phase boundary. The poor performance at 50% and 70% ionomer was likely due to mass transfer limitations resulting in low catalyst activity [44, 67, 78-79].

Based on the optimized ionomer results shown above, an ionomer content of 30% was chosen for use in the electrodes for the alkaline, AEM fuel cell in the AEM-PEM bi-cell configuration. Figure 7.7 shows the AEM fuel cell performance with the optimized ionomer content. The first AEM fuel cell was fabricated with H-AEM ionomer as the membrane and as the ionomer in the electrode assembly. A passive fuel cell configuration (i.e. stagnant tank of 2.0 M methanol) was as the fuel at the AEM anode. The AEM cathode was open to the ambient air at room temperature and ca. 40% relative humidity. The open circuit voltage of the cell was 0.57 V, and a current of 1.4 mA was measured at a cell voltage of 0.4 V. In order to compare cell performance for electrodes with different ionomer content, a second AEM fuel cell was prepared with the lower IEC ionomer, L-AEM. The membrane electrode assembly had the same membrane as the first fuel cell, H-AEM. It was found that the L-AEM ionomer led to higher fuel cell performance, Figure 7.7. The open circuit voltage was 0.64 V and the current was 3.28 mA at 0.4 V. This is twice the current achieved with the H-AEM ionomer. Since H-AEM has a higher ionic conductivity and IEC, as shown in Table 7.1, it is clear that the microstructure and water swelling in the electrode assembly are critical factors, rather than simply ionic conductivity. The L-AEM ionomer has less water swelling due to its lower quaternary ammonium density than the H-AEM ionomer, which is the most likely cause of the performance difference between the two ionomores. It is common for membranes with a high degree of chloromethylation, and resulting quaternary ammonium content, to have higher conductivity and IEC, but also higher water uptake [71]. High water uptake can result in flooding in the electrode which can impede the mass transfer of reactants inside the catalyst layer.

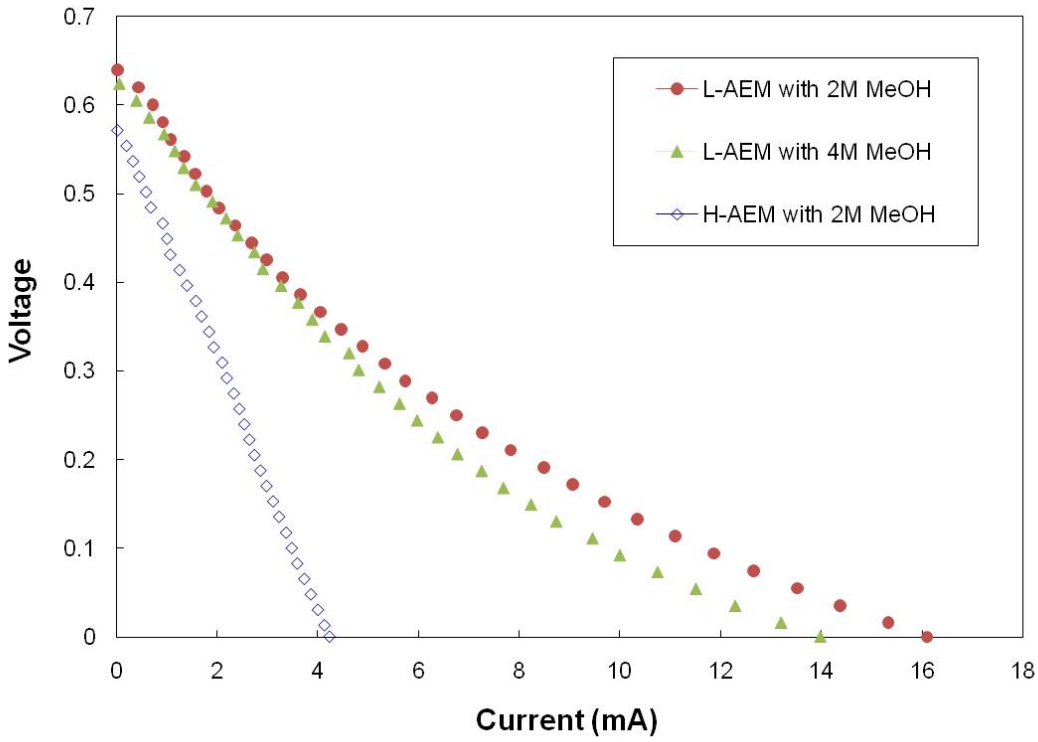

Figure 7.7: AEMFC performance with H-AEM membrane and different IEC ionomers, L-AEM and H-AEM, at room temperature

The AEM fuel cell was also tested in 4.0 M methanol with the L-AEM electrode assembly, as shown in Figure 7.7. Since there is no pressure difference across the membrane in a passive system (the fuel is not pumped to the anode), a higher methanol concentration can lead to higher performance, unless other factors, such as cross-over, become a factor [80]. In this case, the performance of the L-AEM ionomer with 4.0 M methanol fuel was slightly worse (open circuit voltage of 0.67 V) than the 2.0 M

methanol case.

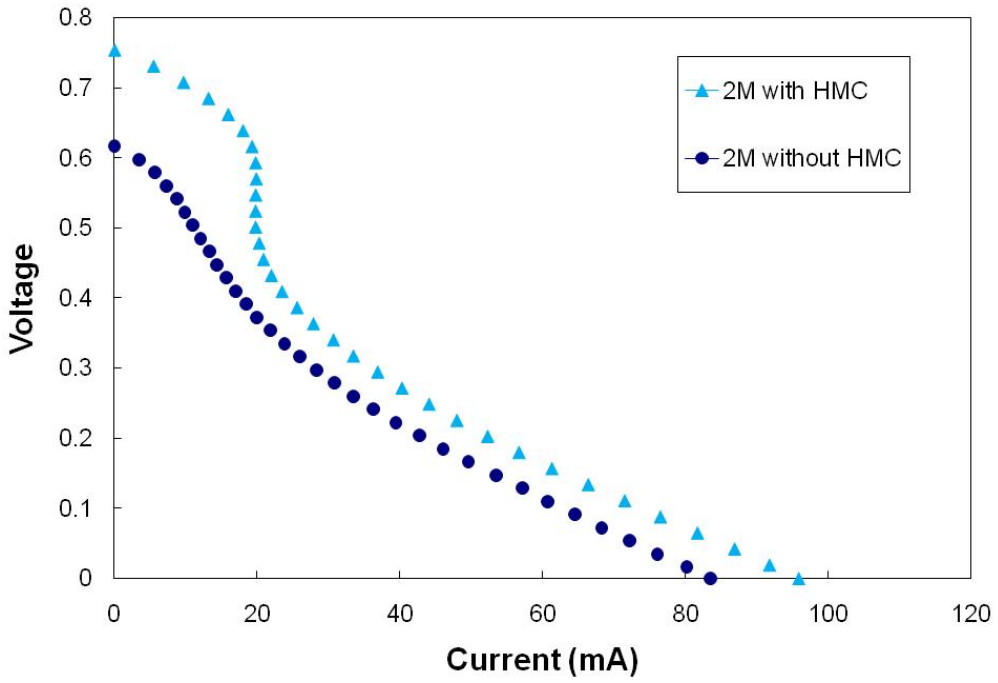

Figure 7.8: The effect of HMC on PEMFC performance prepared using Nafion 117 membrane and Nafion ionomer

Maintaining electrode-fuel contact is critical in liquid feed fuel cells, especially for portable devices which can be moved and rotated. Thus, it is desirable to use a wicking mechanism to keep the electrode assembly wet with fuel even when the device is inverted. This concern is especially true in the bi-cell configuration, as shown in Figure 7.1, where the two electrodes are mounted opposing each other. In the AEM-PEM bi-cell configurations assembled here, hydroxy-methoxy cellulose (HMC) was used in the fuel tank as a liquid wicking material. The single fuel cell performance with HMC was tested at different orientations: anode-side up, upside down and a 90 degree angle. Steady state

performance was achieved at all three orientations, however, it is of interest to evaluate the performance under wicking conditions vs. no wicking conditions. Thus, the single fuel cell performance in 2M methanol was tested with or without HMC. It was found that the AEM fuel cell performance was same in all cases. Interestingly, the PEM fuel cell performance changed when HMC was used, as shown in Figure 7.8. The open circuit voltage of the PEM fuel cell was 0.1 V higher with HMC. The most likely cause of the improved performance was a decrease in cross-over with HMC due to the flow restrictions HMC causes [1]. The methanol cross-over in an AEM cell is lower than in a PEM cell because electro-osmotic is in the opposite direction. If a higher concentration of methanol (>2M) was used, the effect of fuel restriction by the HMC on the AEM cell is expected to be the same as the PEM case.

Finally, the AEM-PEM bi-cell was constructed. An o-ring style glass joint was used to construct the fuel reservoir between the AEM and PEM fuel cells. The AEM and PEM fuel cells were 5 cm apart and the two anodes shared the common methanol fuel tank which included the HMC. Each cathode was open to the air on the outside of the assembly. The cells were operated at room temperature and humidity (ca. 40% relative humidity). The AEM cathode was shorted to the PEM anode. It was confirmed that there was no current flow between the AEM cathode and PEM anode. In a separate experiment, two PEM cells were used in the same bi-cell configuration. A small current of 4 μA was observed between the anode #1 and cathode #2 (the electrode size was 2 cm^2), which indeed showed the expected short circuit current discussed in the Introduction section.

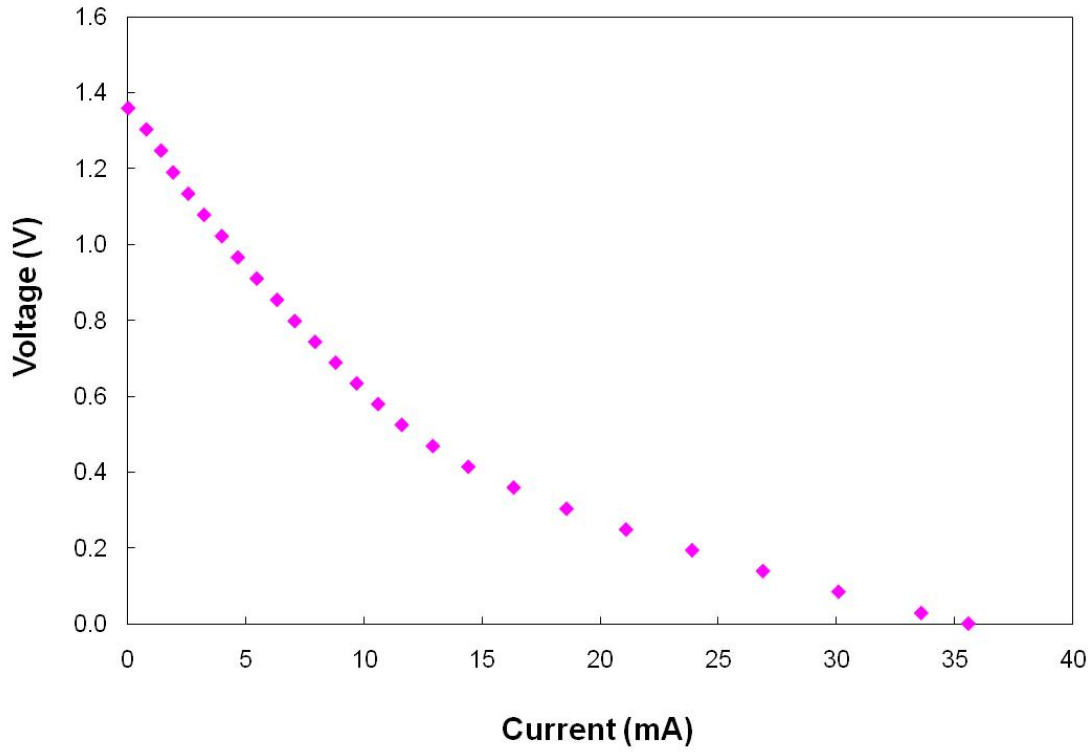

Figure 7.9: The bi-cell performance with 2M methanol and air at room temperature

Figure 7.9 shows the performance of the AEM-PEM bi-cell, which is composed of the PEM cell from Figure 7.8 and AEM cell from Figure 7.7 (using L-AEM ionomer in the electrodes). The open circuit voltage of the bi-cell at ambient temperature and relative humidity was 1.36 V, which corresponds to the sum of the open circuit voltages of the AEM and PEM cells. The current was 7.1 mA at 0.8 V. The moderate performance of the current bi-cell system is limited by the performance of the less mature AEMFC. The bi-cell performance will be increased as the AEM cell technology improves and better matches that of the PEM technology, including the membrane development with high conductivity and stability. The performance here does serve as a demonstration of the advantages of the mixed acid-alkaline bi-cell construction.

In addition to the common-voltage AEM cathode/PEM anode configuration, there are several other intriguing aspects of the bi-cell design in the area of water management. As shown in Equation 2.30 and 7.2, water is produced at the PEM cathode and AEM anode, respectively. This complementary water generation and consumption feature of the AEM and PEM technology can be used to provide self humidification and water management. That is, an air stream flowing across alternating AEM and PEM cathodes will be alternately humidified and dehumidified. Likewise, the methanol fuel will be become diluted by water entry from the AEM cell and depleted of water by the PEM cell. A detailed analysis of electo-osmotic drag and other factors is now underway to better understand these features.

7.4. Summary

A bi-cell design with an AEM and PEM fuel cell in series using a common liquid fuel tank was successfully demonstrated. The actual electrode potentials for both acid-PEM and alkaline-AEM were evaluated and shown to match the combined cell. The actual AEM cathode potential was essentially the same as the PEM anode potential making the bi-cell configuration viable. High ionomer content was shown to cause a negative shift in anode potential of zero current. A 30% loading of the H-AEM ionomer was found to be the optimum content for the current AEM fuel cell. The performance of AEM fuel cell prepared with the L-AEM ionomer showed higher performance than that of the H-AEM ionomer due to lower water uptake. Fuel wicking with HMC was shown to help achieve orientation-independent performance. The bi-cell system was demonstrated with the optimized AEM and PEM fuel cell in series operated from a single

fuel tank. The open circuit voltage of the bi-cell from one fuel tank was 1.36 V, which corresponds to the sum of the open circuit voltages of the AEM and PEM cells.

CHAPTER 8

THE EFFECT OF HYDROPHOBICITY IN ALKALINE ELECTRODES FOR PASSIVE DMFC

8.1 Objective

The anionic-cationic bi-cell performance can be increased by improving the performance of AEM cells. The high overpotential in AEM electrodes is one of the reasons for the limited performance of the current AEM cells. In an effort to improve the electrode overpotential in an alkaline environment, the effect of hydrophobicity in the electrode is addressed in this chapter. Two approaches have been used to increase the hydrophobicity within the electrodes. One is using a more hydrophobic ionomer, and the other is introducing polytetrafluoroethylene (PTFE) into the catalyst layer. Two types of anion exchange ionomers with different hydrophobicity have been synthesized for this study. The effect of ion exchange capacity, ionic conductivity, and water uptake of the ionomers on the electrode performance has been studied using a half-cell test. However, other properties of ionomers can also have an influence the electrode performance, such as the porosity and the degree of interaction with the catalysts. Also, the addition of PTFE to further increase the hydrophobicity was examined in terms of the fuel cell performance.

8.2 Experimental

Two different anion exchange ionomers were used in this study, as shown in Figure 8.1. Ionomer I is poly(arylene ether sulfone) containing trifluoromethyl groups, functionalized with quaternary ammonium ions, and Ionomer II is a partially fluorinated copoly(arylene ether). The synthesis of Ionomer I and Ionomer II was described previously [81]. The ionomer was stored and used in the chloride form as a 5wt% solution in dimethyl formamide (DMF).

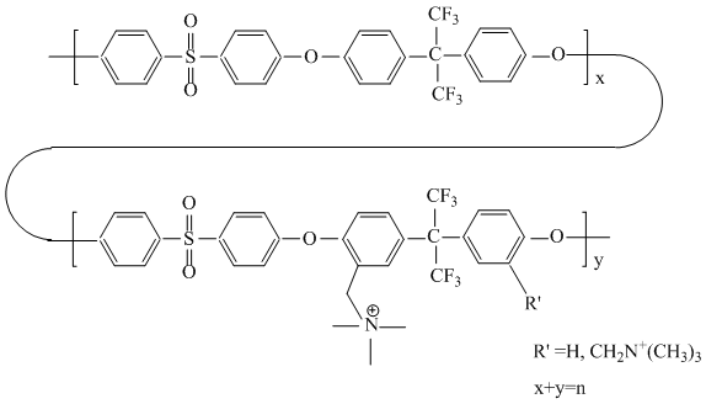

(a) Ionomer I

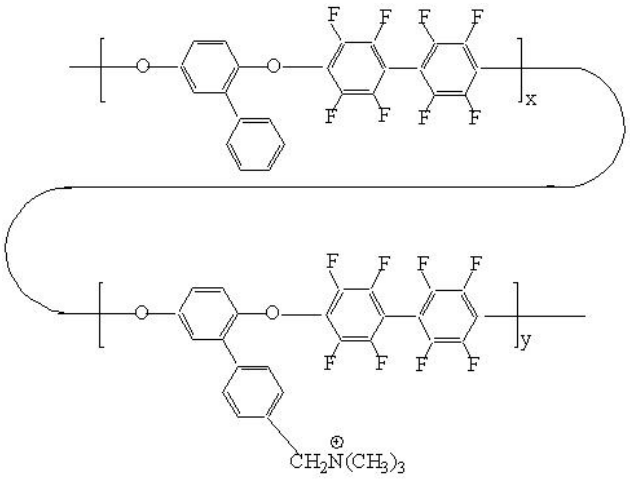

(b) Ionomer II

Figure 8.1: Chemical structure of (a) Ionomer I and (b) Ionomer II

The water uptake of the AEMs was evaluated by comparing the weight of the dry and wet membrane. The weight of the wet membrane was measured after it had been soaked in water for 24 hours at room temperature. Then, the membrane was placed in a dessicator for 24 hours to obtain the weight of the dry membrane. The IEC of the AEM was determined by back-titration [82]. The conductivity of the AEM was evaluated by a four-electrode measurement using a BekkTech Conductivity Cell with AC impedance. The frequency of the impedance measurements ranged from 500 mHz to 0.5 MHz with an AC signal amplitude of 20 mV. At least 30 min equilibrium time was used before acquiring data and the final values were confirmed by performing multiple runs to ensure that equilibrium had been reached.

All electrodes were tested as half-cells with an electrode attached to the membrane. The AEM electrode was made with 40wt% Pt/C catalyst for the cathodes, and 60wt% PtRu/C for the anodes using an AEM ionomer. The catalyst ink for the AEM electrode was prepared by mixing the catalyst, water, AEM ionomer and a mixture of DMF and methanol. The ratio between DMF and methanol was 3:2. The ionomer content was varied from 2 wt% to 30wt% of the carbon in the final dry electrode structure. The catalyst ink was sonicated for 30 minutes and then sprayed onto hydrophobic carbon paper (TGPH-090) for the cathode, and hydrophilic carbon paper (2050L) for the anode. The electrodes had a surface area of 2 cm^2 and the metal loading was 4.0 mg cm^{-2}. The AEM electrode was then pressed onto the membrane at 1.2 MPa and 50^oC for 10 min. The membrane used for the half-cell test was Fumasep® FAA-PK purchased from Fumatech. After fabricating a membrane electrode assembly (MEA), the MEA was immersed in aqueous 0.1 M KOH to exchange OH^- for the Cl^-.

The cathode PEM electrode was made from Nafion ionomer (5wt% suspension) and 40wt% Pt/C. The catalyst ink was prepared by mixing the catalyst, water, Nafion ionomer and isopropyl alcohol (1:5 by mass of catalyst and ionomer to isopropyl alcohol). The catalyst ink was sonicated for 30 minutes and sprayed onto hydrophobic carbon paper (TGPH-090). The resulting PEM electrode had the same surface area and metal loading as the AEM electrodes. Nafion 117 was pretreated with 3% H_2O_2, 1 M H_2SO_4, and water at 80°C, each for one hour. The electrode was pressed onto Nafion 117 at 2 MPa at 135^{o}C for 5 min.

The half-cell performance was evaluated in a three-electrode configuration using a two-compartment cell. An MEA with an electrode only on one side (half-cell MEA) was placed between the two glass cells and the electrode was used as the working electrode [65]. A graphite plate with holes for fuel diffusion was used as a current collector. The working electrode side was filled with 1M methanol for the anode and air for the cathode. The counter and reference electrodes were placed in the opposite compartment of the two-compartment cell. The opposite compartment was filled with 0.5 M NaOH for the AEM electrode and 0.5 M H_2SO_4 solution for the PEM electrode. The electrochemical experiments were performed with a PARSTAT 2263 (Princeton Applied Research) potentiostat. Linear sweep voltammetry (LSV) was carried out with a carbon cloth as the counter electrode and a saturated calomel (SCE) reference electrode. The potential was cycled at least 10 times at a scan rate of 50 mVs^{-1} until steady state behavior was obtained. Linear polarization was performed at a scan rate of 1 mVs^{-1} and IR compensation was used to correct for the uncompensated resistance.

AEM single cells were fabricated for testing the fuel cell performance. The alkaline MEA was comprised of a Tokuyama A201 membrane and the optimized electrodes. The membrane and electrodes were pressed together at 2 MPa and 135^{o}C for 20 min. A passive fuel cell configuration (i.e. stagnant tank of 1.0 M methanol) was used as the fuel for the AEM anode. The AEM cathode was open to ambient air at room temperature. The fuel cell hardware was made of graphite with holes for fuel diffusion. The graphite was also used as the current collector. I-V polarization curves were obtained at a scan rate of 10 mV s^{-1}.

8.3 Results and Discussion

To investigate the effect of hydrophobicity in the alkaline electrodes, two different ionomers were prepared. The chemical structures of Ionomer I and Ionomer II are shown in Figure 8.1, and the physical properties are summarized in Table 8.1. They have the same quaternary ammonium functional group, but different backbone structures. Ionomer I has a polysulfone backbone containing trifluoromethyl groups and Ionomer II has tetrafluoryl phenyl groups in the backbone. In order to fairly compare the two ionomers, samples with similar IEC values were synthesized, 1.14 for Ionomer I and 1.20 mmol g^{-1} for Ionomer II. Even though the IEC of Ionomer I is slightly lower than Ionomer II, Ionomer I has higher conductivity (23 mS cm^{-1}) and water uptake (78 %). This difference is attributed to the hydrophobic nature of Ionomer II due to the fluorination of the polymer backbone. The hydrophobicity leads to lower water uptake. The lower water uptake also results in less ionic conductivity because the ionic conductivity is generally a function of water content.

Table 8.1: Physical properties of Ionomer I and II

	Ionomer I	Ionomer II
Ion-exchange Capacity (mmol/g)	1.14	1.22
Conductivity (mS/cm)	23*	19
Water-uptake (%)	78	55

All measurements were made at room temperature.
**The value was obtained from the previous publication* [45]

The comparison of Ionomer I and Ionomer II on cathode performance was first examined on half-cell MEAs assembled on commercial Fumatech membranes. The counter and reference electrodes were placed in the compartment opposite of the working electrode, so that the anions produced traveled through the membrane, as they would in an operating fuel cell. Thus, the result reflects a closer simulation to the actual fuel cell performance than the traditional method of placing all three electrodes in one compartment [65].

Figure 8.2 shows a comparison of the cathode polarization of the electrodes. The ionomer content was 5wt% of the carbon in the final dry electrode structure, and the catalyst loading was 4 mg cm^{-2}. Ionomer II showed better performance than Ionomer I, although Ionomer II has slightly lower ionic conductivity than Ionomer I. The superior performance of Ionomer II on the cathode is attributed to its hydrophobic nature. Typically, a good cathode electrode should possess facile gas transport properties which can be choked by high water content in the electrode layer. Excessive swelling can inhibit oxygen transport. Similarly, the loss of performance due to high water content in the electrode layer due to ionomer swelling was demonstrated with a H_2/O_2 fuel cell using a

similar alkaline ionomer [83-84]. Typically, high water uptake leads to mechanical failure due to excessive swelling. It is possible that a high degree of swelling in Ionomer I results in poor interfacial contact with the membrane causing low catalyst utilization.

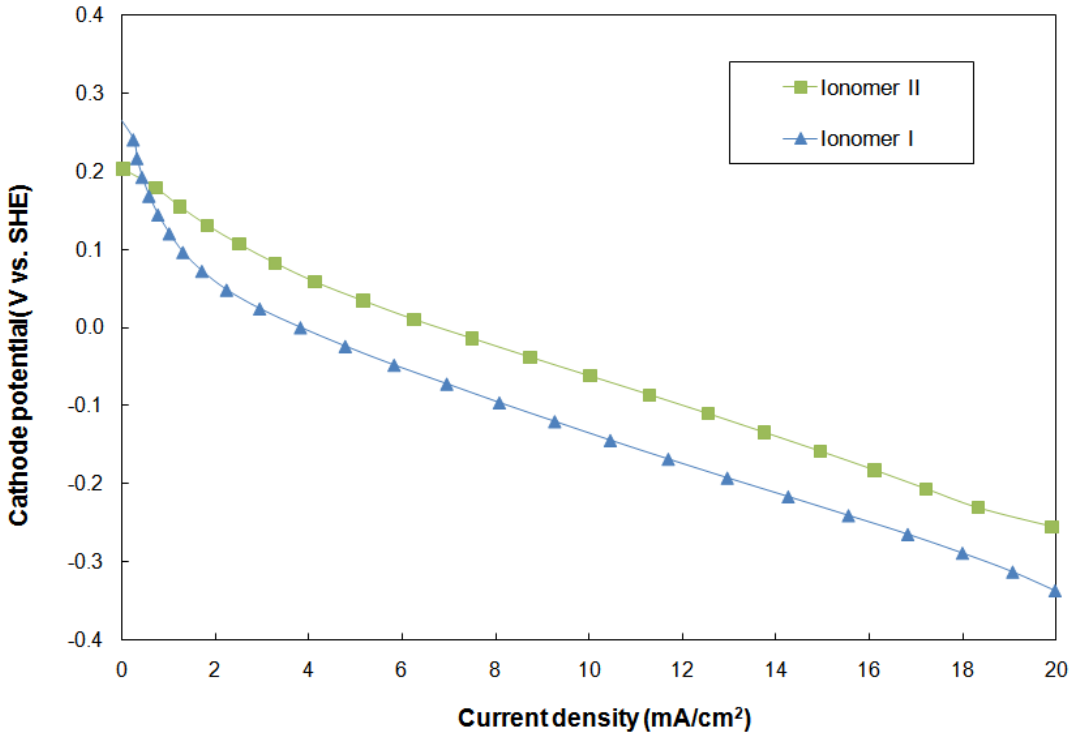

Figure 8.2: Cathode polarization curves comparing Ionomer I and II with air at 25°C (iR corrected)

Ionomer II with three different IECs values were synthesized to evaluate its performance in the cathode. The water uptake and ionic conductivity of the ionomer depending on IEC are shown in Table 8.2. As the IEC increased from 0.63 to 1.22 mmol g^{-1}, the water uptake increased from 14 to 55%. At the same time, the conductivity increased from 5 to 19 mS cm^{-1}.

Table 8.2: Physical properties of Ionomer II as a function of IEC

	IEC=0.63	IEC=0.80	IEC=1.22
Ion-exchange Capacity (mmol/g)	0.63	0.80	1.22
Conductivity (mS/cm)	5	15	19
Water-uptake (%)	14	37	55

All measurements were made at room temperature.

The cathode polarization curves as a function of IEC are shown in Figure 8.3. This shows that higher IEC resulted in improved cathode performance. This is probably due to the improved ionic conductivity with high IEC. However, this is a contrary to the result from our previous study using Ionomer I [45]. Higher IEC of Ionomer I resulted in lower performance even though there was higher ionic conductivity. The decrease in performance with high IEC for Ionomer I was due to excessive water uptake and swelling cause problems with oxygen transport. A hydrophobic ionomer like Ionomer II is favored so as to take advantage of the high ionic conductivity without decreasing reactant transport. Since most high IEC ionomers also have high water uptake, the trade-off between conductivity and water uptake needs to be considered when designing the ionomer structure.

Ionomer content is one of the most important factors affecting the electrode performance [44, 76]. Higher ionomer content could provide increased ionic pathways and improve catalyst utilization, but if the structure is too dense, the reactants can be obstructed from reaching the catalyst surface. Hence, the ionomer content in the catalyst layer must be optimized to provide good ionic and electric conductivity, and high gas and liquid phase transport of the reactants.

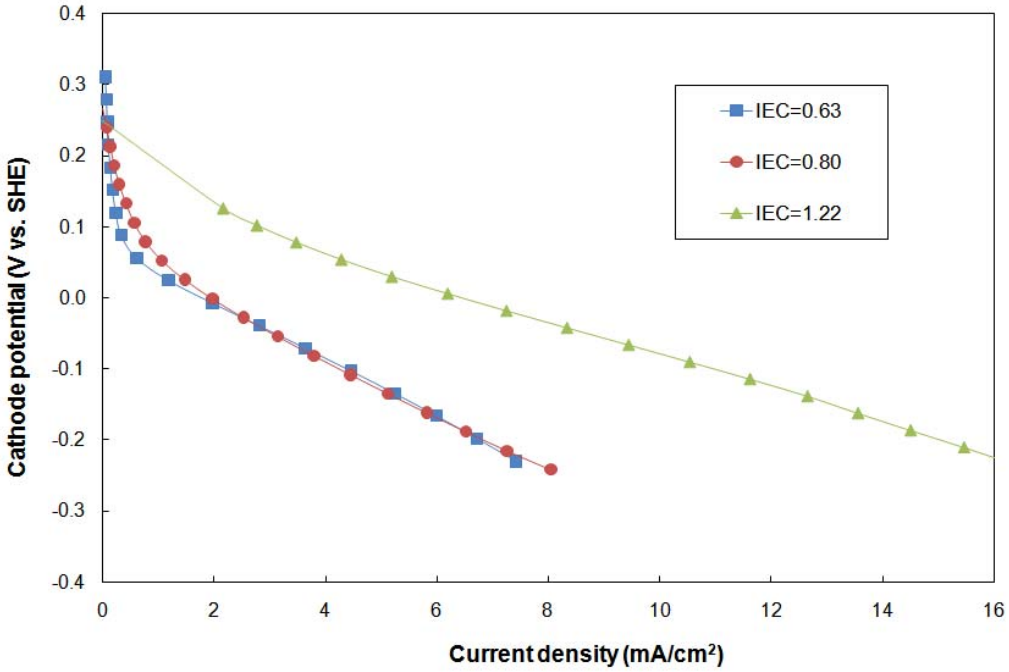

Figure 8.3: Cathode polarization curves of the electrodes as a function of IEC using Ionomer II with air at 25°C (iR corrected)

Figure 8.4 shows that 5wt% is the optimum quantity for Ionomer II. However, 5wt% ionomer in the catalyst layer is a relatively low quantity compared to the optimum value for Nafion, which is about 30wt%. This can be explained in two ways. The first is the nature of the film-like structure in the anion-conducting ionomer in the catalyst layer [47]. Like the A3 ionomer (developed by Tokuyama), Ionomer II forms a very dense catalyst layer, which can block the diffusion of reactants. The second reason is the relatively high water uptake for Ionomer II (55%) compared to Nafion (~30%). Even with the hydrophobic backbone of Ionomer II, the water uptake was still higher than Nafion.

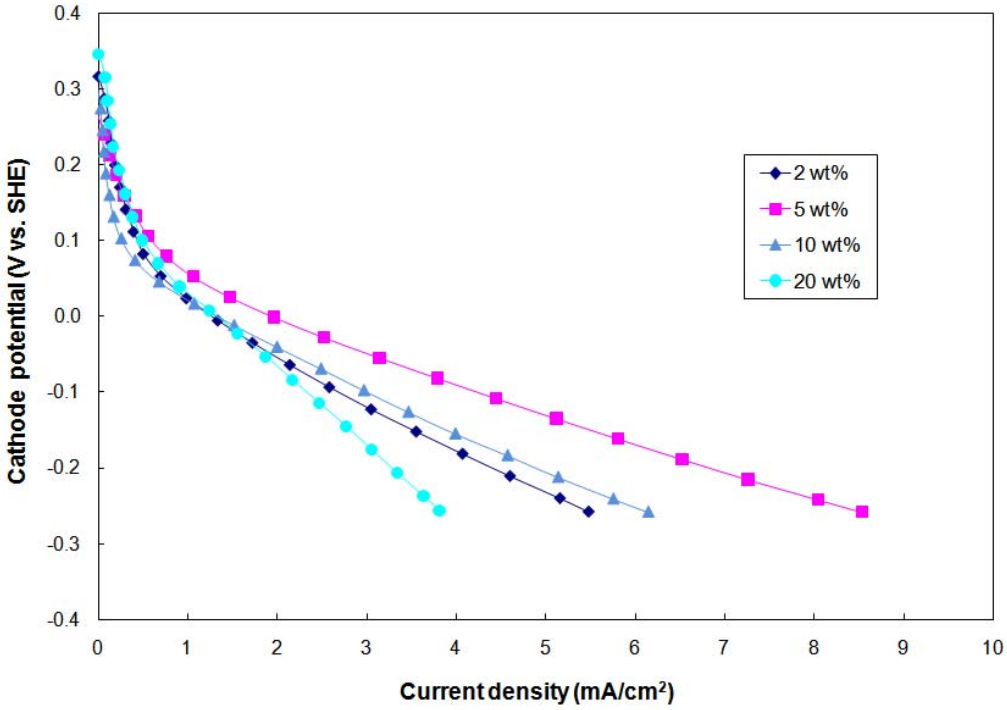

Figure 8.4: Cathode polarization curves of the electrodes as a function of ionomer content using Ionomer II with air at 25°C (iR corrected)

PTFE was added to the electrode structure to further decrease the water uptake in the alkaline electrode containing Ionomer II. The desired amount of PTFE (5 wt% suspension in water) was mixed with the catalyst slurry, and the slurry was coated in the same manner as above. Figure 8.5 shows that the cathode performance increased due to the addition of 10 to 17% of PTFE in the catalyst layer. Although excess amounts of PTFE showed lower performance, the overpotential was improved compared to the non-PTFE electrode. This improvement can be attributed to the enhanced hydrophobicity in the electrode layer. The addition of PTFE reduces the water uptake and provides facile gas transport pathways in the catalyst layer because more catalyst sites become available for oxygen reduction. Additionally, the proper amount of PTFE introduces some porosity

to electrode structure [47, 85]. PTFE not only increases the hydrophobicity in the electrode, but also improves the catalyst utilization and mass transfer of reactants.

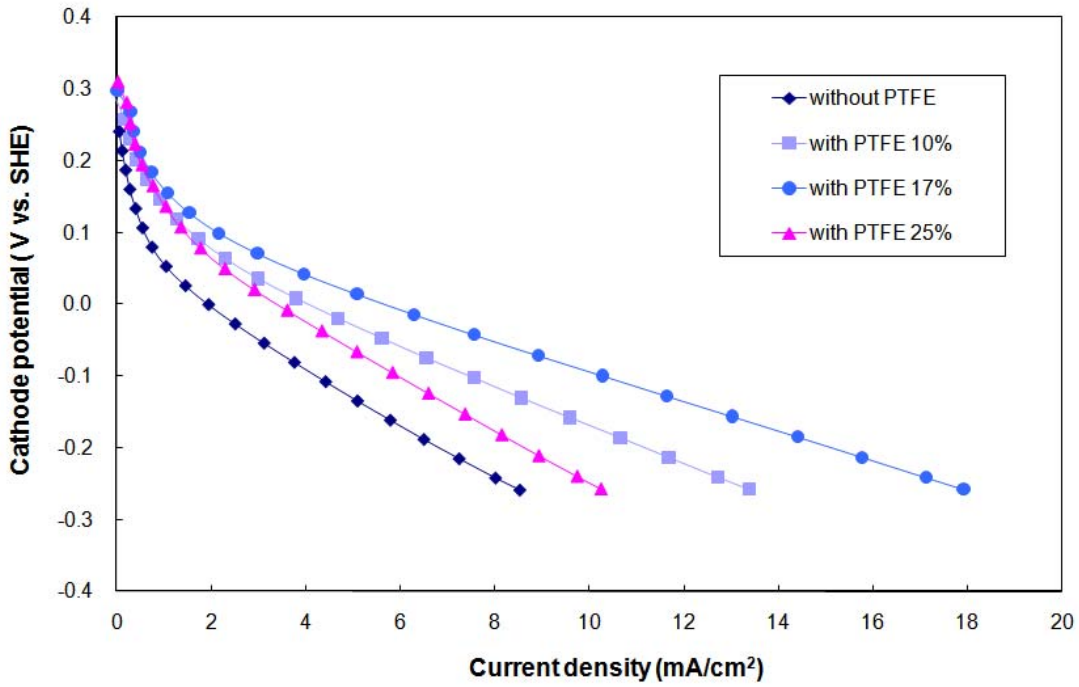

Figure 8.5: The effect of PTFE content on cathode overpotential with air at 25°C (iR corrected) using Ionomer II

The improved cathode performance of Ionomer II, including 17% PTFE, is shown with the optimized Nafion cathode performance in Figure 8.6. The Nafion cathode potential was shifted by 0.7 V vs. SHE to match the open circuit potential with alkaline electrodes for easy comparison. The ionomer II cathode has a lower activation overpotential than Nafion. This could be due to the fast ORR kinetics in the alkaline environment. However, the Ionomer II electrode showed a higher overpotential at high current region than Nafion. The ionic conductivity of Ionomer II is lower than Nafion and the film-like structure of Ionomer II electrode is likely to have poor gas diffusion

compared to the Nafion electrode. This result indicates that the catalyst utilization of the alkaline electrodes needs to be further improved to compete with Nafion electrodes.

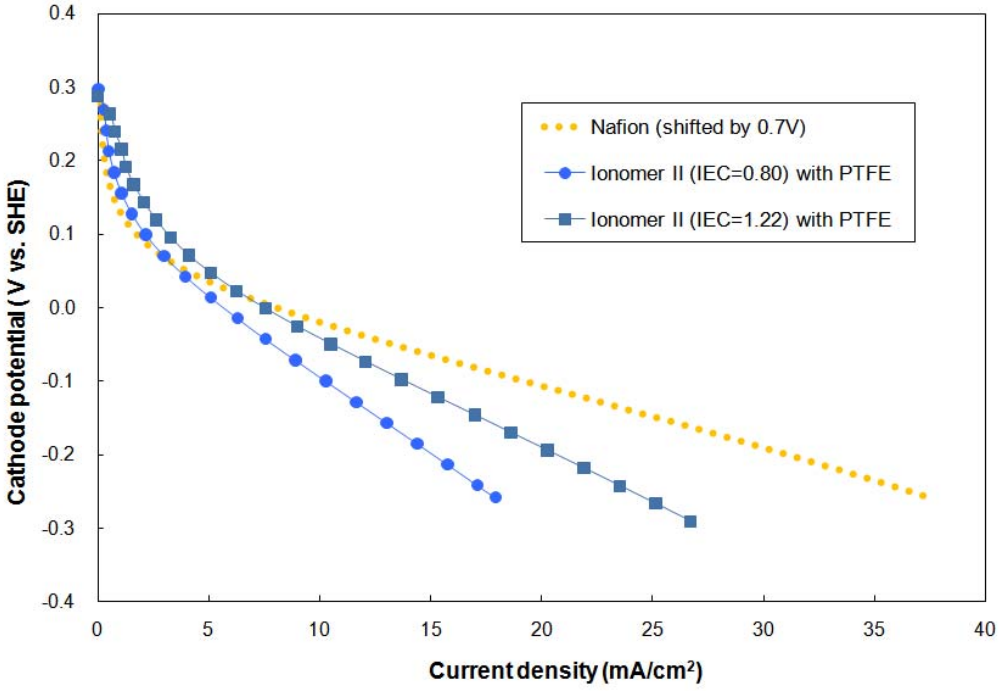

Figure 8.6: Cathode polarization curves of the optimized alkaline electrode with air at 25°C (iR corrected) compared to Nafion cathode (shifted by 0.7 V)

In the development of DMFCs, methanol cross-over has been an obstacle to achieving high performance [86-88]. Methanol which reaches the cathode can be oxidized at the same sites as the ORR resulting in lower current at a less desirable potential. The effect of methanol cross-over was studied in ADMFCs. A 2 M methanol solution was introduced into the membrane side compartment which was filled with 0.5 M NaOH, so the methanol would permeate through the membrane and affect the cathode performance. The potential was cycled at least 10 times at a scan rate of 50 mVs^{-1} until steady state

behavior was obtained. The change in cathode performance by methanol

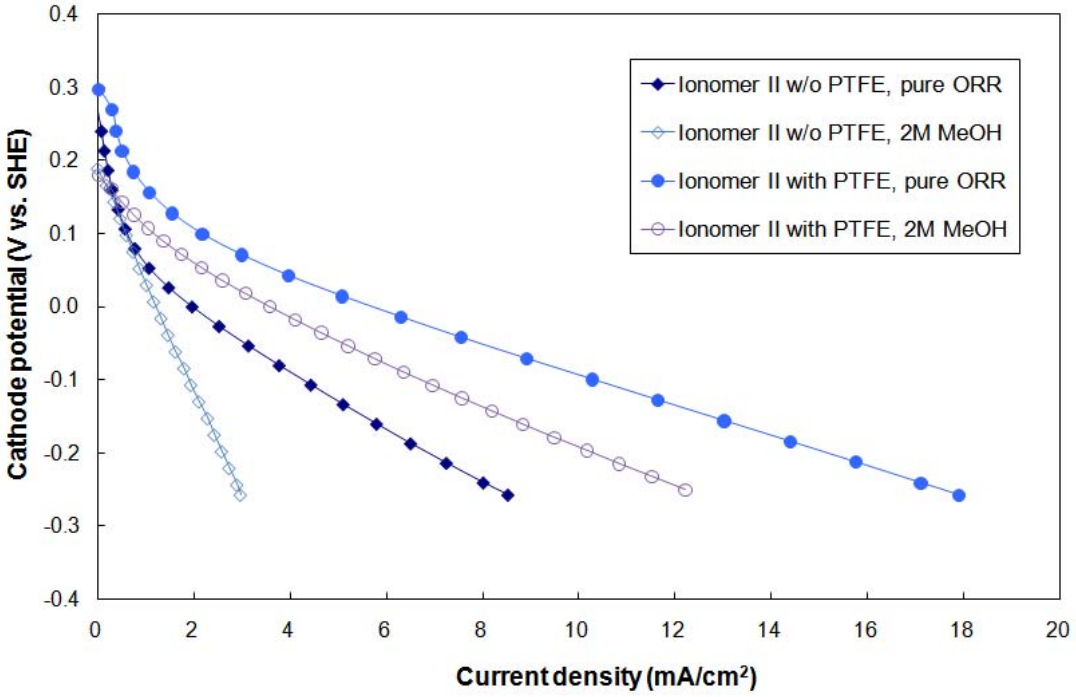

Figure 8.7: Cathode polarization curves with air (pure ORR), or with air and 2M methanol on the other side of the compartment (2M MeOH) at 25°C (iR corrected), showing the effect of PTFE on reducing methanol contact

permeation was observed and is shown in Figure 8.7. The performance and OCVs decreased for both electrodes, with and without PTFE (17 wt%) by the added methanol. However, the addition of PTFE decreased the degree of amount of performance degradation due to methanol cross-over from 64% to 35% at a potential of negative 0.2 vs. SHE. This is another benefit of higher hydrophobicity in the cathode catalyst layer. The hydrophobicity decreases the ratio of the liquid phase domains to the gas phase domains resulting in a decrease in the exposure of the catalyst to the methanol. The improved mechanical stability of the catalyst layer by PTFE addition could also increase the

catalyst utilization as well, since PTFE is a binder and could reduce the degree of ionomer swelling by methanol.

Figure 8.8 shows the anode polarization curves for Ionomer I and Ionomer II electrodes with or without PTFE. Unlike the cathode, Ionomer I and Ionomer II show similar performance. There was no improvement by the addition of a hydrophobic ionomer at the anode. A hydrophobic ionomer is beneficial in the cathode but not in a liquid-phase anode. The anode and cathode require different ionomers due to the liquid vs. gaseous reactants used.

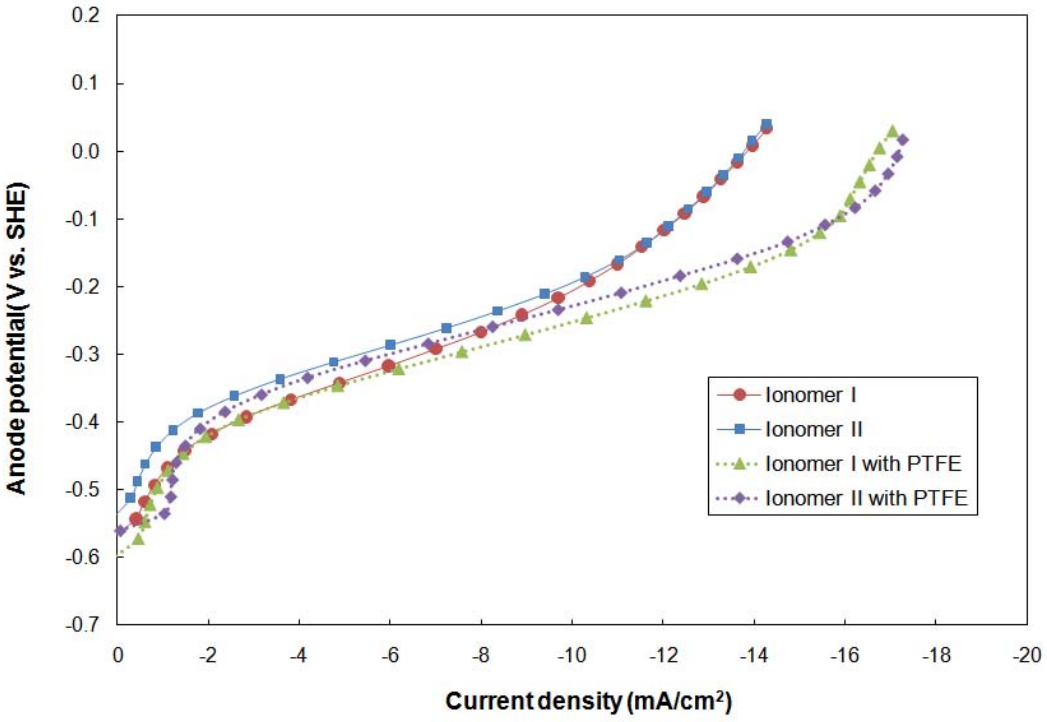

Figure 8.8: The effect of PTFE (17%) on MOR and the comparison of Ionomer I and Ionomer II with 1M methanol at 25°C (iR corrected)

On the other hand, Figure 8.8 also shows that the addition of PTFE increased the anode performance for Ionomer I and Ionomer II by the same degree. Although the

magnitude of the improvement by PTFE addition on anode performance was not as significant as at the cathode (Figure 8.5), the overpotential at the high current region is clearly improved. This result supports the conclusion that PTFE increases the mass transport properties by forming a porous structure. Also, carbon dioxide which is a product in anode reaction could be easily removed.

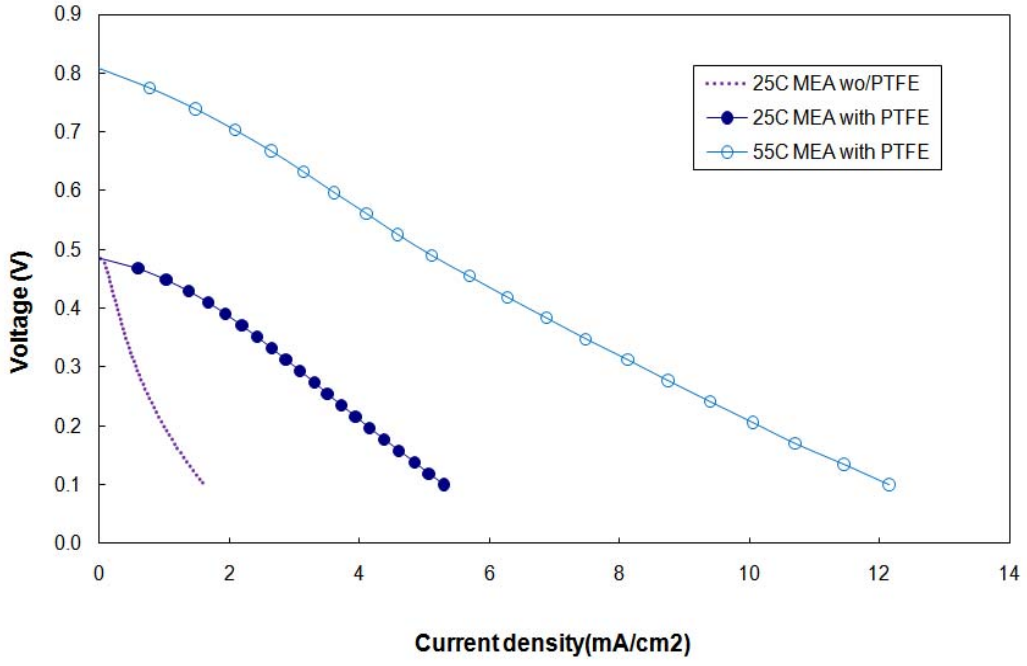

Figure 8.9: Comparison of fuel cell performance of the MEA with PTFE(17%) and without PTFE using a Tokuyama A201 membrane at 25°C and 55°, 1M methanol for anode and air for cathode

Finally, a passive feed system for the alkaline direct methanol fuel cell was demonstrated with the optimized electrodes and the A201 membrane. The cathode was open to the air and 1M methanol was used. Figure 8.9 shows the polarization curves comparing the optimized MEA with PTFE to the MEA without PTFE. The fuel cell

performance tripled by the addition of PTFE in the anode and cathode. At 55°C, the performance of the MEA with PTFE increased three-fold, and the OCV increased from 0.5 V to 0.8 V. The MEA without PTFE failed to operate at 55°C. There was a continuous decrease in current at constant voltage operation during conditioning due to the delamination of the electrode at higher temperature. Thus, PTFE helps the adhesion of the electrode to the membrane at higher temperature.

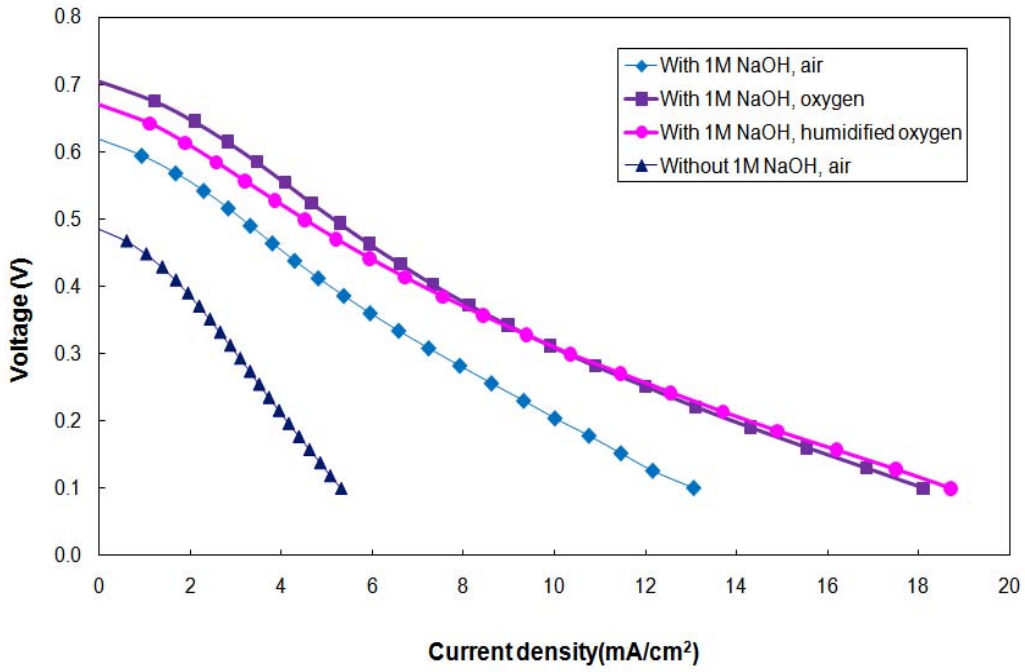

Figure 8.10: Fuel cell performance with or without 1M NaOH in 1M methanol for anode and air, oxygen or humidified oxygen for cathode at 25 °C using the optimized MEA

In Figure 8.10, the optimized MEA with PTFE was operated at different fuel conditions. 1M NaOH was added in the methanol fuel tank, and oxygen or 100% humidified oxygen was supplied at 7 ml min^{-1} to the cathode. The introduction of 1M

NaOH increased the fuel cell performance three-fold. The TPB was increased by adding NaOH. There have been many reports for alkaline DMFCs, and most of them showed high performance with the addition hydroxide to the methanol fuel. Nevertheless, the use of a hydroxide salt is not an acceptable solution for alkaline cells because of the precipitation of carbonates and bicarbonates.

Moreover, supplying oxygen fuel enhances the performance, but the magnitude of the improvement was not significant. The humidification decreased the performance in the low current range. These results confirm that a high water content in the catalyst layer limits gas transport resulting in loss of cell performance. Therefore, additional studies are needed on improving gas transport in the cathode electrode.

8.4 Summary

The effect of hydrophobicity on improving the electrode performances was investigated using two different ionomers and PTFE in the electrodes. Ionomer II had lower water uptake than Ionomer I due to its more hydrophobic backbone. The cathode overpotential was improved by using Ionomer II even though the ionic conductivity was lower. The effect of IEC, ionic conductivity and water uptake of ionomers has been evaluated on electrode performance. However, other properties of ionomers, such as the porosity and the degree of interaction with the catalysts, could have a minor effect on the performance. PTFE was introduced into the Ionomer II electrode to further increase its hydrophobicity. It was found that PTFE helped improve the overpotential. Compared to the traditional PEM cathode made with Nafion ionomer, the optimized alkaline cathode showed less activation overpotential but higher overpotential at high current range. The

hydrophobic ionomer was not effective at the anode, however, PTFE improved the anode overpotential. The results indicate that the addition of PTFE in the catalyst layer does decreases the water content and serves as a binder, improving the mechanical stability, introducing porosity, and improving mass transport. The fuel cell with optimized electrodes made of Ionomer II and 17wt% PTFE showed improved performance (three-fold) compared to the electrode without PTFE.

CHAPTER 9

CONCLUSIONS

The objective of this dissertation was to develop a DMFC system targeted at high energy density and low-loss to be used as the power source for small electronic devices. The most challenging issue in designing a highly efficient DMFC was to reduce the methanol cross-over, since the fuel loss by methanol permeation is dominant over IR loss at low power operation. The traditional polymer membrane was replaced with an inorganic glass membrane synthesized by sol-gel technology. It was also necessary to create an inorganic electrode assembly with the inorganic membrane. For utilizing the small volume allowed and achieving high power and voltage, anionic-cationic bi-cell stack design was proposed and demonstrated. The performance of ADMFCs was increased by improving the properties of AEM electrodes. This work advances the passive DMFC performance for systems where energy and volume density are of largest important.

High selectivity glass membranes have been successfully synthesized via sol-gel reaction using 3MPS, GPTMS and TEOS as the precursors. The conversion of the thiol in 3MPS to sulfonic acid, contribution of the different sol components to the membrane properties, and water ratio in the sol have been investigated. The highest selectivity, 6.23, was achieved with 3 hr oxidation time, 90:7:3 of 3MPS: GPTMS: TEOS and R ratio of 2. The ionic conductivity was 3.71 mS cm^{-1} and the permeability was 2.17 x 10^{-9} molcm $cm^{-2}day^{-1}Pa^{-1}$. The glass and polymer membrane behaviors have been studied and the conductivity and methanol permeability were characterized. The results indicate that the two properties were affected by the free volume in the glass. Less free volume results in lower methanol permeability and closer packing of the sulfonic acid groups providing a

pathway for protons. The lower activation energy for proton transport in the glass membrane, compared to Nafion, supports the surface transport mechanism in the glass. The fuel cell performance of the optimized glass membrane was tested with the Pt/C-SiO_2 electrodes for both anode and cathode. The OCV was 868 mV and the current density at 600 mV was 132 uA cm^{-2}. The total energy loss of the DMFC decreased from 99.9% to 75.2% by replacing the Nafion to the synthesized glass membrane.

Pt/C-SiO_2 glass composite electrodes were prepared by incorporating the Pt/C particles into PSG. It was found that raw samples showed high electrical sheet resistance due to the isolation of catalytic islands by the silicon dioxide dielectric. Therefore, a Leaman bath was used to electrolessly deposit Pt within the composite catalyst layer in order to both merge the catalyst islands and optimize the electrochemically active area of the electrode layer. It was found that the optimum Pt deposition time was 300 s, where the propagation threshold was reached. The resulting electrodes were highly active for the methanol oxidation reaction as ex-situ cyclic voltammograms in 0.5 M H_2SO_4, 0.5 M MeOH showed current densities two orders of magnitude higher than planar electrodes. Also, in a 1 cm^2 DMFC, the composite electrode showed a 50 mV higher open circuit voltage than a conventional Pt/C-Nafion® electrode, which was attributed to a decrease in methanol permeability from anode to cathode, and a moderate improvement in the current was achieved.

For efficient methanol oxidation, Pt_xRu_{1-x} bimetallic electrocatalysts have been prepared by modifying the Leaman bath in terms of precursor concentration and bath temperature. Ruthenium formed an ammoniacal complex when the traditional reducing agent, hydrazine, was used, leading to poor bath efficiency. As an alternative reducing

agent, formic acid yielded 1:1 ratio of Pt and Ru even at lower temperature. The metal deposition process was consistent with the behavior of a galvanic, electrocatalytic bath. An empirical electrochemical model developed in the previous study has been used to compare the experimental results. The model was found to be accurate over a wide range of temperatures and bath compositions.

The blocking effect of the glass electrodes on methanol cross-over was explored using PtRu/SiO_2 inorganic electrodes synthesized using 3TPS and GPTMS. The effect of the gelation time, curing temperature, the mole ratio of the sol components, and the ratio of catalyst to glass in the electrode were investigated in terms of catalytic activity, the adhesion to the glass membrane and inhibition of methanol permeation. PtRu layer was electrolessly deposited on top of the glass electrode as a current collector. It was found that the additional deposit metal layer improved all of the three important parameters; the methanol permeability, the catalytic activity of the electrodes for methanol oxidation, and the sheet conductivity. The selectivity was increased from 6.23 to 7.21 by the blocking effect of the glass composite electrode with the lowest permeability coefficient. Correspondingly, the total loss decreased from 57.1 to 19.12%. The inorganic MEA showed stable performance for more than 10 days.

Three different types of stack design for PEM fuel cells have been discussed. The bipolar stack is the most common design due to the high fuel cell performance, even though the metallic bipolar plate is expensive. The monopolar stack has the advantage of light weight and low cost. The bi-cell stack could reduce the overall system volume due to the use of a common fuel tank. However, the fuel cell performance of the monopolar and bi-cell stack is lower than bipolar configuration due to the higher internal resistance

of the current collector (i.e. there is no extra current collector in the monopolar and bi-cell stack). Also, in the case of the DMFC application, there exists the possible ionic short circuit between adjacent anodes through the common fuel tank. In order to address this concern, a bi-cell design with an AEM and PEM fuel cell in series using a common liquid fuel tank was demonstrated. The electrode potentials for both acid-PEM and alkaline-AEM were evaluated and shown to match the combined cell. The actual AEM cathode potential was essentially the same as the PEM anode potential making the bi-cell configuration viable. The bi-cell system was demonstrated with the optimized AEM and PEM fuel cell in series operated from a single fuel tank. In addition to the higher voltage (theoretically, 2.4 V) and reduced volume using a common fuel tank, self-humidification and easy water management are interesting advantages of the AEM-PEM bi-cell stack.

The effect of hydrophobicity on improving the electrode performances was investigated using two different ionomers and PTFE additives. Ionomer II had lower water uptake than Ionomer I due to the more hydrophobic backbone of Ionomer II. The cathode overpotential was improved by using Ionomer II even though the ionic conductivity was lower. PTFE was introduced to the Ionomer II electrode to further increase the hydrophobicity. It was found that PTFE helped to improve the overall overpotential. Compared to the traditional PEM cathode made of Nafion ionomer, the optimized alkaline cathode showed less activation overpotential but higher overpotential at high current range. The hydrophobic ionomer was not effective at the anode side, but PTFE improved the anode overpotential as well. Results indicate that the addition of PTFE in the catalyst layer does not only decrease the water content but also serves as binder, improving mechanical stability, and introduce porosity, improved mass transport.

The fuel cell with optimized electrodes made of Ionomer II and 17wt% PTFE improved performance by three times compared to the electrode without PTFE. To further increase the performance of ADMFCs, more hydrophobic ionomer with high ionic conductivity, and a porous catalyst structure are recommended for cathode electrodes.

REFERENCES

1. S. K. Kamarudin, W. R. W. Daud, S. L. Ho and U. A. Hasran, *J Power Sources*, **163**, 743 (2007).
2. H. W. Cooper, *Chemical Engineering Progress*, **103**, 34 (2007).
3. B. Bae, H. Y. Ha and D. Kim, *J Membrane Sci*, **276**, 51 (2006).
4. C. Y. Yen, C. H. Lee, Y. F. Lin, H. L. Lin, Y. H. Hsiao, S. H. Liao, C. Y. Chuang and C. C. M. Ma, *Journal of Power Sources*, **173**, 36 (2007).
5. R. C. Jiang, H. R. Kunz and J. M. Fenton, *Journal of Membrane Science*, **272**, 116 (2006).
6. S. Prakash, W. E. Mustain, S. Park and P. A. Kohl, *Journal of Power Sources*, **175**, 91 (2008).
7. D. A. Ward and E. I. Ko, *Abstracts of Papers of the American Chemical Society*, **209**, 182 (1995).
8. S. Sakka and H. Kozuka, *Journal of Sol-Gel Science and Technology*, **13**, 701 (1998).
9. T. Uma, K. Hattori and M. Nogami, *Ionics*, **11**, 202 (2005).
10. C. Wang, M. Nogami and Y. Abe, *Journal of Sol-Gel Science and Technology*, **14**, 273 (1999).
11. S. P. Tung and B. J. Hwang, *J Mater Chem*, **15**, 3532 (2005).
12. C. Wang and M. Nogami, *Materials Letters*, **42**, 225 (2000).
13. M. Nogami, H. Matsushita, Y. Goto and T. Kasuga, *Advanced Materials*, **12**, 1370 (2000).
14. M. Nogami, R. Nagao, G. Wong, T. Kasuga and T. Hayakawa, *Journal of Physical Chemistry B*, **103**, 9468 (1999).
15. T. Tezuka, K. Tadanaga, A. Matsuda, A. Hayashi and M. Tatsumisago, *Electrochemistry Communications*, **7**, 245 (2005).
16. S. W. Li and M. L. Liu, *Electrochim Acta*, **48**, 4271 (2003).
17. Y. Park and M. Nagai, *Solid State Ionics*, **145**, 149 (2001).
18. Y. Park and M. Nagai, *Journal of the Electrochemical Society*, **148**, A616 (2001).

19. Y. I. Park, J. Moon and H. K. Kim, *Electrochemical and Solid State Letters*, **8**, A191 (2005).
20. X. H. Ye and C. Y. Wang, *Journal of the Electrochemical Society*, **154**, B676 (2007).
21. N. W. Deluca and Y. A. Elabd, *Journal of Polymer Science Part B-Polymer Physics*, **44**, 2201 (2006).
22. S. Slade, S. A. Campbell, T. R. Ralph and F. C. Walsh, *Journal of the Electrochemical Society*, **149**, A1556 (2002).
23. S. Prakash, *Ph.D. thesis, Georgia Institute of Technology* (2009).
24. D. A. Ward and E. I. Ko, *Journal of Catalysis*, **157**, 321 (1995).
25. C. J. Brinker, A. J. Hurd, P. R. Schunk, G. C. Frye and C. S. Ashley, *Journal of Non-Crystalline Solids*, **147**, 424 (1992).
26. H. Kim, S. Prakash, W. E. Mustain and P. A. Kohl, *J Power Sources*, **193**, 562 (2009).
27. P. Waszczuk, J. Solla-Gullon, H. S. Kim, Y. Y. Tong, V. Montiel, A. Aldaz and A. Wieckowski, *Journal of Catalysis*, **203**, 1 (2001).
28. H. A. Gasteiger, N. Markovic, P. N. Ross and E. J. Cairns, *Journal of Physical Chemistry*, **97**, 12020 (1993).
29. W. E. Mustain, H. Kim, V. Narayanan, T. Osborn and P. A. Kohl, *J Fuel Cell Sci Tech*, **7** (2010).
30. F.H.Leaman, Platinum Chemical Plating, in, U.S. (1972).
31. D. Chu and R. Z. Jiang, *J Power Sources*, **80**, 226 (1999).
32. A. Heinzel, C. Hebling, M. Muller, M. Zedda and C. Muller, *J Power Sources*, **105**, 250 (2002).
33. R. Z. Jiang and D. R. Chu, *J Power Sources*, **93**, 25 (2001).
34. Y. J. Kim, B. Bae, M. A. Scibioh, E. Cho and H. Y. Ha, *J Power Sources*, **157**, 253 (2006).
35. M. Oszcipok, M. Zedda, J. Hesselmann, M. Huppmann, M. Wodrich, M. Junghardt and C. Hebling, *J Power Sources*, **157**, 666 (2006).
36. D. J. Kim, E. A. Cho, S. A. Hong, I. H. Oh and H. Y. Ha, *J Power Sources*, **130**, 172 (2004).

37. D. Kim, J. Lee, T. H. Lim, I. H. Oh and H. Y. Ha, *J Power Sources*, **155**, 203 (2006).
38. E. Antolini and E. R. Gonzalez, *J Power Sources*, **195**, 3431 (2010).
39. C. Coutanceau, L. Demarconnay, C. Lamy and J. M. Leger, *J Power Sources*, **156**, 14 (2006).
40. S. D. Poynton, J. P. Kizewski, R. C. T. Slade and J. R. Varcoe, *Solid State Ionics*, **181**, 219 (2010).
41. J. Kim, T. Momma and T. Osaka, *J Power Sources*, **189**, 999 (2009).
42. M. Sudoh, Niimi,S., Takaoka,N., Watanabe,M., *ECS Transactions*, **25**, 61 (2010).
43. E. H. Yu and K. Scott, *J Power Sources*, **137**, 248 (2004).
44. H. Bunazawa and Y. Yamazaki, *J Power Sources*, **182**, 48 (2008).
45. H. Kim, M. Unlu, J. F. Zhou, I. Anestis-Richard and P. A. Kohl, *J Power Sources*, **195**, 7289 (2010).
46. K. Scott, E. Yu, G. Vlachogiannopoulos, M. Shivare and N. Duteanu, *J Power Sources*, **175**, 452 (2008).
47. Y. S. Li, T. S. Zhao and Z. X. Liang, *J Power Sources*, **190**, 223 (2009).
48. W. E. Mustain, H. Kim, S. Prakash, J. Stark, T. Osborn and P. A. Kohl, *Electrochem Solid St*, **10**, B210 (2007).
49. S. Z. Ren, G. Q. Sun, C. N. Li, Z. X. Liang, Z. M. Wu, W. Jin, X. Qin and X. F. Yang, *Journal of Membrane Science*, **282**, 450 (2006).
50. S. Shylesh, S. Sharma, S. P. Mirajkar and A. P. Singh, *Journal of Molecular Catalysis a-Chemical*, **212**, 219 (2004).
51. T. Kobayashi, M. Rikukawa, K. Sanui and N. Ogata, *Solid State Ionics*, **106**, 219 (1998).
52. I. Diaz, F. Mohino, J. Perez-Pariente and E. Sastre, *Thermochimica Acta*, **413**, 201 (2004).
53. R. L. Guo, C. L. Hu, F. S. Pan, H. Wu and Z. Y. Jiang, *Journal of Membrane Science*, **281**, 454 (2006).
54. H. Kataoka, Y. Saito, M. Tabuchi, Y. Wada and T. Sakai, *Macromolecules*, **35**, 6239 (2002).

55. P. Malik, M. Castro and C. Carrot, *Polymer Degradation and Stability*, **91**, 634 (2006).
56. B. Tazi and O. Savadogo, *Electrochimica Acta*, **45**, 4329 (2000).
57. V. Neburchilov, J. Martin, H. Wang and J. Zhang, *Journal of Power Sources*, **169**, 221 (2007).
58. F.H.Leaman, *Plating*, **59**, 5 (1972).
59. R. Liu, K. Triantafillou, L. Liu, C. Pu, C. Smith and E. S. Smotkin, *J Electrochem Soc*, **144**, 2942 (1997).
60. W. E. Mustain, H. Kim, T. Osborn and P. A. Kohl, *Isr J Chem*, **48**, 251 (2008).
61. W. M. Latimer, *Soil Science*, **48** (1939).
62. F. A. Cotton, and Wilkinson,Glk,, *Advanced inorganic chemistry:A comprehensive text*, Wiley-Interscience, New York (1972).
63. J. Chatt, *Platinum Metals Review*, **13**, 6 (1969).
64. C. Rice, S. Ha, R. I. Masel and A. Wieckowski, *J Power Sources*, **115**, 229 (2003).
65. H. Kim and P. A. Kohl, *J Power Sources*, **195**, 2224 (2010).
66. G. Alberti, M. Casciola and R. Palombari, *Solid State Ionics*, **52**, 291 (1992).
67. J. S. Lee, K. I. Han, S. O. Park, H. N. Kim and H. Kim, *Electrochim Acta*, **50**, 807 (2004).
68. E. Passalacqua, F. Lufrano, G. Squadrito, A. Patti and L. Giorgi, *Electrochim Acta*, **46**, 799 (2001).
69. T. Iwasita, *Electrochim Acta*, **47**, 3663 (2002).
70. S. Wasmus and A. Kuver, *J Electroanal Chem*, **461**, 14 (1999).
71. J. F. Zhou, M. Unlu, J. A. Vega and P. A. Kohl, *J Power Sources*, **190**, 285 (2009).
72. J. R. Varcoe, R. C. T. Slade, G. L. Wright and Y. L. Chen, *J Phys Chem B*, **110**, 21041 (2006).
73. J. R. Varcoe and R. C. T. Slade, *Fuel Cells*, **5**, 187 (2005).
74. J. R. Varcoe, R. C. T. Slade, E. L. H. Yee, S. D. Poynton, D. J. Driscoll and D. C. Apperley, *Chem Mater*, **19**, 2686 (2007).
75. M. Ü. J.F.Zhou, I.Anestis-Richard, P.A.Kohl, *J Membrane Sci*, **350**, 7 (2010).
76. E. Antolini, L. Giorgi, A. Pozio and E. Passalacqua, *J Power Sources*, **77**, 136 (1999).

77. E. R. G. E.Antolini, *J Power Sources*, **195**, 20 (2010).
78. J. H. Kim, H. Y. Ha, I. H. Oh, S. A. Hong, H. N. Kim and H. I. Lee, *Electrochim Acta*, **50**, 801 (2004).
79. B. Krishnamurthy, S. Deepalochani and K. S. Dhathathreyan, *Fuel Cells*, **8**, 404 (2008).
80. J. G. Liu, T. S. Zhao, R. Chen and C. W. Wong, *Electrochem Commun*, **7**, 288 (2005).
81. J. Zhou, M. Ünlü, J. A. Vega and P. A. Kohl, *J Power Sources*, **190**, 285 (2009).
82. T. N. Danks, R. C. T. Slade and J. R. Varcoe, *J Mater Chem*, **13**, 712 (2003).
83. M. Ünlü, J. F. Zhou, I. Anestis-Richard and P. A. Kohl, *ChemSusChem*, **Submitted** (2010).
84. M. Ünlü, J. F. Zhou, I. Anestis-Richard and P. A. Kohl, *J Electrochem Soc*, **157**, 6 (2010).
85. D. S. Chan and C. C. Wan, *J Power Sources*, **50**, 163 (1994).
86. J. Ling and O. Savadogo, *J Electrochem Soc*, **151**, A1604 (2004).
87. Z. G. Qi and A. Kaufman, *J Power Sources*, **110**, 177 (2002).
88. A. Kuver and W. Vielstich, *J Power Sources*, **74**, 211 (1998).